LBL-8407 c. 2

Lawrence Berkeley Laboratory
UNIVERSITY OF CALIFORNIA

A NON-EQUILIBRIUM STATISTICAL MECHANICAL APPROACH FOR DESCRIBING HEAVY ION REACTIONS

Joseph Sherman Sventek
(Ph.D. thesis)

November 1978

Prepared for the U.S. Department of Energy under Contract W-7405-ENG-48

A NON-EQUILIBRIUM STATISTICAL MECHANICAL APPROACH FOR DESCRIBING HEAVY ION REACTIONS

by

Joseph Sherman Sventek

Lawrence Berkeley Laboratory
University of California
Berkeley, California 94720

A NON-EQUILIBRIUM STATISTICAL MECHANICAL APPROACH FOR DESCRIBING HEAVY ION REACTIONS

BY

JOSEPH SHERMAN SVENTEK

ABSTRACT

With the availability of heavy-ion projectiles ($A > 4$) at low to intermediate energies ($4 < E/A < 10$), products showing various stages of relaxation for certain macroscopic variables (center-of-mass energy, orbital angular momentum, etc.) were produced in various reactions. The distributions for these macroscopic variables showed a correlation between the stage of relaxation reached and the net amount of mass transfer which had occurred in the reaction. There was also evidence that there was an asymmetry in the number of net transfers necessary for complete relaxation between stripping and pickup reactions.

A model for describing the time-evolution of these reactions has been formulated, the keystone of which is a master-equation approach for describing the time-dependence of the mass-asymmetry. This, coupled with deterministic equations of motion for the other macroscopic coordinates in the reaction lead to calculated distributions which provide

an excellent qualitative description of these reactions, and, in some cases, quantitatively reproduce the experimental data quite well.

Acknowledgements

I am greatly indebted to Luciano G. Moretto for his guidance and assistance throughout my research. He not only suggested the possibility of using non-equilibrium methods to describe these reactions, but also provided the main impetus for this work.

Further, I wish to thank R. Babinet, A. Behkami, B. Cauvin, J. Galin, P. Glassel, J. Hunter, R. Jared, G. Mathews, J. Moulton, P. Russo, R. Schmitt and G. Wozniak for the many stimulating discussions during my stay with their research group.

I have benefited from numerous discussions with H. C. Britt, J. Huizenga, W. Myers, J. R. Nix, J. Randrup, W. Swiatecki, C. F. Tsang and R. Vandenbosch during the course of this research.

The guidance and assistance of D. Hall, H. Holmes and C. Quong during the completion of this work is greatfully acknowledged.

Last, but certainly not least, I wish to thank my wife, Virginia, and my son, Gabriel, for tolerating the inevitably long hours necessary to do the research and to write it up. In order to express my gratitude for their love and patience, this work is dedicated to them.

This work was performed under the auspices of the U. S. Department of Energy.

TABLE OF CONTENTS

Chapter I

Foundations

This thesis is concerned with some of the very exciting developments which have occurred in the field of Nuclear Physics since 1973, and is an attempt to describe some of the complex workings of heavy-ion reactions in terms of quite elementary models. It is hoped that some of the insights provided by this work will stimulate further study in this growing field, and that an eventual unification of many facets of nuclear science research will result.

A. Comparison of Compound Nucleus and Direct Reactions

Prior to the advent of heavy-ion accelerators, most nuclear reactions could be classified as one of two general types [Har69]:

1. Direct reactions. This general label applies to those reactions which are very elastic in nature. Typically, they involve very peripheral interactions between the two nuclei, and the resulting products display very small deviations of the values of all macroscopic variables (orbital angular momentum, center of mass kinetic energy, etc.) from the corresponding values in the entrance channel. The peripheral nature of these reactions (as determined

from the angular distributions) seemed to indicate that only the partial waves in a narrow band around the classical grazing angular momentum contribute substantially to the Direct Reaction products. These reactions occupy one end of an "equilibration" spectrum, that of highly non-equilibrated reactions, since none of the macroscopic variables have shifted markedly from the entrance channel values towards the true equilibrated ones.

2. Compound nucleus reactions. This general label applies to those reactions which are very inelastic in nature. In the case of the collision of two heavy ions, only the most central interactions lead to a compound nucleus, and the resulting products are truly equilibrated - i.e. the total energy of the system has been statistically shared among all degrees of freedom, and the final distribution for a given collective variable is determined from level densities and average matrix elements. The central nature of these reactions (as inferred from the gamma-ray yields of the products) seemed to indicate that only the most central collisions (smallest partial waves) contributed significantly to the compound nucleus cross section. Obviously, these reactions occupy the other end of the equilibration spectrum, that of totally equilibrated systems.

To be sure, there were some indications of processes intermediate to these two extremes (pre-equilibrium decay, giant multipole resonances, etc. [Mah73,Blo63]). In the case of pre-equilibrium decay, the physical situation was not conducive to a true investigation of the approach to equilibrium for various collective modes, since only single particle modes (particle-hole excitations) were induced.

One significant piece of information concerning the above reactions is glaringly absent: no mention of the relevant time scale has been made. Direct reactions must, for obvious reasons, occur on a time scale on the order of the time necessary for the projectile to fly past the target nucleus. The lifetime of a compound nucleus, on the other hand, must be long compared to the lifetime of all transient states populated during the approach of all variables to their equilibrated values. Nature did not seem to provide the nuclear physicist with the opportunity to watch the collective modes equilibrate.

B. Intermediate Aspects of Deep Inelastic Reactions

The acceleration of heavy-ions ($A > 4$) provided the tool necessary to attack the problem which was outstanding at the close of the previous section. One could now study various stages of equilibration for the following reasons:

1. The entrance channel mass-asymmetry may be far from the compound nucleus limit; if equilibration is

mediated by single particle exchange, then many exchanges must occur before a compound nucleus results.

2. Large numbers of partial waves may be involved, implying that a large portion of the cross section should fall in a region intermediate to the two extremes described above.

A crude estimate of the time dependence of any collective variable may be had by measuring its angular dependence, since the angular position can be roughly correlated with the interaction time. Furthermore, the interplay of various collective modes can be followed quite easily. Examples of these effects may be found in Chapter II.

C. Classical vs. Quantal Treatment of the Dynamics

In order to describe Direct Reactions, one must resort to a quantum mechanical description. This is due, in part, to the large size of the wave packet for the projectile as compared to the typical interaction distance. Also, the interaction time mentioned above is comparable to the period of nucleonic motion within the target nucleus, implying a small number of nucleonic interactions, so that individual quantum mechanical matrix elements and selection rules will play a large part in determining the dynamics of the interaction. The interaction time for Compound Nucleus reactions, on the other hand, is orders of magnitude larger than the period of nucleonic motion, implying that average matrix elements and level densities can be used to describe the final states of the reaction variables. Therefore, aside from constraints imposed by conservation laws, the macroscopic variables describing the products of the decayed compound nucleus depend only upon the aforementioned average quantities.

A question of interest is how to treat the dynamics for deep-inelastic collisions. As will be shown later, these reactions are fairly peripheral in nature, with the reaction cross section coming largely from a window of partial waves near the grazing value. If it can be shown that the size of the system's wave packet is small compared to the interaction radius, then a classical (or, at least, a semi-classical) treatment should be valid. Any other situation would dictate a quantum mechanical approach.

The size of the wave packet should be of the order of the de Broglie wave length $\lambdabar$, given by the prescription

$$\lambdabar = \hbar / p \tag{1.1}$$

As long as the velocity of the reduced mass is small compared to the speed of light

$$\beta \equiv \frac{v}{c} << 1 \tag{1.2}$$

p can then be evaluated classically to give

$$p = [2\mu(E - V(r))]^{\frac{1}{2}} \qquad (1.3)$$

where E is the energy of the system and V is the potential energy at the radius r. A classical approximation is valid, therefore, if

$$\frac{\lambdabar}{r} \ll 1 \qquad (1.4)$$

Estimates of this quantity range from 0.005 to 0.05, thereby indicating that a classical formulation for the nuclear dynamics is justified.

D. Definition of Terms

At this juncture, it is appropriate to define many of the terms used throughout the thesis. This glossary, together with the local definitions in the text, should provide a sufficient base for a non-specialist in the field to follow the discussion of the various topics in the thesis.

charge(mass) asymmetry

A measure of the distribution of the total mass of the system. As will be described, these reactions are binary in nature, implying that the charge(mass) is partitioned into two well defined sections. The usual measure of the charge(mass) asymmetry is the charge(Z) or mass(M) of the smaller fragment. If the mass is not partitioned into well defined sections, the mass asymmetry becomes undefined. In a geometrical sense, one can picture the shape of the reaction intermediate at the time of breakup as consisting of two connected non-intersecting shapes. A particular measure of the asymmetry could be the volume of the smaller fragment divided by the total volume of the two shapes, since nuclear matter is basically incompressible.

collective mode

A degree of freedom which is manifested by the individual elements in a system working in concert. Some typical examples are:

1. the distance between the centers of two colliding nuclei
2. the shape vibrations of a drop of liquid nitrogen

deep-inelastic collisions

Those nuclear reactions which present values of certain observables which are intermediate to the two extremes described in section I.A. A more complete description is given in Chapter II. Synonyms for deep-inelastic include quasi-fission, strongly-damped and relaxed.

equilibration

The process of approaching equilibrium. A collective mode has equilibrated if the distributions for its observables are determined purely from the distribution of level densities of the reaction intermediate at the scission point.

giant resonance

A particular example of a collective mode, wherein the majority of the strength for a particular multipole vibration is concentrated in a limited energy region.

grazing angle

The hypothetical scattering angle for a nuclear collision in which the distance of closest approach is the interaction radius (see below).

interaction radius

The distance between nuclear centers at which the nuclear density distributions begin to interact via the strong nuclear force.

intermediate complex

A term loosely used to describe the interacting nuclei while they are in the interaction region. The binary nature of the reaction (section II.A) indicates that the physical nature of the complex is that of two connected shapes.

scission point

That point in the evolution of the complex in coordinate space at which the nuclei cease to interact strongly. The distributions of most observables will reflect the corresponding values at this point in time.

E. Purpose and Contents of the Thesis

The purpose of the thesis is twofold: obviously, it summarizes the author's efforts in this area over the last six years. More importantly, it is hoped that this work will stimulate discussion in an area in which there is still little agreement among researchers as to the interpretation of experimental results and the underlying physical mechanisms involved. The situation is more global than it might appear to be; the correct interpretation of deep-inelastic collisions will implicitly describe both of the extreme situations seen in the early experiments, thereby unifying much of nuclear physics. While no pretenses to that effect are made here, it is hoped that the present work can make a small contribution toward that goal.

The remainder of the thesis consists of five parts:

1. Chapter II is concerned with the experimental evidence of partial equilibration in several macroscopic observables of heavy-ion reactions. This chapter is global in nature, and general trends, rather than the intricacies of a single system, are described. The main focus of this chapter is to derive an experimental hierarchy of relaxation times for the various observables which will give some insight into the physics behind the diffusion model, which is presented in chapter IV.

2. In chapter III, an attempt is made to show what assumptions are necessary to obtain a stochastic equation of motion for a quantal system, given the Hamiltonian of the system. This chapter makes no pretenses of originality (most of the derivations may be obtained from any textbook on non-equilibrium statistical mechanics), and is only included for completeness. For a more thorough exposition of the subject, the pioneering work of Norenberg [Nor75] should be consulted. The main points made in this chapter are those requirements necessary for a master equation approach to be valid, and the relationship between the master equation and its associated Fokker Planck equation.
3. Chapter IV is the meat of the thesis, as it describes the various parts of the diffusion model. In the interest of continuity, many of the lengthly derivations have been relegated to appendices. It should be noted that many of the new features of the model are described in those appendices. It is therefore strongly advised that the appendices be read upon completion of Chapter IV. It is hoped that the material in this chapter will make clear the general physical principles at work in these reactions, and how they may be described in a simple manner.
4. Chapter V is a comparison of the experimental

distributions with the calculated results. It should be noted that the author has striven for a qualitative understanding of these reactions, and has avoided parameter adjustment to achieve quantitative fits of the experimental data in this work. There are no adjustable parameters in the model. Given its relative crudeness, therefore, quantitative fits are not expected. It is gratifying, though, that many of the differential distributions which display accurate qualitative trends reduce to integrated distributions which fit their experimental counterparts quite well.

5. Chapter VI is an attempt to objectively summarize the preceding chapters, and to draw conclusions concerning the relevance of the current work.

Chapter II

Experimental Evidence for Non-equilibrium Behavior in Heavy Ion Reactions

A. General Features of Experimental Distributions

To date, most of the experimental information concerning deep-inelastic collisions has been obtained from the measurement of the following properties of the final reaction products: kinetic energy, charge, mass, and angular distributions [Gal70,Art73,Mor73,Wol74,Kra74,Van76,Sch77]. Simultaneous measurement of two or more of these properties allows correlations between the observables to be discerned. Presently, multi-parameter coincidence measurements of secondary-emission products (those products emitted during the de-excitation of the primary products in the exit channel) are being performed to learn about various properties of the intermediate complex at the scission point [Gla77,Per77,Har77,Gal74]. From these studies, the following general features of deep inelastic collisions have emerged:

1. The exit channel consists of two massive primary fragments (the process is primarily binary in nature).
2. The final kinetic energies of the products display varying degrees of damping of the entrance channel kinetic energy, ranging from essentially elastic

energies down to the Coulomb interaction energy between highly deformed fragments.

3. An exchange of nucleons occurs during the time of interaction between the two nuclei, leading to distributions in the masses of the fragments. For collisions which can be characterized by short interaction times, the mass distributions (for the light primary fragment) are peaked at the projectile mass and are quite narrow, while for collisions resulting in longer interaction times, the mass distributions are broader and shifts of the centroid can be discerned, the direction of the drift correlating with potential energy considerations.
4. The angular distribution for the projectile-like products, integrated over energy and charge, is strongly peaked in the neighborhood of the grazing angle. When this distribution is decomposed into the distributions for each Z, the peaking gradually transforms into a general forward peaking as one moves in Z away from the projectile.
5. The average neutron-to-proton (N/Z) ratio reflects the value which minimizes the potential energy of the intermediate complex, independent of the entrance channel values, after accounting for secondary particle emission from the primary fragments.
6. Angular momentum is transferred from relative orbital motion to the intrinsic spins of the two primary

fragments.

7. The de-excitation of the primary fragments in the exit channel occurs through the emission of light particles (n, p, α) and γ -rays; the target-like primary fragment may also fission, if the barrier is small enough to allow fission to compete with particle emission.

Since these reactions display properties of a fast, peripheral process (peak near the grazing angle), a natural time scale is established [Nor74,Bon75]. Comparison of properties measured at the grazing angle with those measured at more forward angles (which require the nuclei to interact for longer times in order to rotate to the more forward angle) yields an approximate relaxation time for the observable in question. These correlations with scattering angle will be exploited many times in the succeeding sections.

The fact that deep inelastic collisions are binary processes was originally suspected from the values of the kinetic energies observed for the fragments [Mor73,Col74]. Correlated measurements of the two primary fragments indicate that they are indeed emitted at 180 in the center-of-mass system, and perturbations of the measured angle about this value are consistent with secondary emission of light particles [Cau78a]. For further discussion of this subject, see [Sch77].

In succeeding sections, each of the other properties is discussed in turn. For each property, the main experimental features are outlined. The situation in which the property in question is totally equilibrated is described. Where appropriate, relationships between this property and other aspects of nuclear reactions are discussed. If available, experimental information concerning mechanisms for the equilibration of the observable is presented. Finally, the relaxation time of the observable is estimated from its correlation with scattering angle. From the hierarchy of relaxation times which results, one can view the interplay between various collective modes, and the choice of the "slow" mode to be described by non-equilibrium statistical methods will become obvious.

B. Kinetic Energy Distributions

One of the most distinctive features of deep inelastic reactions is the broad kinetic energy distributions observed for all products [Gal70,Art73,Mor73,Wol74,Kra74,Van76,Sch77]. As can be seen in figures 1-3, the kinetic energy distributions display two main features:

1. For all products measured at all angles, there is a large cross section for events whose total kinetic energy (the sum of the kinetic energies of the

primary fragments) in the center-of-mass system is quite close to the Coulomb energy of two touching fragments (see figures 4 and 5). For reactions involving fairly light projectile-target combinations, the centroid of this low energy component follows the Coulomb energy of two spheres at the interaction radius, while for heavier projectile-target systems, the general trend of these centroids seems to indicate that the relevant configuration at scission may be more stretched and involve deformation of the primary fragments. It should also be noted that the position of the centroid of this low energy component for a given reaction is independent of the angle at which the product is observed.

2. For products with atomic numbers (masses) close to that of the projectile at angles near the grazing angle, the distributions display a range of kinetic energies, varying from essentially no loss of the entrance channel kinetic energy down to the low energy component described above. For reactions where the bombarding energy is quite large compared to interaction barrier (E/B > 2), a well-defined separation of the low energy component and a high energy component is observed, and one may speak of a "relaxed" and a "quasi-elastic" component. For low-energy bombardments (E/B < 1.5), the spectra are

very broad, with no discernable separation of components.

From our definition of equilibration (section I.D), the exit channel kinetic energy is relaxed if it is due entirely to the potential energy of the scission shape, with no dependence upon dynamics, other than the energy tied up in the rigid rotation of the complex. The correlation of the centroid of the "relaxed" component with the Coulomb plus rotational energy of a connected shape indicates that these events are truly equilibrated, hence the name "relaxed".

Much information can be derived from the correlation between the kinetic energy and other experimental observables. The first studied was the correlation between the total kinetic energy (hereafter referred to as TKE) of the fragments and the center-of-mass angle of the light fragment [Wil73]. Examples of this type of correlation (the pictorial representation of which is called a Wilczynski plot or diagram) are displayed in figures 6 and 7. Wilczynski's original interpretation of the type of diagram seen in figure 6 is that the upper ridge of cross section, starting at the elastic energy and the grazing angle and moving to lower energies for more forward angles, is due to positive angle scattering, as depicted schematically by trajectory 1 in figure 8. The lower ridge, seen at essentially constant energy and extending out to large scattering angles, is due to negative angle scattering, shown schematically as trajectory 2 in figure 8. If, during the course of the reaction, some of the orbital angular momentum is transformed into spin angular momentum of the fragments, as is known (see section II.D), and this spin is oriented perpendicular to the reaction plane, then the spins of the nuclei for the two trajectories of figure 8 will be aligned in opposite directions. This fact has been measured experimentally [Tra77] by detecting the polarization of the gamma-rays emitted by the primary fragments in the relaxed and the quasi-elastic parts of the spectrum. The fact that some trajectories lead to negative angle scattering is sometimes referred to as "partial orbiting". Perusal of figure 7 for Z = 24, 28, 42, 44 shows that for products which involve sufficiently large net mass transfer, only the low energy ridge appears, implying that the exit channel kinetic energies for such asymmetries are completely relaxed. The behavior of the high energy ridge in figure 7 for Z = 34, 38 seems contrary to that seen in figure 6. Very little angular motion is observed as the ridge drops from elastic to relaxed energies, which is sometimes referred to as "strong focussing" [Sch77]. This seemingly anomalous behavior is due to the fact that the average rotational frequency $\overline{\omega}$ is small enough such that the product

$$\Delta\theta = \overline{\omega}\,\tau_E \qquad (2.1)$$

where τ_E is the relaxation time for the kinetic energy, is a small quantity. Thus by increasing $\bar{\omega}$ for a given reaction system, one should see a transition from a "strongly focussed" situation to a "partial orbiting" one. Equivalently, the type of behavior exhibited by the high energy ridge in the Wilczynski diagram should strongly correlate with the ratio E/B, since $\bar{\omega}$ is an increasing function of this ratio. Experimental verification of this point is displayed in figures 9 and 10. Figure 9 is a Wilczynski plot for bromine isotopes (Z=35) from the reaction 731MeV ^{86}Kr + ^{197}Au (E/B = 1.84). The pattern is unmistakably that of a partially orbiting system. Figure 10 is the analogous plot for 506MeV ^{86}Kr + ^{197}Au (E/B = 1.28). This system is obviously strongly focussed.

It is possible to estimate the relevance of various models for energy dissipation by studying the correlation between energy loss and mass transfer. Two of the most popular models to describe the observed energy loss are:

1. The one-body dissipation formalism, which ascribes the energy loss to the momentum transfer caused by single nucleons traveling from one nucleus to the other [Blo78].
2. The excitation of giant multipole resonances, which allows the collective vibrational energy to be dissipated due to the large coupling of these resonance states to the single particle states [Bro76].

Very little correlation between energy loss and particle transfer should be observed if the second mechanism is predominant, while the opposite would be true if the first is the dominant dissipation mechanism. Displayed in figure 11 is an example of this type of experimental correlation [Sch77]. It has been shown that the 1-body dissipation mechanism seems to be able to describe the energy loss observed for peripheral collisions quite well [Sve78]. Further discussion of this matter will follow in section IV.D. It is important to point out that a third mechanism for energy dissipation, that due to nucleon-nucleon scattering, is not expected to be important during the initial stages of the interaction, when most of the energy is dissipated. During that time, the intermediate complex is a system of fermions characterized by a small temperature. Since most possible final states for the nucleons are forbidden due to the Fermi statistics, the two-nucleon scattering will be inhibited.

An estimate of the relaxation time for the collective kinetic energy can be performed by exploiting the correlation of the "quasi-elastic" centroid with the angle of observation for systems displaying a two-component spectrum. By assuming that the system rotates with an angular frequency given by

$$\omega = \frac{\ell_{ave}\hbar}{\mu r_o^{2}} \qquad (2.2)$$

(where ℓ_{ave} is the average ℓ-value leading to a deep-inelastic collision, μ is the reduced mass, and r_o is the interaction radius), an approximate relation between angle and interaction time results. By assuming an exponential decay of the centroid of the "quasi-elastic" component with time, one arrives at the following expression for the relaxation time τ_E:

$$\tau_E = \frac{(\theta_{gr} - \theta)}{\omega} \left[\ln \left\{ \frac{<E(\theta_{gr})> - E_o}{<E(\theta)> - E_o} \right\} \right]^{-1} \qquad (2.3)$$

where θ is the observed angle, θ_{gr} is the grazing angle, $<E(\emptyset)>$ is the centroid of the "quasi-elastic" component at angle $\emptyset$, and E_o is the centroid of the "relaxed" component. Analysis of the data displayed in figure 6 indicates that $\tau_E \approx 3x10^{-22}$ sec. As will be seen in later sections, this relaxation time is quite short as compared to that for other observables. One is then justified in speaking of "fast" relaxation of the kinetic energy.

C. Neutron to Proton Ratio

Since most reactions involve projectiles and targets with different neutron-to-proton (N/Z) ratios, some of the earliest work in the heavy ion field was concerned with how these ratios relaxed to a common value [Gal76]. These studies require both charge and mass identification, so most have been carried out using light targets and projectiles. One of the first experiments performed involved the bombardment of ^{58}Ni and ^{64}Ni targets with ^{40}Ar and ^{40}Ca projectiles, which allowed all possible combinations of neutron-rich and neutron-poor targets and projectiles. A typical isotope yield distribution is displayed in figure 12 for the ^{40}Ar + ^{58}Ni entrance channel near the grazing angle for the element chlorine (Z=17). The separation between "relaxed" and "quasi-elastic" energy components in this case is well-defined. In the grazing (quasi-elastic) collision, the most probable isotope formed is ^{39}Cl, which is the result of a single proton being stripped from the projectile. The quasi-elastic events range from ^{34}Cl to ^{41}Cl, with the lower mass isotopes having lower average kinetic energies, indicating that the lower mass events may be due to collisions involving more matter overlap (more energy loss) than the higher mass events. On the other hand, the heaviest isotopes are missing from the relaxed component, indicating that the N/Z ratio has had more time to equilibrate, since the highest masses correspond to the entrance channel asymmetry in N/Z, that of a neutron-rich projectile and a neutron-poor target. For angles forward of the grazing angle (see figure 13), the two-peaked structure of the kinetic energy spectra disappears, but the broad distributions seen reflect the N/Z ratio of the relaxed component at the grazing angle. The above features do not depend strongly upon the bombarding energy.

If one considers the composite system to consist of two touching fragments, the average Z for the light fragment for a given mass fractionation is the one that minimizes the potential energy of the complex, given by

$$V = V^1_{LD} + V^2_{LD} + V_{INT} \tag{2.4}$$

where V^i_{LD} is the liquid drop energy for the ith nucleus and V_{INT} is the interaction energy between the nuclei, consisting of Coulomb repulsion and nuclear attraction. (Note that since the rotational energy depends upon the masses, but not on the charge, it will have no bearing upon this mode.) The results of such a calculation assuming the complex is two touching spherical nuclei for the four systems described above are displayed in figure 14 together with the experimental points. The agreement is quite good for all but the most neutron rich system, in the sense that the gross pattern as a function of asymmetry is reproduced. Calculations using equation (2.4) neglect shell effects and ignore the fact that the nuclei possess excitation energy following the interaction. The de-excitation of the nuclei certainly results in some particle emission, expecially neutrons, which would explain why equation (2.4) deviates most strongly from the experimental points for the most neutron rich system. To check this fact, the effect of evaporation has been included in the calculations, and one can see from figure 14 that the discrepancies between the general trends disappears for all systems.

The model proposed above is actually a representation of the giant E1 resonance (of the Steinwedel-Jensen type [Ste50]) in the intermediate complex. From other theoretical work [Mye77], the width of the resonance is known to be rather well reproduced by

$$\Gamma = \hbar \frac{\overline{v}}{R} \qquad (2.5)$$

where $\overline{v}$ is the average velocity of a nucleon in the system and R is a typical linear dimension of the complex; in this case R is the sum of the radii. From the uncertainty principle, one can convert this width into the relaxation time of the resonance state, given by

$$\tau \approx \frac{\hbar}{\Gamma} = \frac{R}{\overline{v}} \qquad (2.6)$$

For the case of ^{58}Ni + ^{40}Ar, $\tau \approx 1.3\text{x}10^{-22}$ sec.

An experimental estimate of the relaxation time, $\tau_{N/Z}$, can be performed by exploiting the angular correlation observed in figure 13. Using formula (2.3) and substituting the appropriate Z value for E, one arrives at $\tau_{N/Z} \approx 1.3\text{x}10^{-22}$ sec. Comparing this with the estimate of τ_E from the preceding section, one immediately sees that the N/Z mode relaxes even faster than the kinetic energy.

Also, the agreement between the experimental and theoretical relaxation times indicates that one is truly observing the relaxation of the giant E1 resonance in this type of measurement.

D. Gamma-ray Multiplicities

During the course of a deep inelastic collision, angular momentum is transferred from the orbital motion of the nuclei into their intrinsic spins. This has been established by several experimenters by measuring the multiplicity of gamma-rays emitted from the primary fragments in the exit channel [Gla77,Per77,Nat78,Chr78]. Three general features are observed in the multiplicities.

1. For the "relaxed" energy component in the reactions of light systems (where the deep-inelastic products are due to a well-defined angular momentum window), the multiplicities increase with increasing charge asymmetry (decreasing Z) for angles behind the grazing angle, but show little dependence upon asymmetry for angles forward of the grazing angle (see figure 15) [Gla77].
2. For the "relaxed" component in heavy systems (where esentially all impact parameters lead to deep-inelastic events), the multiplicities are essentially independent of angle, and display little dependence upon asymmetry (see figure 16) [Ale78].

3. For the "quasi-elastic" component for all systems, the multiplicities display a strong correlation with the net charge transfer observed (see figure 17).

The source of these de-excitation gamma-rays is well known from compound nuclear studies [Boh69]. In short, the two primary fragments in the exit channel possess both excitation energy and spin angular momentum. The most efficient method for removing both quantities is charged particle emission, but this de-excitation mode is strongly inhibited by Coulomb effects. Therefore, the fragments must rely upon neutron emission to eliminate the excitation energy, with centrifugal barrier effects favoring s-wave neutron emission. The net result is that following particle emission, each fragment finds itself with approximately 8 MeV of excitation energy and most of the spin generated during the collision. Due to the large density of nuclear states, gamma-rays due to single-particle transitions start to compete favorably as a de-excitation mechanism at this point. These gamma-rays are principally E1 multipolarity and emitted in a statistical manner. Such emission occurs until the fragment is in the lowest energy state consistent with the given spin, known as an yrast level. For the large class of nuclei that, in their ground states, have a stable shape deviating significantly from spherical symmetry, the yrast levels are collective rotational states (part of a rotational band) and decay primarily by E2 gamma-emission to the next lower level in the band. Due to the collective nature of these levels, the transitions are strongly enhanced compared to the single-particle transitions leading to the statistical gamma-rays. The collective (or "stretched") E2's are emitted until the fragment reaches its ground state. The bulk of the spin angular momentum is lost in this last stage. Compound nuclear studies [Per77] indicate that the possible emission of charged particles (with a corresponding large loss of angular momentum) almost exactly compensates for the low multipolarity of the statistical gamma-rays, such that the conversion from multiplicity to angular momentum given by

$$\ell = 2M_\gamma \tag{2.7}$$

is fairly accurate. Thus, by measuring the gamma-ray multiplicities, one can estimate the amount of spin in the complex at scission.

In a macroscopic sense, one can picture the following mechanism for the angular momentum transfer [Tsa74]: initially the two nuclei slide upon one another. Tangential friction exerts a torque upon each fragment, causing them to rotate. When the peripheral velocities are equal, the tangential friction no longer acts, and the system has reached the "rolling" stage. At this point, rolling friction acts to reduce the difference in rotational frequencies of the two nuclei, resulting in rigid rotation of the complex. In actuality, both tangential and rolling friction act in concert, but the relaxation time for the tangential friction seems to be much shorter, so the above description is essentially correct. For the rolling case, the spin angular momentum of the fragments is 2/7 of the total angular momentum, independent of the mass asymmetry (see Appendix C). For rigid rotation, the fraction of the total angular momentum involved in the spins of the fragments varies from 2/7 to 1, the former for symmetric fragmentation and the latter for compound nucleus formation. This rigid rotation corresponds to the totally equilibrated situation for the angular momentum transfer.

From inspection of figure 15, one sees that the 90° data exhibits the pattern expected for rigid rotation. From this data, an upper limit on the relaxation time for the angular momentum transfer can be calculated. Assuming that the relaxed energy component for the entrance channel asymmetry observed at $\theta_{lab} = 90^{\circ}$ corresponds to systems which have orbited through 0°, the total angle through which the complex has rotated is $\sim 150^{\circ}$. The rotational frequency for rigidly rotating touching spheres with this asymmetry and assuming $\ell = 70\hbar$ is $\sim 10 \times 10^{22}$ deg/sec. Therefore, an upper limit on the relaxation time for the angular momentum transfer is given by

$$\tau_{\ell} = \frac{\Delta\theta}{\omega} = \frac{150}{10^{23}} = 15\mathrm{x}10^{-22}\,\mathrm{sec} \qquad (2.8)$$

A quick comparison shows that this is the largest relaxation time observed so far in the thesis.

E. Charge (Mass) Distributions

Due to technical improvements which originated at Berkeley [Fow75], the charge of the light primary fragment is easily and accurately measured in deep inelastic collisions. The charge distributions for the "relaxed" energy component display the following characteristics (see figures 18-20):

1. At angles in the region of the grazing angle, the charge distributions observed are narrow, indicative of very short interaction times, and the centroids of the distributions coincide with the projectile Z.
2. At forward angles, the distributions are somewhat broader. Drift of the centroid may or may not be observed.
3. At backward angles, the distributions are very broad, and measurable drifts of the centroid are often seen.

If the charge distribution were truly relaxed, one should observe distributions similar to those seen for fission products-- i.e. the yield for a given Z depends upon the potential energy of the saddle point through which the shape must evolve in order to decay into the channel specified by the asymmetry Z. Examples of this ridge-line potential is shown in figure 21. If the total energy available to the compound nucleus is E, then the excitation energy of the complex at the ridge line is E - V(Z), where the potential is measured with respect to the compound nucleus. The probability of decaying with asymmetry Z depends upon the potential through the density of states at the saddle point, which is a function of the excitation energy of the shape:

$$Y(Z) \sim \rho[E - V(Z)] \tag{2.9}$$

where $\rho[E^*]$ is the level density functional. If $V(Z) \ll E$, one can expand the level density about E to arrive at

$$Y(Z) \sim e^{-V(Z)/T} \tag{2.10}$$

where $T^{-1} = \left.\frac{d\ln\rho[x]}{dx}\right|_{x=E}$ is the nuclear temperature. This type of yield distribution is displayed in figure 21 for the potential labeled $\ell = 50\hbar$.

A comparison of figures 18-20 and 21 indicates that the charge distributions at all observed angles are still far from equilibrium, although the backward angle data shows strong tendencies for approaching this limiting shape. Exploitation of the angular correlation again allows an estimate of the relaxation time to be made. A comparison of the data taken at 10° and 35.4° from figure 18, using appropriate substitutions in equation (2.3), results in the estimate

$$\tau_Z \approx 60\text{x}10^{-22}\text{sec} \qquad (2.11)$$

the largest relaxation time observed thus far.

F. Angular Distributions

Much attention has been focussed on the total angular distribution and the angular distributions for different asymmetries for the "relaxed" energy component. A correlation between the shape of the total angular distribution (forward or side peaked) and the ratio of the bombarding energy to the interaction barrier (E/B) has been described by Mathews and coworkers [Mat77]. Such a correlation indicates that a system with $E/B \lesssim 1.6$ exhibits a well-defined side peak in the total angular distribution, while one with $E/B > 1.6$ has a forward peaked distribution. With the knowledge of the relaxation time for the energy from section II.B, one can substantiate this correlation from the average kinematics of the relaxed component.

Assume that the projectile follows a Coulomb trajectory (with ℓ_{ave} units of angular momentum) into the interaction radius, traversing an angle θ_1. The complex then rotates with the average rotational frequency for a time

$$t = \tau_E \ln(10) \tag{2.12}$$

which is the time necessary for 90% of the excess energy to be dissipated. The projectile then follows a Coulomb trajectory with the reduced energy (θ_2). The "relaxed" peak will then appear at an angle

$$\theta = \pi - (\theta_1 + \bar{\omega}t + \theta_2) \tag{2.13}$$

Due to the energy loss, the kinematical broadening of the peak will be quite large ($\Delta\theta = 30^\circ - 40^\circ$), so if $\theta < 30^\circ$, the angular distribution will appear forward peaked, while for $\theta > 30^\circ$, the side peak will be well defined. Table I is a comparison of some experimental data with the accompanying value of θ as calculated by equation (2.13). This substantiates the E/B correlation, since all quantities calculated in equation (2.13) are essentially dependent only upon the ratio E/B.

The most striking feature of the angular distributions for different charge (mass) asymmetries is the apparent relaxation of the angular distributions with increasing net charge transfer (see figures 22-25). The relaxed shape of the angular distribution is 1/sin θ, which indicates that the reaction intermediate is long-lived compared to the rotational period and that the number of partial waves involved is large. The fact that the angular distributions are more forward (side) peaked for the projectile, and the increasing relaxation for asymmetries farther removed from the entrance channel asymmetry indicates that the time necessary for the complex to evolve to the observed asymmetry increases as the required net charge transfer increases.

As noted in section II.E, a dynamically controlled drift of the charge distributions is sometimes observed [Gal75,Mor76]. The direction of the drift is related to the slope of the asymmetry potential, with a negative slope driving the system toward symmetric fragments, and a positive slope tending towards more asymmetric divisions. Due to this drift, one would expect the angular distributions to equilibrate more slowly in the direction of the drift than in the other direction. Figures 26 and 23 display this fact for two systems which have the opposite tendencies.

G. Summary and Conclusions

While it was not obvious from the energy or charge distributions that deep inelastic reactions differed from compound nucleus reactions, the characteristic shapes of the angular distributions and their Z-dependence unequivocally rule out compoumd nucleus reactions. One is assured, then, that the deep inelastic products are due to a different mechanism (or the same mechanism at different stages of relaxation) than compound nucleus reactions. As stated in the introduction, the deep inelastic reactions seem to bridge the void between the two extremes observed in light particle induced reactions.

The aforementioned hierarchy in relaxation times is now complete:

$$(\tau_{N/Z} = 1.3) < (\tau_E = 3) < (\tau_\ell = 15) < (\tau_Z = 60) \qquad (2.14)$$

where all times are in units of 10^{-22} sec. From this hierarchy, one observes that all modes equilibrate much faster than the charge (mass) asymmetry mode. This fact, coupled with the large widths observed in the charge distributions, lends support to the Diffusion Model (described in chapter IV) in which the charge-asymmetry mode is treated as a stochastic process (approach to equilibrium), the N/Z and radial kinetic energy modes are considered instantaneous, and the angular momentum dissipation depends deterministically upon the mass transfer. By keeping track of the dynamics and folding over all impact parameters, the experimental observables (energy, charge and angular distributions) can be calculated and compared with experiment. Secondary processes (γ-ray multiplicities, fission probabilities, etc) can also be described. The succeeding chapters will describe the model, the calculated results, and the comparison with experiment.

Chapter III

Microscopic Derivation of a Master Equation

As stated in the introduction, the main purpose of this thesis is to describe a plausible model which reproduces the experimental observables of deep inelastic collisions and, more important, to provide a simple physical picture of the interactions which lead to the observed data. It will be shown in chapter IV that the distributions in the observables are consistent with a stochastic mass transfer process during the time of interaction between the two nuclei. It is the purpose of this chapter to show under what conditions the time-dependence of the macroscopic observables for strongly interacting quantal systems can be described by stochastic methods [Zwa64]. The projection method used was first applied to this situation by Norenberg [Nor75].

A. Restatement of the Many-body Problem

Let H denote the hamiltonian for the system with orthonormal wave packets $|\psi_i(t)>$ such that

$$i\hbar<\psi_j(t)|\frac{\partial}{\partial t}\psi_i(t)> = \delta_{ij}<\psi_j(t)|H\psi_i(t)> \qquad (3.1)$$

These orthonormal wave functions can be thought of as representing the possible eigenstates of the separated nuclei, suitably orthogonalized to account for the region of overlap. The wave function for the system can be expanded in terms of these orthonormal wave functions

$$|\Phi(t)\rangle = \sum_i \alpha_i(t)\,|\psi_i(t)\rangle \qquad (3.2)$$

where the $\alpha_i(t)$ are occupation amplitudes for the channels. This expansion can be inserted into equation (3.1) to yield

$$i\dot{\alpha}_j(t) = \sum_i U_{ji}(t)\,\alpha_i(t) \qquad (3.3)$$

where

$$U_{ji}(t) = \begin{array}{lll} \hbar^{-1}\langle\psi_j(t)|H\psi_i(t)\rangle & j\neq i & (3.4a) \\ 0 & j=i & (3.4b) \end{array}$$

The result in equation (3.3) can alternatively be expressed ~~in terms of the density matrix $\rho_{ij} = \alpha_i\alpha_j^*$ as:~~

$$i\dot{\rho}_{ji}(t) = \sum_{n,m} L_{ji,nm}(t)\,\rho_{nm}(t) \qquad (3.5)$$

where the Liouville operator is given by

$$L_{ji,nm}(t) = U_{jn}(t)\,\delta_{im} - U_{mi}(t)\,\delta_{jn} \qquad (3.6)$$

As is obvious from equation (3.5), L is a tetradic; it relates one element of a matrix to a linear combination of all matrix elements. The algebra of tetradics and matrices is isomorphic to that of matrices and vectors if one considers the density matrix to be a vector in the superspace $\mathcal{H} \otimes \mathcal{H}^*$, where $\mathcal{H}$ is the total hilbert space of the hamiltonian H. If a vector in the superspace is denoted by $|\ )$, then equation (3.5) becomes

$$\frac{d}{dt}|\rho(t)\Big) = -iL(t)|\rho(t)\Big) \qquad (3.7)$$

The components in the original representation are $\rho_{ji} = (ji|\rho)$ and $L_{ji,nm} = (ji|Lnm)$. Thus one is left with the formal solution

$$|\rho(t)\Big) = e^{-itL(t)}|\rho(0)\Big) \qquad (3.8)$$

While this expression is well-defined in terms of an expansion of the exponential operator, the real power of the superspace formalism lies in the resolvent form of the solution. If the Laplace transform of the density operator is

$$\hat{g}(p) = \int_{0}^{\infty} dt\ e^{-pt}\hat{\rho}(t) \qquad (3.9)$$

then the formal operator solution for the transform of equation (3.7) is

$$\hat{g}(p) = \frac{1}{p+iL}\hat{\rho}(0) \qquad (3.10)$$

This fact, along with the property that the inverse Laplace transform of a product is a convolution, will be used below.

At this point, it is desirable to separate the density operator, or more precisely, its Laplace transform, into diagonal and non-diagonal parts through the application of a projection operator D, whose definition in the original representation is

$$D_{ij,kl} = \delta_{ij}\delta_{ik}\delta_{jl} \tag{3.11}$$

It is easy to verify that D has the desired property. The projection operator and its complement can be used to separate $\hat{\rho}$, $\hat{g}(p)$ and equation (3.10) into diagonal and non-diagonal parts as follows:

$$\hat{\rho} = D\hat{\rho} + (1-D)\hat{\rho} \equiv \hat{\rho}_1 + \hat{\rho}_2 \tag{3.12a}$$

$$\hat{g}(p) = \hat{g}_1(p) + \hat{g}_2(p) \tag{3.12b}$$

$$p\hat{g}_1(p) - \hat{\rho}_1(0) = -iDL\hat{g}_1(p) - iDL\hat{g}_2(p) \tag{3.12c}$$

$$p\hat{g}_2(p) - \hat{\rho}_2(0) = -i(1-D)L\hat{g}_1(p) - i(1-D)L\hat{g}_2(p) \tag{3.12d}$$

By solving equation (3.12d) for $\hat{g}_2(p)$ and substituting into equation (3.12c), one arrives at the Laplace transform of the master equation for the system

$$\begin{aligned} p\hat{g}_1(p) - \hat{\rho}_1(0) = -iDL\hat{g}_1(p) - iDL\frac{1}{p+i(1-D)L}\hat{\rho}_2(0) \\ - DL\frac{1}{p+i(1-D)L}(1-D)L\hat{g}_1(p) \end{aligned} \tag{3.13}$$

Upon application of the inverse Laplace transform, the following master equation results:

$$\frac{d\hat{\rho}_1(t)}{dt} = -iDL\hat{\rho}_1(t) - iDLe^{-i(1-D)Lt}\hat{\rho}_2(0)$$

$$-\int_0^t d\tau\ DLe^{-i\tau(1-D)L}(1-D)L\hat{\rho}_1(t-\tau) \qquad (3.14)$$

One sees immediately that, if the density operator is initially diagonal--i.e. $\hat{\rho}_2(0) \equiv 0$, then equation (3.14) is closed in the diagonal part of the density operator. This condition, usually called the assumption of initial random phases, is often assumed.

It is quite straight forward to show that the first term on the rhs of equation (3.14) is identically 0. By assuming initial random phases, equation (3.14) becomes

$$\frac{d\rho_{mm}(t)}{dt} = -\int_0^t d\tau \sum_n \Xi_{mmnn}(\tau)\rho_{nn}(t-\tau) \qquad (3.15a)$$

where $\Xi_{mmnn}(t) = [L(t)e^{-it(1-D)L(t)}(1-D)L(t)]_{mmnn}$ (3.15b)

Thus it is seen that the equation of motion for the density matrix depends upon its value at all previous times, with the coupling described by the memory kernel $\Xi_{mmnn}(t)$. If the physical situation is such that individual channels cannot be observed (such as observing the mass-asymmetry degree of freedom in deep inelastic collisions), one can resort to coarse graining, which is the process of dividing up the entire hilbert space into subspaces $\mathcal{H}_\mu$, with the elements of a given subspace all possessing a common value for some macroscopic observable. Then, equation (3.15a) can be rewritten as

$$\frac{dP_\nu(t)}{dt} = -\sum_\mu \int_0^t d\tau K_{\nu\mu}(\tau) P_\mu(t-\tau) \qquad (3.16a)$$

where $P_\mu(t) \equiv \sum_{m\in\mathcal{H}_\mu} \rho_{mm}(t)$ (3.16b)

$$K_{\nu\mu}(t) \equiv [d_\nu d_\mu]^{-1} \sum_{\mu,\nu} \Xi_{mmnn}(t) \qquad (3.16c)$$

and d_μ is the total number of channels in the subspace $\mathcal{H}_\mu$.

Equation (3.16a) still represents a formal solution to the many-body problem in which there are no initial correlations. In order to use this formalism, it is necessary to make certain approximations.

B. Derivation of a Master Equation

A quick perusal of equation (3.16a) indicates that the time evolution of the system depends upon all previous times. This is the expected behavior for a deterministic system. A system which can be described by a master equation, on the other hand, has had all long-time correlations removed, since a master equation approach implies that the process is Markovian. Qualitatively, then, one sees that a master equation approach will be accurate if two conditions are met:

1. The probabilities P_μ must remain constant in the time scale necessary for the correlations to decay away.
2. The time scale of interest (interaction time) must be

small compared to the Poincare recurrence time, which is the time necessary for a system to approach its initial conditions in phase space to any arbitrary accuracy.

Norenberg [Nor75] has shown that if one assumes stochastic properties for the coupling matrix elements $U_{ij}(t)$, then a master equation for the probabilities P_ν results

$$\frac{dP_\nu(t)}{dt} = \sum_\mu W_{\nu\mu}(t)[d_\nu P_\mu(t) - d_\mu P_\nu(t)] \tag{3.17a}$$

where

$$W_{\nu\mu}(t) = \hbar^{-2}\tau_{mem}^{(\nu\mu)}(t)<<|U_{nm}|^2>_\nu>_\mu \tag{3.17b}$$

$$\tau_{mem}^{(\nu\mu)}(t) = [2\pi]^{\frac{1}{2}}\hbar[\sum_i (<|U_{mi}|^2>_\mu + <|U_{ni}|^2>_\nu)] \tag{3.17c}$$

$$<f_m>_\mu = d_\mu^{-1} \sum_{m\in\mathcal{H}_\mu} f_m \tag{3.17d}$$

The quantities τ_{mem} are the correlation times discussed above, and estimates for the mass-asymmetry degree of freedom lead to values of 10^{-23}-10^{-22} sec. The relaxation times for the probabilities, τ_{rel}^{μ}, are of the same order of magnitude as the interaction times, τ_{int}, as shown by the sizable widths of the measured mass distributions. These times are of the order 10^{-21}-10^{-20} sec. Thus one sees that the first condition is met. The recurrence time can be estimated as $\tau_{rec}=2\pi\hbar/D$ where D is the average energy level spacing. The high density of states involved in these deep inelastic collisions cause $\tau_{rec} \approx 10^5\tau_{int}$. Thus the second condition is also met.

While the results of this and the previous section could be used as the basis of calculations for nuclear interactions, its sole purpose here is to indicate that a master equation approach is plausible for deep inelastic collisions from first principles. This is sufficient to permit the development of the diffusion model of chapter IV where more cognizance of the known properties of nuclear matter can be taken. Its eventual justification lies in its agreement with measured experimental data.

C. Fokker-Planck Simplification

In order to better appreciate the physical situation described by a master equation of the type in equation (3.17a), it is necessary to discuss Markov processes in general, and to look at appropriate limiting forms [Rei65]. In the following, the coordinate of interest (x) is assumed to be continuous and its domain is the entire real line.

By definition, a Markov process is one in which the joint probability distribution p_2 given by

$$p_2(x_1,t_1;x_2,t_2)dx_1dx_2 \qquad (3.18)$$

which is the probability of finding x in (x_1,x_1+dx_1) at time t_1 and in the range (x_2,x_2+dx_2) at time t_2, describes the process completely. This is certainly not true for dynamical systems, where x(t) depends upon the value of x at all previous times. It is useful to rewrite equation (3.18) in terms of conditional probabilities:

$$p_2(x_1,t_1;x_2,t_2) = p_1(x_1,t_1)P(x_2,t_2-t_1|x_1) \qquad (3.19)$$

where p_1 is the probability of finding x in (x_1,x_1+dx_1) at time t_1 and $P(y,\tau|z)$ is the probability of finding x at y given that x was at z time τ in the past. Using the expression in (3.19), one can write an equation for the probabilities p_1 as

$$p_1(x,t+\tau) = \int_{-\infty}^{\infty} dx_o \; P(x,\tau|x_o)p_1(x_o,t) \qquad (3.20)$$

All this equation states is that if the probabilities p_1 are known at some earlier time t, then the value at time $t+\tau$ is due to contributions from all positions x_o via equation (3.20).

A taylor expansion of equation (3.20) about t for small τ can be performed, resulting in

$$\tau\frac{\partial p_1}{\partial t}(x,t) = \int_{-\infty}^{\infty}dx_1P(x,\tau|x_1)p_1(x_1,t) - p_1(x,t)\int_{-\infty}^{\infty}dx_1P(x_1,\tau|x) \qquad (3.21)$$

The second integral on the rhs of equation (3.21) is identically unity, since it says that the system must go somewhere in time τ. If one defines Λ such that

$$\Lambda(x,y) = \lim_{\tau\to 0} \frac{1}{\tau} P(x,\tau|y) \qquad (3.22)$$

then one is left with the following master equation

$$\frac{\partial\phi}{\partial t}(x,t) = \int_{-\infty}^{\infty} dy[\Lambda(x,y)\phi(y,t) - \Lambda(y,x)\phi(x,t)] \quad (3.23)$$

where $\phi \equiv p_1$. This is the continuous version of equation (3.17a). Care must be taken in taking the limit in equation (3.22). It is necessary that τ become small compared to the relaxation time for the probabilities, but must be large enough that the Markov approximation is still adequate. Since the validity of these assumptions has been substantiated in the previous section, it is assumed that the limit exists and is well-defined.

In the following, it is informative to rewrite equation (3.23) as

$$\frac{\partial\phi}{\partial t}(x,t) = \int_{-\infty}^{\infty} d\xi[\Lambda(x,x-\xi)\phi(x-\xi,t)] - \phi(x,t) \quad (3.24)$$

where a change of variable from y to $x-\xi$ has occurred. Now, if the relative change in x in a time τ is small ($|\xi| << 1$), one can expand the integrand in powers of ξ about the value $\Lambda(x+\xi,x)\phi(x,t)$ to yield

$$\Lambda(x,x-\xi)\phi(x-\xi,t) = \sum_{n=0}^{\infty} \frac{(-\xi)^n}{n!} \frac{\partial^n}{\partial x^n}[\Lambda(x+\xi,x)\phi(x,t)] \quad (3.25)$$

Substituting (3.25) into (3.24), one arrives at

$$\frac{\partial\phi}{\partial t}(x,t) = \sum_{n=1}^{\infty} \frac{(-1)^n}{n!} \frac{\partial^n}{\partial x^n}[\phi(x,t)\int_{-\infty}^{\infty} d\xi\,\xi^n \Lambda(x+\xi,x)] \quad (3.26)$$

Defining

$$\mu_n(x) \equiv \int_{-\infty}^{\infty} d\xi \ \xi^n \Lambda(x+\xi, x) \qquad (3.27)$$

the final form of the Fokker-Planck equation results:

$$\frac{\partial \phi}{\partial t}(x,t) = \sum_{n=1}^{\infty} \frac{(-1)^n}{n!} \frac{\partial^n}{\partial x^n}[\mu_n(x)\phi(x,t)] \qquad (3.28)$$

Traditionally, one considers only the first two terms in the sum of equation (3.28).

$$\frac{\partial \phi}{\partial t}(x,t) = -\frac{\partial}{\partial x}[\mu_1(x)\phi(x,t)] + \frac{1}{2}\frac{\partial^2}{\partial x^2}[\mu_2(x)\phi(x,t)] \qquad (3.29)$$

The coefficient μ_1 corresponds to the average velocity along the x coordinate of the mean of the probability distribution, and μ_2 describes the time development of the second moment of the distribution. This formulation, with the assumption of constant μ_i's , has been used by several authors [Nor74,Sch77] to describe the observed distributions in deep inelatic reactions.

Chapter IV

Diffusion Model for Deep Inelastic Collisions

A. General Principles Behind the Diffusion Model

From the considerations in chapter II, it should be apparent that one observes distributions in all observables which display varying degrees of relaxation. This difference in relaxation times can be viewed as follows: as the two nuclei come into contact during the collision, a "window" opens up allowing nucleons to travel from one nucleus to the other (or alternatively, the potential barrier between the two potential wells of the nuclei decreases as the nuclei approach). Due to the collective velocity of the nucleus whence it originated, each nucleon deposits energy and angular momentum when it is captured in the other nucleus. There is an average flux of nucleons traveling in each direction (from projectile to target and vice versa), and one can quickly see that the transfer of energy and angular momentum will depend upon the sum of these fluxes. The motion of the mass asymmetry, on the other hand, will depend upon the difference of the fluxes, and will, in general, have a longer relaxation time than the energy or the angular momentum. This is substantiated by the hierarchy of relaxation times determined in chapter II. In this single particle picture, the relaxation of energy and angular momentum depends upon the mass transfer in a deterministic way. The measured distributions in these quantities can be related to the fluctuations in the particle fluxes, and more important, to the geometrical folding due to the large number of partial waves. One sees, therefore, that an adequate description of the time evolution of the system should consist of the following points:

1. Since the number of nucleons in each nucleus is small, the fluctuations in the one-sided flux of nucleons can be quite large. Due to these large fluctuations and the essentially random nature of the process, one should be able to describe the time dependence of the mass asymmetry of the complex in terms of a master equation or Fokker Planck approach.
2. In a deterministic way, the values of the excitation energy and nuclear spins for each asymmetry are known as a function of time.
3. The distributions in the lab will reflect the values at the time the nuclei stop interacting, folded over impact parameter, with possible modifications due to secondary processes.

The implementation of these points occurs in the following manner:

1. A dynamical model which has reasonable success in predicting the energy loss is used to determine the average overlap of the nuclei along the trajectory

and the interaction time of the collision.

2. Assuming this overlap to hold for all asymmetries, a master equation is used to calculate the time dependent populations of possible asymmetries.
3. The spins of the nuclei are determined from these populations in an iterative manner.
4. Assuming that the complex decays at time t with a probability distribution centered at the interaction time from 1 above, the final distributions can be calculated.

Sections IV.B through IV.E will deal with each of these points of the model in detail.

B. Classical Model for Nuclear Dynamics

A model for the collision of idealized nuclei has been developed using the proximity potential for the real part of the nuclear interaction potential and proximity friction to describe the damping of the motion [Ran78]. The nuclei are assumed to remain spherical throughout the collision. The coordinates considered (see figure 27) are the internuclear separation r, the angle this line of centers makes with the incident direction θ, and the angles θ_1, θ_2 each nucleus makes with the incident direction. The inertias for these coordinates are the reduced mass μ, the relative moment of inertia μr^2, and the spin moment of inertias I_i, respectively, where $I_i = \frac{2}{5} M_i R_i^2$, M_i and R_i corresponding to the mass and radius of the spherical nucleus i. The potential energy consists of the point-charge Coulomb repulsion and the nuclear proximity potential [Blo77]. From these considerations, the conservative motion is described by the Lagrangian

$$\mathcal{L} = \frac{1}{2}\mu\dot{r}^2 + \frac{1}{2}\mu r^2\dot{\theta}^2 + \frac{1}{2}I_1\dot{\theta}_1^2 + \frac{1}{2}I_2\dot{\theta}_2^2 - \frac{Z_1Z_2e^2}{r} + 4\pi\bar{R}b\gamma\Phi(r-C_1-C_2) \tag{4.1}$$

where $\dot{\theta}$, $\dot{\theta}_1$, $\dot{\theta}_2$ denote the angular velocities for the relative motion, spin 1 and spin 2, respectively. The expression for the proximity potential is described in Appendix D, and is a measure of the attraction of the two nuclei due to the strong nuclear force. The damping due to the proximity friction [Ran78] can be summed up in the following expression for the Rayleigh dissipation function

$$\mathcal{F} = \pi n_0\bar{R}b\ \Psi(r-C_1-C_2)[2\dot{r}^2 + (r\dot{\theta}-r_1\dot{\theta}_1-r_2\dot{\theta}_2)^2] \tag{4.2}$$

where r_1,r_2 are the distances of the respective nuclear centers from the window between them. Appendix D can again be consulted for more details on the form of $\mathcal{F}$.

Armed with the Lagrangian and the Rayleigh dissipation function, the time evolution of the reaction system in the absence of net mass transfer is given by the following set of dynamical equations [Whi44]:

$$\frac{d}{dt}\frac{\partial \mathcal{L}}{\partial \dot{q}} = \frac{\partial \mathcal{L}}{\partial q} - \frac{\partial F}{\partial \dot{q}} \tag{4.3}$$

where q is one of the four variables described above. The rate of energy loss of the system is given by

$$\dot{E} = -2F \tag{4.4}$$

where E is the sum of kinetic and potential energies. The simultaneous integration of the set of equations (4.3) describes the trajectory of the system. The integration of equation (4.4) along the trajectory yields the energy loss associated with the trajectory. Displayed in figure 28 are examples of the time dependence of various quantities determined from this set of equations.

The main purpose of these dynamical equations is to provide information on average dynamical quantities describing the intermediate complex. The first quantity of interest is the interaction time, which is simply the time necessary for the system to return to the interaction radius, since no damping of the motion occurs for larger internuclear separations. Examples of this quantity, and in particular, its ℓ-dependence are shown in figure 29. For comparison, the analogous quantity in the absence of dissipation is also shown. One quickly observes that the dissipation causes the interaction times for very central collisions to dramatically increase. The second desirable quantity is the average internuclear separation along the trajectory, average in the sense of the number of particle exchanges occurring at each separation. This quantity, $\bar{r}(\ell)$, is calculated as

$$\bar{r}(\ell) = \frac{\oint dr\ r\Psi(r-C_1-C_2)[2\mu(E-V(r))]^{-\frac{1}{2}}}{\oint dr\ \Psi(r-C_1-C_2)[2\mu(E-V(r))]^{-\frac{1}{2}}} \qquad (4.5)$$

The Ψ function (described in Appendix D) is proportional to the flux of nucleons at a particular internuclear separation and the term $dr[2\mu(E-V(r))]^{-\frac{1}{2}}$ is simply the time interval spent in the vicinity of separation r. Obviously, the path integral implies integration along the trajectory given by the solution of equations (3.3). It is this quantity $\bar{r}(\ell)$, or more appropriately the overlap $\delta(\ell)$ given by

$$\delta(\ell) = \bar{r}(\ell) - C_T \qquad (4.6)$$

where C_T is the sum of the central radii of the two nuclei, which allows evaluation of the driving potential for the solution of the charge-asymmetry master equation. This topic is discussed in the next section.

For sufficiently light systems, the integration of equations (3.3) sometimes leads to orbits which never return to the interaction radius. This behavior is due to the frozen density assumption (nuclei remain spherical), which causes pockets to develop in the interaction potential for small impact parameters (see figure 30). This behavior is highly unphysical, since the nuclei are most certainly free to explore other shapes during the course of the collision, thereby eliminating the pocket. Therefore, for those systems which displayed this behavior, the value of the lifetime and the overlap have been extrapolated using the values obtained for non-trapped trajectories. This extrapolation procedure is not expected to cause serious error, since those systems which exhibit the trapped orbits also have sizable compound nucleus cross sections as calculated by the master equation (see section IV.C).

C. Master Equation Description of Charge Transfer

As described in section III.B, under conditions which are rather well satisfied in deep-inelastic collisions, a master equation may be used to describe the time evolution of certain observables of heavy-ion reactions. In particular, it is of interest to explore this possibility for the charge(mass) asymmetry degree of freedom, which was shown in section II.E to be the slowest equilibrating collective mode. A master equation approach is favored due to the following three facts:

1. The observed Z-distributions are generally far from equilibration.
2. No oscillation of the most-probable Z about the equilibrated value is observed.
3. The Z-distributions display quite large widths.

The first two points are consistent with two possible physical interpretations; 1) the charge asymmetry mode is overdamped or 2) the charge asymmetry mode is underdamped, but the period of oscillation is very large compared with the interaction times. The second possibility is inconsistent with the large widths observed, since the drift and spread of the Z-distributions must be related by the fluctuation-dissipation theorem [Rei65]. (The large widths indicate a large fluctuating force affecting the collective mode, which could cause the collective motion to be strongly damped, contrary to the underdamped assumption.) Therefore, the charge distribution may be described by a master equation.

In its simplest form, the master equation for the charge asymmetry mode is written as

$$\dot{\phi}_Z = \sum_{Z' \neq Z} [\Lambda_{ZZ'}\phi_{Z'} - \Lambda_{Z'Z}\phi_Z] \qquad (4.7)$$

where the asymmetry is labelled by the charge of one fragment, the ϕ_Z's represent the probability for a given asymmetry Z, and Λ_{ij} is the transition matrix element from state j to state i. Obviously, all of the physics is involved in finding expressions for the matrix elements. Before pursuing that goal, it is informative to estimate the size of the matrix elements.

Suppose each asymmetry is equally likely to be populated. Then the matrix element Λ should be of the following form

$$\Lambda \sim n_o \sigma \qquad (4.8)$$

where n_o is the bulk flux of charges(protons) and σ is the window area through which the charges must travel to enter the other nucleus. Substituting typical values for n_o and σ in equation (4.8), one arrives at the following order of magnitude estimate

$$\Lambda \sim 1 \text{ proton} / 10^{-22}\text{sec} \qquad (4.9)$$

Implicit in this formulation is the fact that the proton transfers are uncorrelated, so the sum in equation (4.7) can be restricted to $Z'=Z+1$. (Randrup has shown that in a quantum mechanical treatment of the mass transfer, the two body operators cancel when determining the net mass flux [Ran77].) Also, since the kinetic energy is damped quite rapidly, most of the charge transfers occur at temperatures in the range of 1-3 MeV. It has been well established that residual interactions are washed out at these temperatures [Hui72].

By extending some of the notions described in [Ran78], one finds that the Fokker-Planck formulation for the mass-asymmetry mode should have coefficients of the following form (in the limit of no residual interactions):

$$\mu_1^A = 2n_o^A \sigma F_A / \mathcal{T} \qquad (4.10a)$$

$$\mu_1^A = 2n_o^A \sigma \qquad (4.10b)$$

where n_o^A is the mass flux of nuclear matter in the bulk, σ is the effective window area and $F_A / \mathcal{T}$ is the driving force of the mass-asymmetry in units of the available energy in the mass-asymmetry mode, $\mathcal{T}$. In previous formulations of the model [Mor75], it has been assumed that the mode was purely classical, with result that $\mathcal{T} = 2T$, where T is the nuclear temperature. More recent investigations into the matter have led to the conclusion that the relevant energy to consider is the average kinetic energy of the diffusing nucleons above the single particle potential barrier. This average kinetic energy, or more important, the ratio

$$\Xi(s,T) \equiv \frac{\mathcal{T}(s,T)}{\frac{3}{5}T_F} \qquad (4.11)$$

where s is the separation between the two potential wells, T_F is the nucleon fermi energy ($T_F \approx 37$MeV), and T is the nuclear temperature, is displayed in figure 31 for some representative temperatures. Note that for large overlaps ($s \lesssim 0$), $\Xi \approx 1$ for all T, and for small overlaps ($s \gtrsim 3$), $\Xi \approx 2T$, consistent with the classical formulation. The derivation of Ξ is given in Appendix A.

Due to the rapid equilibration of the N/Z ratio (see section II.C), the neutron and proton transfers are completely correlated, implying the following relationships between the Fokker-Planck coefficients for charge and mass transfer:

$$\mu_1^Z = \alpha^{-1}\mu_1^A \tag{4.12a}$$

$$\mu_2^Z = \alpha^{-2}\mu_2^A \tag{4.12b}$$

where $\alpha=A_T/Z_T$ is the A/Z ratio for the composite system. Noting that $n_o^A=\alpha n_o^Z$ and $F_Z=\alpha F_A$, one arrives at

$$\mu_1^Z = 2\alpha^{-1}n_o^Z\sigma F_Z \;/\; \tau \tag{4.13a}$$

$$\mu_2^Z = 2\alpha^{-1}n_o^Z\sigma \tag{4.13b}$$

Given equation (4.7), one can calculate the quantities μ_1^Z, μ_2^Z from the Λ's as

$$\mu_1^Z = -\Lambda_{Z-1,Z} + \Lambda_{Z+1,Z} \tag{4.14a}$$

$$\mu_2^Z = \Lambda_{Z-1,Z} + \Lambda_{Z+1,Z} \tag{4.14b}$$

where the restriction on the sum in equation (4.7) has been included explicitly. Inverting equations (4.14), the following expressions for the Λ's ensue:

$$\Lambda_{Z\pm1,Z} = \frac{\mu_2^Z}{2}[1 \pm F_Z \;/\; \tau] \tag{4.15}$$

Since the Λ's must remain positive, the bracketed term may be considered to be the first two terms in an expansion of an exponential, and the following expressions result:

$$\Lambda_{Z\pm1,Z} = \frac{n_o^Z \sigma}{\alpha} e^{\pm F_Z/T} \qquad (4.16)$$

This is the final expression for the matrix elements of equation (4.7).

The driving force F_Z is derived from the driving potential energy for the charge asymmetry mode. This potential energy, V(Z), can be calculated in the following manner:

$$V(Z) = V_{LD}(Z) + V_{LD}(Z_T - Z) + V_{INT} + V_{ROT} \qquad (4.17)$$

where $V_{LD}(Z)$ is the liquid drop energy for a spherical nucleus with charge Z and mass $A = \alpha Z$, Z_T is the total charge of the composite system, V_{INT} is the Coulomb plus Proximity potential for the complex shape and V_{ROT} is the rotational energy for the shape. In this paper, the complex shape is assumed to be two spheres separated by the distance

$$d(Z) = C(Z) + C(Z_T - Z) + \delta(\ell) \qquad (4.18)$$

where C(Z) is the central radius for the spherical nucleus with charge Z and $\delta(\ell)$ is the overlap calculated in section IV.B. Once d(Z) is known, V_{INT} can be calculated for each asymmetry. The rotational energy depends upon how the entrance channel angular momentum ℓ is shared between orbital motion ℓ_{rel} and the spins of the two nuclei ℓ_1, ℓ_2 . Section IV.D describes how these quantities are calculated. Suffice it to say that once ℓ_{rel}, ℓ_1, ℓ_2 are known, the rotational energy will be given by

$$V_{ROT} = \frac{\hbar^2}{2}\left[\frac{\ell_{rel}^2}{\mu_Z d(Z)^2} + \frac{\ell_1^2}{I_1} + \frac{\ell_2^2}{I_2}\right] \tag{4.19}$$

where μ_Z is the reduced mass for the asymmetry Z and I_1, I_2 have the same meanings as in section IV.B.

Examples of V(Z) for several systems are displayed in figures 32-36. The driving force F_Z is simply given by

$$F_Z = -\frac{dV}{dZ}(Z) \tag{4.20}$$

A comparison with equation (4.13a) indicates that the drift of the centroid of the Z-distribution is determined by the slope of the potential energy curve. This fact leads to the following conclusions:

1. If the entrance channel asymmetry corresponds to a positive slope in V(Z) (see figures 32,33), then the drift of the Z-distribution should cause smaller Z's to be populated more quickly than the larger Z's. This difference in population times should show up on the angular distributions, as described in section II.E.
2. If the entrance channel asymmetry corresponds to a negative slope in V(Z) (see figures 35,36), then the above behavior should be inverted.

The fact that this behavior has been observed for appropriately chosen experimental systems was early proof of the influence of the driving potential in the motion of the charge-asymmetry.

It is informative at this juncture to compare equation (4.16) with earlier forms for the matrix elements. In reference [Mor75], the following expression for the matrix elements was used:

$$\Lambda_{Z\pm1,Z} = \kappa f_{ZZ'} e^{(V_Z - V_{Z\pm1})/2T} \tag{4.21}$$

The definition of terms in this equation were such that it is exactly equivalent with the classical form of equation (4.16) if

$$\kappa = \frac{n_o^Z}{\alpha} \tag{4.22}$$

where κ was a constant varied to fit the data, and had the value $0.05\mathrm{fm}^{-2}/10^{-22}\mathrm{sec}$. Evaluation of n_0^Z/α for the same system yields

$$\frac{n_o^Z}{\alpha} = 0.051\ \mathrm{fm}^{-2}\ /\ 10^{-22}\mathrm{sec} \tag{4.23}$$

Thus it is seen that the classical limit of equation (4.16) is equivalent to previous parameterizations of the matrix elements.

The final master equation for describing the charge-asymmetry degree of freedom is:

$$\dot{\phi}_Z = \frac{n_o^Z}{\alpha} \sum_{Z'=Z\pm1} \sigma_{ZZ'} [e^{(V_{Z'}-V_Z)/T} \phi_{Z'} - e^{(V_Z-V_{Z'})/T} \phi_Z] \qquad (4.24)$$

Equation (4.24) can be solved by standard matrix techniques (see Appendix E) to arrive at the values for $\phi_Z(t)$. Displayed in figures 37-41 are the $\phi_Z(t)$ calculated for the potential energy curves displayed in figures 32-36. Note the drift of the centroid for short times, and the spreading of the distributions. The long time equilibrated behavior is also noticable, where the Z-distributions depend upon the Boltzmann factors $e^{-V_Z/T}$, as for fission yields.

One of the factors which complicates discussion of deep-inelastic reactions is compound nucleus formation. Intuitively, one would expect the most central collisions to result in compound nucleus formation, at least for the lighter systems, due in large part to the large nuclear overlaps attained in these collisions and the long interaction times involved. The master equation approach allows one to estimate the compound nucleus formation due to motion along the mass asymmetry coordinate.

The clearest experimental signature of a compound nucleus event is the detection of a heavy evaporation residue, which has usually lost several charges during the de-excitation of the compound nucleus. The other possible de-excitation mode for the highly excited compound nucleus is via fission [Van73]. As described in section II.E, the expected yield for the fission products will reflect the

Boltzmann factors $e^{-V_Z/T}$, where V_Z is the potential energy of the saddle point shape through which the nucleus must evolve to fission and T is the effective temperature at the saddle. As seen in figures 37-41, the equilibrated Z-distributions from the master equation will be indistinguishable from these yields, aside from a possibly different temperature. Furthermore, the kinetic energies measured for the fission fragments will be identical to the kinetic energies of the relaxed peak. The only easily obtainable experimental observable which can truly distinguish between compound nucleus or deep-inelastic products with the same Z is the angular distribution. If the fragments are due to CN, the angular distribution must be symmetric about 90^{o} , reflecting the fact that the compound nucleus is long lived compared to the rotational period. The DI products should have an angular distribution with varying degrees of side or forward peaking; but, if the product in question is very far removed from the entrance channel asymmetry, such that a long interaction time is necessary for its formation, the angular distribution may also be symmetric about 90^{o}, for the same reason as the compound nucleus products. One sees, therefore, that the cross section measured for symmetric fragmentations in deep-inelastic collisions may be the sum of cross-section produced by two vastly different mechanisms. A careful measurement of the branching ratios of the complex into various channels could differentiate between CN and DI products. Unfortunately, this type of data is not yet commonly available.

The master equation may be used to calculate the compound nucleus cross section in the following manner; for very large asymmetries (small Z's), the shape of two spheres differs negligibly from the compound nucleus shape. For some critical Z-value, Z_{cr} (a value of 4 is used in the calculations), all asymmetries with $Z < Z_{cr}$ and $Z > Z_T - Z_{cr}$ are considered to be compound nuclei. Due to the large number of channels available to the compound nucleus for de-excitation, it is assumed that the probablity going into compound nucleus formation is lost from the charge asymmetry mode. In this way, a time-dependent probability for compound nucleus formation is given by

$$P_{CN}(t) = 1 - \sum_{Z=Z_{cr}}^{Z_T - Z_{cr}} \phi_Z(t) \tag{4.25}$$

The sum of P_{CN} over all impact parameters then yields the compound nucleus cross section due to motion along the mass asymmetry coordinate. This quantity may be compared with the measured evaporation residue cross sections.

D. Angular Momentum Transfer Accompanying Mass Transfer

As observed in section II.D, angular momentum is transformed from orbital motion into intrinsic spin of the nuclei during the course of a deep-inelastic collision. In this section, a model is described for calculating the contribution to the angular momentum transfer due to the exchange of nucleons through the window between the nuclei [Sve78].

The quantities of interest are $\ell_1(Z,\ell)$, $\ell_2(Z,\ell)$; that is, the spin of the two nuclei as a function of asymmetry Z and of the entrance channel angular momentum ℓ. As described in section II.D, most of the spin can be measured as γ-rays, and one can correlate the multiplicity observed with the spins by the simple formula

$$M_\gamma(Z) = \frac{1}{2}[\ell_1(Z,\ell) + \ell_2(Z,\ell)] \qquad (4.26)$$

Before describing the model to calculate these spins, it is informative to explore possible limiting cases and the expectations for realistic situations.

Since the quantity which can be directly compared with experiment is the sum of the spins, attention can be focussed upon the complementary quantity, the relative orbital angular momentum, denoted by $\ell_{rel}(Z,\ell)$. If, during the course of a reaction, no angular momentum is transformed into spin, then the quantity ℓ_{rel} is a constant, independent of Z, and equal to ℓ . At the opposite extreme, if the reaction occurs in a way such that the angular momentum is equilibrated -- i.e. the complex rotates as a rigid rotor at scission, then ℓ_{rel} is given by

$$\ell_{rel}(Z,\ell) = \frac{\mu_Z d_Z^2}{\mu_Z d_Z^2 + I(Z) + I(Z_T - Z)} \ell \qquad (4.27)$$

These two behaviors are shown for a system of two touching spheres for various ℓ-waves in figures 42a and 42b.

These two extreme behaviors can be viewed as that resulting from collisions with short and long average interaction times, respectively. (Due to the fluctuations experienced by the system, it is expected that a distribution in the lifetime of the complex will result. To populate those channels which require a large net mass transfer, one will be sampling the wings of this distribution.) The larger the time necessary to form a given asymmetry, the larger the number of nucleons which have been exchanged between the nuclei, which implies a larger damping of the relative orbital angular momentum into the spins of the nuclei. If one focusses on a near grazing impact parameter, which is characterized by a short average lifetime of the complex, the expected qualitative behavior of ℓ_{rel} is displayed as the line of asterisks(*) in figure 42c. For asymmetries near the entrance channel value Z_p, the cross section is expected to be dominated by the short time behavior, resulting in very few nucleon exchanges and correspondingly small amounts of angular momentum transfers. For Z's quite far removed from Z_p, a correspondingly larger amount of time is necessary to populate them, resulting in larger amounts of angular momentum transfer. Now shift the focus to a more direct collision, with a much longer interaction time. Here the expected behavior is displayed as the lower solid line in figure 42c. Due to the large interaction time, the angular momentum transfer is expected to be nearly complete for all asymmetries, leading to the rigid rotation limit.

In order to quantitatively measure the accuracy of the qualitative estimates above, a model has been formulated to calculate the transfer of angular momentum from relative motion to spin. Due to the short relaxation times observed for the kinetic energy, the assumption of infinite radial friction is made -- i.e. all radial kinetic energy is dissipated at the interaction radius. One then considers a system of two spheres separated by a Z and ℓ dependent distance $d(Z,\ell)$ [see equation (4.18)] with ℓ-units of orbital angular momentum and no spin. In order to calculate how ℓ_{rel} is transferred into ℓ_1, ℓ_2 and their functional dependence upon Z, two steps are needed:

1. The complex, initially at asymmetry Z_p, is assumed to live a time t and to decay with asymmetry Z. The average rate of change of the charge of nucleus 1 is given by

$$\dot{Z}_1 = (Z-Z_p) / t \qquad (4.28)$$

Due to the rapid N/Z equilibration (see section II.C), one may write

$$\dot{A}_1 = (Z-Z_p)\alpha \;/\; t \qquad (4.29)$$

where A_1 is the mass of nucleus 1 and α is the A/Z ratio for the composite system. The average rate of nucleon transfer from one nucleus to the other is $n_o\sigma$, where n_o is the bulk flux of nuclear matter and σ is the effective window between the nuclei (see [Ran78]). By forcing the system to arrive at asymmetry Z at time t, an asymmetry in the right (r_{12}) and left (r_{21}) nucleon transfer rates is imposed, which can be written as

$$r_{12} = n_o\sigma - \tfrac{1}{2}\dot{A}_1 \qquad (4.30a)$$

$$r_{21} = n_o\sigma + \tfrac{1}{2}\dot{A}_1 \qquad (4.30b)$$

Knowing these transfer rates, the following system of coupled differential equations for the spins and the orbital angular momentum (in the absence of rolling friction) can be written

$$\dot{\ell}_1 = d_1[r_{12}d_1(\dot{\theta}-\dot{\theta}_1)+n_o\sigma d_2(\dot{\theta}-\dot{\theta}_2)]/\hbar \qquad (4.31a)$$

$$\dot{\ell}_2 = d_2[n_o\sigma d_1(\dot{\theta}-\dot{\theta}_1)+r_{21}d_2(\dot{\theta}-\dot{\theta}_2)]/\hbar \qquad (4.31b)$$

$$\dot{\ell}_{rel} = -(\dot{\ell}_1+\dot{\ell}_2) \qquad (4.31c)$$

where all quantities have been defined in section IV.B. Simultaneous integration of equations (4.29) and (4.31) from 0 to t, subject to the proper initial conditions, results in values for $\ell_1(Z,\ell,t)$ and $\ell_2(Z,\ell,t)$, which represent the spins as a function of Z and ℓ if the complex is forced to live a time t.

2. The functions $\ell_1(Z,\ell)$ and $\ell_2(Z,\ell)$ are obtained by integrating out the time dependence. A gaussian lifetime probability distribution $\Pi(t)$ about the interaction time $\tau(\ell)$ from section IV.B is used with a variance given by

$$\sigma^2(\ell) = 0.25\tau(\ell) \qquad (4.32)$$

It will be shown in chapters V and VI that such a functional form for the variance predicts the experimental observables reasonably well. It is also necessary to weight the $\ell_i(t)$ by the probability for forming the system Z at time t. This function, $\phi(Z,t)$ is calculated using the master equation (or associated Fokker Planck equation) from section IV.C. Thus one is left with

$$\ell_i(Z,\ell) = \int_0^\infty dt\ \ell_i(Z,\ell,t)\Pi(t)\phi(Z,t)/\int_0^\infty dt\ \Pi(t)\phi(Z,t) \quad (4.33)$$

The above scheme for calculating the angular momentum transfer is actually an iterative one, since the values of $\ell_1, \ell_2, \ell_{rel}$ must be known for each Z in order to calculate the probability $\phi(Z,t)$. Two questions concerning the model's validity immediately come to mind:

1. Does the sequence of iterations converge uniquely, independent of the initial assumption about the ℓ's?
2. How many iterations must be executed before the ℓ-values reasonably approximate the convergence values?

In order to answer these questions, a suitable convergence criterion must be established. Define the relative root mean square deviation in ℓ_{rel} from the (i-1)th to the ith iteration by:

$$\Delta^{i}_{rms} = [\frac{1}{N}\sum_{Z}\langle \ell^{i}_{rel}(Z,\ell) - \ell^{i-1}_{rel}(Z,\ell)\rangle^{2}]^{\frac{1}{2}} \qquad (4.34)$$

where N is the number of terms in the sum and ℓ^{j}_{rel} is the value of the orbital angular momentum at the jth iteration. A reasonable criterion is that

$$\Delta^{i}_{rms} < 0.001 \qquad (4.35)$$

i.e. that the relative deviation be less than 0.1%.

Displayed in figure 43 are the ℓ_{rel} values converged to given three different initial assumptions concerning the 0th iteration ℓ-values. As can be seen, the final values are indistinguishable. Thus question 1 is answered in the affirmative.

Figure 44 shows the successive values for ℓ_{rel} for various iterations i. It seems quite reasonable, in the sense of no loss of significant physical information, to truncate the iterative sequence after the first step, in light of this figure.

Plotted in figure 45 are the curves $\ell_{rel}(Z,\ell)$ in the Z-TKE plane for several different ℓ-values for the reaction 1156MeV ^{136}Xe + ^{197}Au. The qualitative behavior predicted above is quite apparent. It will be shown in Chapter V that this formalism gives approximately correct results for the γ-ray multiplicities.

E. Dynamics

Sections IV.B-IV.D have outlined models for the calculation of the probability of forming a given asymmetry during a collision and the amount of spin angular momentum the complex possesses for each asymmetry. In order to compare these quantities with experimental data, it is necessary to perform some average dynamics in order to correlate the calculated quantities with angle. To do so, one may proceed in the following manner.

A basic concept of classical scattering theory is the ability to generate the angular distribution for a given channel if the corresponding deflection function is known [Gol50]. This concept may be formally exploited in the following sense: assume that the complex lives a time t. Then, for a given asymmetry Z (channel focussed upon), the classical deflection function Θ is given by

$$\Theta(\ell;Z,t) = \pi - [\theta_{in}(\ell)+\bar{\omega}(Z,\ell)t+\theta_{out}(\ell_{rel}(Z,\ell);Z)] \qquad (4.36)$$

where θ_{in} is the Coulomb angle scattered through in reaching the interaction radius, θ_{out} is a grazing Coulomb scattering angle for asymmetry Z with $\ell_{rel}(Z,\ell)$ units of orbital angular momentum, and $\bar{\omega}(Z,\ell)$ is the average rotational frequency of the complex. This average frequency may be calculated as

$$\bar{\omega}(Z,\ell) = \sum_{i=Z_p}^{Z} \frac{\ell_{rel}(i,\ell)\hbar}{\mu_i d_i^2} \Big/ (|Z-Z_p|+1) \tag{4.37}$$

where all quantities have been previously defined. If, for a given partial wave, the fraction of the particle flux which produces the channel being considered is T_ℓ , then the differential cross section is given by

$$\frac{d\sigma}{d\Omega}(\theta) = 2\pi\bar{\lambda}^2 \sum_\ell \frac{\ell}{\sin\theta\left|\frac{d\theta}{d\ell}\right|} T_\ell \tag{4.38}$$

where the summation is carried out over all ℓ-waves which result in particle emission at the desired angle θ . In the present adaptation of the theory, T_ℓ and θ are both dependent upon the lifetime of the complex, t. Therefore, one generates the following triple differential cross section:

$$\frac{\partial^3\sigma}{\partial Z\partial\Omega\partial t}(Z,\theta,t) = \frac{2\pi\bar{\lambda}^2}{\sin\theta} \sum_\ell \frac{\ell}{\left|\frac{d\theta}{d\ell}(\ell;Z,t)\right|} \phi(Z,\ell,t) \tag{4.39}$$

where the fraction of flux, T_ℓ , has been explicitly written as the probability function from the solution of the master equation. In order to compare with experiment, it is necessary to remove the time dependence.

From section IV.B, the average lifetime of the complex, $\tau(\ell)$, is known for each partial wave. Due to mass transfer and thermal fluctuations, the complex is expected to have a distribution of lifetimes about this average value, represented by $\Pi(t;\ell)$. Π is expected to be of gaussian shape, and the variance of the distribution should be an increasing function of the average lifetime, since, if the complex lives longer, on the average, the random fluctuations causing the dispersion have longer to operate, resulting in a wider time distribution. Further discussion of Π may be found in Appendix B.

Assuming the existence of Π , the time dependence can be eliminated, resulting in the following expression for the angular distributions:

$$\frac{\partial^2 \sigma}{\partial Z \partial \Omega}(Z,\theta) = \frac{2\pi ƛ^2}{\sin\theta} \int_0^\infty dt \left[\sum_\ell \frac{\ell}{\left|\frac{d\theta}{d\ell}\right|} \phi(Z,\ell,t)\Pi(t;\ell)\right] \quad (4.40)$$

The resulting center of mass angular distributions can now be compared with experiment.

F. Summary

The previous four sections have described the basic components of the diffusion model. They are:

1. Use a dynamical model to calculate the average overlap and interaction time for each partial wave.
2. Using the overlaps from 1, calculate the master equation probabilities.
3. From these probabilities, determine the angular

momentum transfer.

4. Calculate the angular distributions from the average dynamics.

By far, the crudest portion of the model is the average dynamics. These quantities are the ones which will be most drastically influenced by other degrees of freedom. It is therefore expected that the angular dependence of observables calculated by the model should have the correct qualitative features, but that hidden degrees of freedom may strongly influence the data.

Chapter V

Comparison of Experimental and Calculated Quantities

The model described in chapter IV has been implemented numerically on the CDC 7600 computer at the Lawrence Berkeley Laboratory. Operationally, a grid of points in the angular momentum range spanning the interaction region $[0,\ell_{max}]$ is selected, called ℓ_i. Dynamical calculations following the model in 4B are performed for each ℓ_i, in order to determine the overlap δ_i and the interaction time τ_i. The master equation of section IV.C is then solved, using a driving potential calculated from δ_i, for a grid of time points. The average spin of the two reaction products is then determined from the probabilities calculated above and using the formalism described in section IV.D. Finally, the time information is integrated out to arrive at the final dynamical variables.

As may be discerned from the above discussion, the following quantities are available for comparison with the experimental data:

1. $\partial^2\sigma/\partial\Omega\partial Z$ - angular distribution for each Z
2. $d\sigma/dZ$ - integrated Z-distribution
3. $\partial^2 M_\gamma/\partial\Omega\partial Z$ - average gamma-ray multiplicity as a function of Z and angle
4. dM_γ/dZ - average gamma-ray multiplicity as a

function of Z

Due to the crudeness of the dynamical portion of the model, an in depth comparison of the angle dependent quantities is of questionable utility. For this reason, those quantities will only be described for the reaction system ^{86}Kr + ^{197}Au for three incident energies: 506, 620 and 731 MeV. The angle integrated quantities are presented for the following three sets of reactions:

1. 288 MeV ^{40}Ar, 620 MeV ^{86}Kr and 979 MeV ^{136}Xe + ^{197}Au
2. 620 MeV ^{86}Kr + ^{159}Tb, ^{181}Ta and ^{197}Au
3. 506 MeV, 620 MeV and 731 MeV ^{86}Kr + ^{197}Au

In all cases, experimental values are included in the figures, where available. By far, the richness of the data for the Kr + Au excitation function provides the severest test of the model.

A. Angle Integrated Z-distributions

Displayed in figure 46 are the calculated Z-distributions for three different projectiles on ^{197}Au [Mor76,Rus77a,Rus77b]. The abscissa is Z - Z_p, so that the initial asymmetries for the systems lineup at 0. One immediate feature which may be discerned is the gradual shift of the peak of the distribution as the mass of the projectile increases. As the projectile mass increases, the average slope of the driving potential energy at the injection point becomes increasingly negative (see figure 47), thereby driving the cross section peak towards more symmetric mass asymmetries. This general feature was one of the earliest indications of the approach to equilibrium nature of these reactions. The data points for the Ar and Xe induced reactions are representative spectra for a single lab angle, while the rest of the data points throughout this section are the actual integrated cross sections. It is apparent that the model predicts the correct trend as one changes projectile. It should be noted that the energies used all give the same approximate E/B values.

Figure 48 illustrates the same quantity for 620 MeV ^{86}Kr bombarding three different targets [Rus77a,Woz78,Cau78b]. The success of the model in predicting this quantity in this energy and mass region is easily observed.

As a final test of the model, the same quantity for the reaction system ^{86}Kr + ^{197}Au at three bombarding energies [Sch78] is displayed in figure 49. With the exception of the low Z side of the 506 MeV curve, the calculations agree with the data quite well, although even the "bad" region of the low energy curve is quite impressive when compared to other attempts to fit similar quantities. Also one must remember that there are no adjustable parameters in the model.

The general accuracy of the predictions of the model may be attributed to the self-consistency of the lifetimes and overlaps and their seeming balance with the master equation formalism for the asymmetry distribution. As stated previously, the justification for many of the physical arguments presented in chapter IV lies in their ability to describe the physical situation. As for the integrated Z-distributions, the model seems to do quite well.

The discrepancy for the low Z side of the low energy system could be due to many factors, not the least of which is the assumption concerning the shape of the intermediate complex. The frozen density assumption may be considered to be a "sudden" approximation in that the densities remain spherical throughout the reaction. The lower the incident energy, the more adiabatically one might expect the reaction to proceed, thus allowing the nuclear densities to readjust as the reaction proceeds. This different family of complex shapes is known [Nix65] to result in driving potentials which favor symmetric shapes over asymmetric ones, thus removing some of the cross section from the overpopulated low Z products. This added degree of freedom may also favor higher compound nucleus cross section, thus removing the excess cross section seen in the deep-inelastic channel.

B. Angular Distributions

Figures 50, 51 and 52 display the calculated vs. measured angular distributions for the Kr + Au reaction system at 506, 620 and 731 MeV bombarding energies, respectively [Sch78]. Three general features emerge from these figures:

1. With the exception of the previously noted difficulty for Z's below the projectile at 506 MeV, the magnitude of the cross sections for each Z are correct.
2. For Z's in the neighborhood of the projectile, the position of the side peak, as well as the magnitude of the cross section in the neighborhood of the peak are correctly predicted.
3. The model dynamics tends to overpopulate angles behind the peak value and to underestimate the cross section for angles forward of the peak.

The discrepancies noted in 3 above would seem to indicate that the average dynamics used to arrive at the angle dependent cross sections may not be correct. The fact that the peaks are fairly well reproduced indicates that the dynamics performs well in the neighborhood of the grazing angular momentum, which results in the peak cross section. The discrepancies are greatest for angles which are populated by more central impact parameters. Possible solutions to this problem are discussed in chapter VI.

C. Gamma Multiplicity Distributions

In order for this comparison to be a self-consistent test of the model, the M_γ values should only be compared for systems in which the model correctly predicts the angular distributions. The only system described above for which gamma-ray multiplicity information is available is 620 MeV ^{86}Kr + ^{197}Au [Ale78]. As will be seen, this one system is sufficient to show some discrepancy between experiment and theory.

Displayed in figure 53 are the measured and calculated values for the grazing angle of this reaction. It is immediately obvious that the calculated results have the same general Z dependence as the data. This strong increase in multiplicity with increasing net mass transfer is indicative of a tight correlation between mass transfer and angular momentum transfer. The fact that the calculated values are generally lower than the experimental ones is to be expected, since not all of the experimental gamma-rays carried 2 units of angular momentum, as was supposed in the calculated results. Also, other mechanisms have been shown to be capable of generating sizeable amounts of angular momentum.

Figure 54 shows the experimental and calculated quantities for $\theta_{cm} = 45^o$ and $\theta_{lab} = 30^o$, respectively. The same general trend is observed for both sets of points. The gross discrepancy in the neighborhood of the projectile Z is due to the fact that the calculated values include contributions from the quasi-elastic cross section while the experimental ones do not. Again, the calculated values are smaller than the experimental ones.

Armed with only this information, one would be tempted to say that there are approximately 5 E1 gamma-rays emitted in each reaction, as well as all of the predicted E2's, and the calculations and experiment would agree. Unfortunately, the theory does not predict the experimentally observed angle independence of the M_γ values for each Z. As may be observed in figure 55, the calculations predict a gradual decrease in the multiplicities as θ increases, while the experimental values are essentially angle-independent. The fact that there are many mechanisms by which gamma-rays may be created, and that the model only considers one of them implies that the multiplicities calculated in this way should probably not be expected to reproduce all of the experimentally observed features.

Chapter VI

Summary of Results

For reactions in which the frozen density assumption is probably valid, as evidenced by the incident energy, the diffusion model does quite well in predicting the charge distributions for a wide range of targets and projectiles. The angular distributions display the correct general trends, as well as predicting the angular position and cross-section of the side peak for Z's in the neighborhood of the projectile Z. The underestimate of the forward angle cross-section and overestimate of the backward angle cross-section seems to indicate that the dynamics used in the model is in error for central collisions. The gamma-ray multiplicity distributions are quite good for the quasi-elastic portion of the cross-section, but the calculated distributions as a function of angle do not predict the angle independence observed experimentally for heavy systems.

The angular distribution problem mentioned above can be tackled in a variety of ways, one of which is being attempted by G. Mathews [Mat79]. His approach is to perform a Monte Carlo calculation, using the functional form of the charge flux function from chapter IV to calculate the charge-asymmetry at each step of the calculation. Of course, the dynamics is then performed correctly at each step.

The gamma-ray multiplicity distribution problem is more difficult to solve. Theoretically, more cognizance of the other possible mechanisms for gamma-ray production (statistical, bending modes, etc.) should be taken in the model. Operationally, it is not clear how to include them in the present model.

Another possible solution to the general problem discussed in this thesis has been pursued by W. Norenberg and coworkers [Nor74,Nor75,Nor76a,Nor76b,Ayi76a,Ayi76b]. In their work, the Fokker-Planck formulation of the mass diffusion is solved concurrently with the equations of motion for the other collective variables. Their expressions for the FP coefficients and the form factors is based upon a different model than those of the present work. Their method has experienced reasonable success in describing the relaxed cross section, and has been extended to describe the angular momentum distributions.

Another major effort to predict these quantities using a vastly different physical approach is due to H. Weidenmuller and coworkers [Aga75,Aga76,Wei77]. In their approach, a transport equation for deep-inelastic collisions is derived from a random matrix model for the form factors for inelastic scattering and transfer reactions. The inherently quantum mechanical nature of this effort has caused their predictions to be less impressive than those of the semi-empirical models, such as the diffusion model, but it will also probably lead to the correct description of all variables and their correlations as the calculations are further refined.

Appendix A

Average Kinetic Energy in Mass-asymmetry Mode

A quantity of major importance in calculating the transition matrix elements is the average kinetic energy available for the transition, which was written as T in equation (4.10). The physical situation which prevails can be seen in figure 56. The two nuclear centers are separated by a distance r, and the total single particle potential looks like the bottom curve in figure 56. As can be seen, there is a minimum energy ε_{min} below which particles in one nucleus cannot classically enter the other nucleus. The relevant energy available to cause a net transition involving ΔV MeV of energy is the average energy above the barrier of those nucleons having energies $\varepsilon \geqslant \varepsilon_{min}$. If $P(\varepsilon)$ represents the probability of having a nucleon with energy ε, then one can write

$$T = \frac{\int_{\varepsilon_{min}}^{\infty} d\varepsilon\ P(\varepsilon)[\varepsilon-\varepsilon_{min}]}{\int_{\varepsilon_{min}}^{\infty} d\varepsilon\ P(\varepsilon)} \qquad (A.1)$$

From the work of Randrup [Ran78], one can calculate the value of ε_{min}. The ψ function (see appendix D) represents the fraction of the nucleons which can enter the other nucleus for a zero temperature fermi gas at a separation s. In other words,

$$\psi(s) = \int_{\varepsilon_{min}}^{\varepsilon_F} d\varepsilon\ P_o(\varepsilon) \tag{A.2}$$

where $P_o(\varepsilon)$ is the probability distribution for a T=0 fermi gas. Since

$$P_o(\varepsilon) = \frac{3}{2}\frac{\varepsilon^{1/2}}{\varepsilon_F^{3/2}} \tag{A.3}$$

one finds that

$$\frac{\varepsilon_{min}}{\varepsilon_F} = [1 - \psi(s)]^{2/3} \tag{A.4}$$

With the knowledge of ε_{min}, one can evaluate T in equation (A.1) for a non-zero temperature fermi gas, with $P(\varepsilon)$ of the form

$$P(\varepsilon) = \frac{1}{N}\frac{\varepsilon^{1/2}}{1+e^{(\varepsilon-\mu)/T}} \tag{A.5}$$

where $\mu(T)$ is the chemical potential, T is the nuclear temperature in MeV, and N normalizes the probability distribution $P(\varepsilon)$. Since the number of nucleons must be constant, independent of the temperature, $N = \frac{2}{3}\varepsilon_F^{3/2}$, and μ is determined implicitly from

$$\int_0^\infty d\varepsilon \frac{\varepsilon^{1/2}}{1+e^{(\varepsilon-\mu)/T}} = \frac{2}{3}\varepsilon_F^{3/2} \tag{A.6}$$

It can be easily shown [Rei65] that

$$\mu(T) = \varepsilon_F[1 - \frac{\pi^2}{12}(\frac{T}{\varepsilon_F})^2 + \cdots] \tag{A.7}$$

so, one can evaluate T since μ is now known for a given temperature. Explicitly,

$$T = \varepsilon_F \left\{ \frac{I(\frac{3}{2}, \frac{\varepsilon_{min}}{\varepsilon_F}, \frac{T}{\varepsilon_F}, \frac{\mu}{\varepsilon_F})}{I(\frac{1}{2}, \frac{\varepsilon_{min}}{\varepsilon_F}, \frac{T}{\varepsilon_F}, \frac{\mu}{\varepsilon_F})} - \frac{\varepsilon_{min}}{\varepsilon_F} \right\} \qquad \text{(A.8a)}$$

where

$$I(\alpha,\eta,\tau,\beta) = \int_\eta^\infty \frac{dx \quad x^\alpha}{1+e^{(x-\beta)/\tau}} \qquad \text{(A.8b)}$$

or in terms of $\Xi(s,T)$

$$\Xi(s,T) = \frac{T(s,T)}{\frac{3}{5}\varepsilon_F} \qquad \text{(A.9)}$$

Examples of $\Xi(s,T)$ are plotted in figure 31.

Appendix B

The Lifetime Distribution Function

From the discussion of section IV.B, the average lifetime of the complex is known for each impact parameter from the dynamical model. It is expected that due to mass transfer and thermal fluctuations, there will be a distribution of lifetimes centered around this average value. It is the purpose of this appendix to outline the general features of this distribution.

In an attempt to calculate the smear due to mass transfer, the dynamical model of section IV.B was modified by the inclusion of a driving term which forced the asymmetry to change. By correlating the exit channel asymmetry with the interaction time, a rough estimate of the variance due to mass transfer was obtained. In all cases tested,

$$\frac{\sigma^2}{\tau} << 0.001 \qquad (B.1)$$

indicating that very little smear is due to the mass transfer itself.

In order to estimate the effects of thermal fluctuations, a few simplifications may be made. The motion of the system along the radial coordinate can be likened to the motion of a Brownian particle in one dimension in a constant field of force [Rei65,Cha43]. (For example, motion of a Millikan oil drop in the field between the capacitor plates.) The equation of motion for the Brownian particle is

$$\frac{du}{dt} + \beta u = \kappa + A(t) \tag{B.2}$$

where u is the velocity of the particle, β is the specific viscosity, κ is the specific force and A(t) is the fluctuating force. Using standard techniques for its solution [Cha43], one finds that the probability distribution for the system is given by

$$W(x,t;x_0,u_0) = [2\pi\sigma^2(t)]^{-\frac{1}{2}} e^{-(x-<x(t)>)^2/2\sigma^2(t)} \tag{B.3a}$$

where

$$<x(t)> = x_0 + \frac{\kappa}{\beta}t + (1-e^{-\beta t})[\frac{u_0}{\beta} - \frac{\kappa}{\beta^2}] \tag{B.3b}$$

$$\sigma^2(t) = \frac{T}{2m\beta^2}(2\beta t - 3 + 4e^{-\beta t} - 2e^{-2\beta t}) \tag{B.3c}$$

The time distribution function sought is

$$\Pi(t) = W(x_0,t;x_0,u_0) \tag{B.4}$$

i.e. the probability that the system finds itself back at x_0 after time t. A typical example of $\Pi(t)$ for the nuclear case is plotted in figure 57. The skewed gaussian shape is evident from the figure. A quantity of interest is the functional dependence of the variance of the distribution upon the mean value τ. Plotted in figure 58 are curves of σ^2 vs. τ for various assumptions concerning the relationship between β and κ. The slopes of the curves vary from 0.85 to 1.0, the latter value being an asymptotic one. Therefore, it seems quite reasonable to assume that

$$\sigma^2 = c\tau \qquad (B.5)$$

for some constant c. The curve labelled $\gamma = 1$ is the best approximation to the nuclear case, with the result that

$$c = 0.25 \qquad (B.6)$$

It is this value which is used in all of the calculations performed.

Appendix C

Limiting Angular Momenta for Interacting Spheres

Let us suppose the following physical situation: two spherical nuclei of radii d_1, d_2 with masses m_1, m_2 are sliding over one another. Initially, all of the angular momentum, L(0), is concentrated in the relative motion. If one assumes that the damping of the relative angular momentum is given by one-body dissipation [Blo78], then the following coupled equations of motion result for the spin angular momenta, L_1, L_2:

$$\dot{L}_1 = (n_o\sigma)d_1[d\dot{\theta} - d_1\dot{\theta}_1 - d_2\dot{\theta}_2] \quad (C.1a)$$

$$\dot{L}_2 = (n_o\sigma)d_2[d\dot{\theta} - d_1\dot{\theta}_1 - d_2\dot{\theta}_2] \quad (C.1b)$$

where $d = d_1 + d_2$; $\dot{\theta}_i = L_i/I_i$; $\dot{\theta} = (L_o-(L_1+L_2))/\mu d^2$ (C.1c)

and $n_o\sigma$ is the one-sided transfer rate of mass from one nucleus into the other. Defining $f=n_o\sigma$ and collecting terms, one arrives at

$$\dot{L}_1 = c_{10} + c_{11}L_1 + c_{12}L_2 \quad (C.2a)$$

$$\dot{L}_2 = c_{20} + c_{21}L_1 + c_{22}L_2 \quad (C.2b)$$

where

$$c_{i0} = fd_i dL_o/\mu d^2 \qquad (C.3a)$$

$$c_{i1} = -fd_i[(d/\mu d^2) + (d_1/I_1)] \qquad (C.3b)$$

$$c_{i2} = -fd_i[(d/\mu d^2) + (d_2/I_2)] \qquad (C.3c)$$

The roots of the corresponding set of homogeneous equations are

$$\lambda_\pm = \tfrac{1}{2}[(c_{11}+c_{22}) \pm [(c_{11}-c_{22})^2+4c_{12}c_{21}]^{\frac{1}{2}}] \qquad (C.4)$$

which reduces to

$$\lambda_\pm = \begin{matrix} c_{11} + c_{22} \\ 0 \end{matrix} \qquad (C.5)$$

since the square root term is $(c_{11}+c_{22})$. Therefore, the general solutions to the set of homogeneous equations are

$$L_1(t) = a_- + a_+e^{\lambda_+ t} \qquad (C.6a)$$

$$L_2(t) = -\frac{c_{11}}{c_{12}} a_- + \frac{(\lambda_+-c_{11})}{c_{12}} a_+e^{\lambda_+ t} \qquad (C.6b)$$

The particular solutions of the inhomogeneous equations prove to be linear in time, and the term proportional to t may be eliminated since the spins must assume a finite asymptotic limit. Thus the final solutions are

$$L_1(t) = a_- + a_+e^{{}_+\lambda t} + b_1 \qquad (C.7a)$$

$$L_2(t) = -\frac{c_{11}}{c_{12}} a_- + \frac{(\lambda_+-c_{11})}{c_{12}} a_+e^{\lambda_+ t} + b_2 \qquad (C.7b)$$

The a's and b's are related by

$$\begin{pmatrix} a_- \\ a_+ \end{pmatrix} = - \begin{pmatrix} 1 & 1 \\ -\frac{c_{11}}{c_{12}} & \frac{(\lambda_+ - c_{11})}{c_{12}} \end{pmatrix} \begin{pmatrix} b_1 \\ b_2 \end{pmatrix} \qquad (C.8)$$

which results from the application of the initial conditions $L_1(0)=L_2(0)=0$. Since the b's are solutions in their own right, they may be evaluated by solving

$$\begin{pmatrix} b_1 \\ b_2 \end{pmatrix} = - \begin{pmatrix} c_{11} & c_{12} \\ c_{21} & c_{22} \end{pmatrix}^{-1} \begin{pmatrix} c_{10} \\ c_{20} \end{pmatrix} \qquad (C.9)$$

Thus, one may solve for all quantities in equation (C.7). One may evaluate λ_+ from the expressions for c_{11}, c_{22} to arrive at

$$\lambda_+ = -\frac{7}{2}\frac{f}{\mu} \qquad (C.10)$$

or may define the relaxation time as

$$\tau = \frac{2}{7}\frac{\mu}{f} \qquad (C.11)$$

This expression makes sense physically, since it implies that the relaxation time for a system increases with increasing inertia and decreases with increasing damping. For a typical system, $\tau \sim 3 \times 10^{-22}$ sec , on the same order as the relaxation time for the initial energy.

By solving for b_1, b_2, a_+, a_- , one arrives at the following expressions for the spins:

$$L_1(t) = \left(\frac{2}{7}\frac{d_2}{I_2} - \frac{5}{7}\frac{d}{\mathcal{I}}\right)\left(\frac{d_2}{I_2} - \frac{d_1}{I_1}\right)^{-1}(1-e^{-t/\tau})L_o \qquad (C.12a)$$

$$L_2(t) = \left(\frac{5}{7}\frac{d}{\mathcal{I}} - \frac{2}{7}\frac{d_2}{I_2}\right)\left(\frac{d_2}{I_2} - \frac{d_1}{I_1}\right)^{-1}(1-e^{-t/\tau})L_o \qquad (C.12b)$$

where $\mathcal{I} = \mu d^2$. If one examines the infinite time limit of these expressions, one arrives at

$$L_1(\infty) + L_2(\infty) = \frac{2}{7} L_o \qquad (C.13)$$

regardless of the masses. This, then, is the result asserted in section II.D.

Appendix D

Finite Curvature Effects upon the Proximity Treatment of Nuclear Interactions

The real internuclear potential calculated from the proximity theorem[Blo77] has been shown to accurately account for much of the measured heavy-ion elastic scattering data[Chr76]; it has also been shown to be consistent with some of the measured complete fusion data[Bir78]. The analogous treatment of the single particle flux in heavy-ion reactions[Ran78], and in particular, the resulting energy loss, has also been shown to be not inconsistent with the experimental data. In most cases where comparisons have been carried out, the colliding nuclei have suffered only very grazing collisions, with an accompanying small overlap of nuclear matter. It is in this region of impact parameters that the frozen density assumption of the treatment is expected to be best satisfied.

A question of current interest is to what extent the proximity treatment is valid as the nuclear matter overlap becomes large. Intuitively, one might expect the frozen density approximation to be valid for a large part of the trajectory up to the classical turning point, since that part of the trajectory is traversed in times small compared to the relaxation time of density fluctuations in nuclear matter. Given that its use for large overlaps is justified, this appendix describes a method for the correct calculation of the proximity function Φ [Blo77,Ran78] and the flux function Ψ [Ran78], taking into consideration the finite curvature of the two colliding nuclei. In particular, a simple approximation is described which allows the correct evaluation of Φ, Ψ for asymmetric spheres and which goes over into the known closed form expression for equal spheres[Blo77].

First, it is necessary to review the basic points of the proximity treatment[Blo77]. Assume that one is interested in a quantity F as a function of the separation of the surfaces of the two nuclei, denoted F(s). If the corresponding quantity per unit area, f(s), is known for parallel surfaces, then the proximity theorem states that

$$F(s) = \iint_{\text{Gap}} dxdy \; f(D[x,y]) + \text{corrections} \qquad (D.1)$$

where the surface integral is over the surface areas that oppose each other across the gap, and D[x,y] is the functional for the distance between the two opposing surfaces elements as a function of position on the surface. The corrections are assumed to vanish for large radii of curvature. For cases involving axial symmetry, one may perform the angular integration immediately to arrive at

$$F(s) = \pi \int_{\text{Gap}} (2rdr) \; f(D[r]) \qquad (D.2)$$

where r is the cylindrical coordinate describing the surface. Now, if one can write r^2 as a power series in D -- i.e.

$$r^2 = \sum_{i\geq 0} a_i D^i \tag{D.3}$$

then one may differentiate the above expression, substitute into (D.2) and arrive at the following expression for F:

$$F(s) = \pi \sum_{i\geq 1} i a_i \int_s dD\, D^{i-1} f(D) \tag{D.4}$$

By their definition, the a_i's are unique to a specified geometry; the upper limit in the integrals in equation (D.4) has purposely been left unspecified.

At this point, the usual proximity treatment[Blo77,Ran78] makes the following assumptions: the radii of curvature are large and the function f is short range. These allow the upper limit of the integrals of equation (D.4) to be set to ∞, giving rise to the incomplete moments $F_n(s)$, defined by

$$F_n(s) = \int_s^\infty dD\, D^n f(D) \tag{D.5}$$

The large radii of curvature also allow the evaluation of the coefficients a_i for spheres to be performed approximately as

$$a_1 = 2\overline{R} \tag{D.6a}$$

$$a_i = 0 \; (i > 1) \tag{D.6b}$$

where $\overline{R}=R_1R_2/(R_1+R_2)$ is the "reduced radius". Essentially, the above approximations correspond to replacing the two juxtaposed spherical surfaces by paraboloids with the same radii of curvature. For separations s corresponding to small amounts of nuclear matter overlap, the above approximations are quite good, as will be seen below. Unfortunately, for even moderate overlaps, the finite curvature of the spheres, as opposed to the infinite paraboloids, causes sizeable corrections to the above scheme.

The easiest case to consider is for two equal spheres of radius C, since then the results may be obtained in closed form. In this case, the non-zero coefficients in equation (D.3) are:

$$a_1 = 2\overline{R} + \frac{s}{2} \tag{D.7a}$$

$$a_2 = -\tfrac{1}{4} \tag{D.7b}$$

More important, there is a finite upper limit to the integrals in equation (D.4) given by

$$D_{\text{lim}} = 2C + s \tag{D.8}$$

For grazing collisions, imposition of the finite upper limit in the evaluation of the incomplete moments does not result in appreciable corrections to F. But, as the two nuclei overlap strongly ($s \leq 0$), the upper limit reduces the values of the moments substantially. The size of the correction may be deduced from figure 59, in which are plotted curves displaying $V_p(s) / 4\pi\bar{R}b\gamma$ (see [Blo77] for definition of terms) for various values of C using the correct evaluation, and for the usual approximation (labelled ∞). As stated above, all curves are approximately the same for large separations; as the nuclei overlap more strongly, the correction becomes quite large.

The situation for nuclei characterized by different radii of curvature ($C_1 < C_2$) is more complex. The geometrical situation is displayed in figure 60. In this case, the limiting distance is given by

$$D_{lim} = C_1 + C_2 + s - [C_2^2 - C_1^2]^{\frac{1}{2}} \qquad (D.9)$$

A straightforward evaluation results in

$$r^2 = 2\,\frac{C_1\,C_2}{C_1+C_2}\,(D-s) - \frac{C_1\delta_2^2+C_2\delta_1^2}{C_1+C_2} \qquad (D.10)$$

where the δ_i's are defined in figure 60. As can be quickly seen, the usual proximity treatment relies on the assumption that one can ignore the second term on the right hand side of equation (D.10). It is possible to expand this second term in higher powers of (D-s), but a simple approximation is available to allow an easy evaluation of the proximity functions. This approximation consists of assuming that

$$r^2 = \sum_{i=1}^{2} b_i (D-s)^i \tag{D.11}$$

where $b_1 = 2\overline{R}$ and b_2 is determined from the requirement that

$$r^2 = C_1^2 \text{ when } D = D_{1im} \tag{D.12}$$

Working through the algebra, one arrives at

$$b_2 = \frac{C_1^2 - 2\overline{R}(D_{1im}-s)}{(D_{1im}-s)^2} \tag{D.13}$$

or, in terms of the a_i's in equation (D.3)

$$a_2 = b_2 \tag{D.14a}$$

$$a_1 = 2\overline{R} - 2a_2 s \tag{D.14b}$$

One should note that in the limit that $C_1 = C_2$, one is left with the results in equation (D.7). The effects of these results are displayed for a few typical asymmetric situations in figure 61. Again, the usual function is labelled as ∞. One can see the large discrepancy for even moderate overlaps.

The accuracy of the above approximation can be checked in the following manner: given a value for the cylindrical coordinate r, the value of the distance between the surfaces is given by

$$D(r) = C_1 + C_2 + s + [C_1^2 - r^2]^{\frac{1}{2}} - [C_2^2 - r^2]^{\frac{1}{2}} \qquad (D.15)$$

For a given value of r, one can calculate D(r) from equation (D.15), and then calculate the approximate value r'(D) by substituting this value of D into equation (D.11) and taking the square root. To quantify the situation, if q << 1, where

$$q = [{}_0\int^{C_1} rdr\, [1 - \frac{r'(D(r))}{r}]^2 \,/\, {}_0\int^{C_1} rdr]^{\frac{1}{2}} \qquad (D.16)$$

is the average root mean square relative deviation of r, then the approximation may be said to accurately represent the physical situation. The ratio q has been evaluated for several cases which are summarized in Table II. As can be seen, the values of q indicate that the average relative deviation is always less than 2%.

Appendix E

Solution of the Charge Diffusion Master Equation

From the considerations in section IV.C, one is left with the following master equation for the time dependence of the probability distribution for the charge asymmetry:

$$\frac{d}{dt}\phi_n = \sum_{n'\neq n} \lambda_{nn'}(\phi_{n'}\rho_n - \phi_n\rho_{n'}) \qquad \text{(E.1)}$$

In vector notation,

$$\frac{d}{dt}\vec{\phi} = -\vec{\vec{P}}\,\vec{\phi} \qquad \text{(E.2a)}$$

where

$$P_{nn'} = \begin{array}{ll} \sum_{n''\neq n} \lambda_{nn''}\rho_{n''} & (n = n') \\ -\lambda_{nn'}\rho_n & (n \neq n') \end{array} \qquad \text{(E.2b)}$$

If we define $R_{nn'} = (\frac{\rho_{n'}}{\rho_n})^{\frac{1}{2}} P_{nn'}$, then equation (E.1) becomes

$$\frac{d}{dt}(\rho_n^{-\frac{1}{2}}\phi_n) = -\sum_{n'} R_{nn'}\rho_{n'}^{-\frac{1}{2}}\phi_{n'} \qquad \text{(E.3)}$$

It is desirable to show that $\vec{\vec{R}}$ is a symmetric matrix. It is necessary to consider $n \neq n'$, since R_{nn} is obviously symmetric.

$$R_{nn'} = -\lambda_{nn'}\rho_n(\frac{\rho_{n'}}{\rho_n})^{\frac{1}{2}} = -\lambda_{n'n}\rho_{n'}(\frac{\rho_n}{\rho_{n'}})^{\frac{1}{2}} = R_{n'n} \qquad \text{(E.4)}$$

since

$$\lambda_{nn'} = \lambda_{n'n} \qquad \text{(E.5)}$$

By defining $\psi_n=\rho_n^{-\frac{1}{2}}\phi_n$, one is left with

$$\frac{d}{dt}\vec{\psi} = -\vec{\vec{R}}\,\vec{\psi} \tag{E.6}$$

with $\vec{\vec{R}}$ a symmetric matrix. The solution to equation (E.6) is

$$\vec{\psi}(t) = e^{-t\vec{\vec{R}}}\,\vec{\psi}(0) \tag{E.7}$$

or, in terms of $\vec{\phi}$,

$$\phi_n(t) = \rho_n^{\frac{1}{2}} \sum_{n'} [e^{-t\vec{\vec{R}}}]_{nn'}\rho_{n'}^{-\frac{1}{2}}\phi_{n'}(0) \tag{E.8}$$

Now, if $\vec{\vec{S}}$ is the matrix of eigenstates and $\vec{\vec{r}}$ is the matrix of eigenvalues for $\vec{\vec{R}}$, $e^{-t\vec{\vec{R}}}=\vec{\vec{S}}e^{-t\vec{\vec{r}}}\vec{\vec{S}}^{\dagger}$; since $\vec{\vec{S}}$ is a real matrix, $S^{\dagger}_{nm}=S_{mn}$. Equation (E.8) now becomes

$$\phi_n(t) = \rho_n^{\frac{1}{2}} \sum_{n'} \sum_{m} S_{nm}S_{n'm}e^{-tr_{mm}}\rho_{n'}^{-\frac{1}{2}}\phi_{n'}(0) \tag{E.9}$$

or defining $\gamma_m=\sum_{n'} S_{n'm}\rho_{n'}^{-\frac{1}{2}}\phi_{n'}(0)$, one is left with

$$\phi_n(t) = \rho_n^{\frac{1}{2}} \sum_{m} S_{nm}\gamma_m e^{-tr_{mm}} \tag{E.10}$$

In the situation where all of the probability at time 0 is concentrated in one channel n_o , an especially simple form for γ_m results:

$$\gamma_m = S_{n_o m}\rho_{n_o}^{-\frac{1}{2}} \tag{E.11}$$

References

Aga75 D. Agassi and H.A. Weidenmuller, Phys. Lett., **56B** (1975) 305.

Aga76 D. Agassi, C.M. Ko and H.A. Weidenmuller, preprint MPIH-1976-V25, 1976.

Ale78 M.M. Aleonard, G.J. Wozniak, P. Glassel, M.A. Deleplanque, R.M. Diamond, L.G. Moretto, R.P. Schmitt and F.S. Stephens, Phys. Rev. Lett., **40** (1978) 622.

Art73 A.G. Artukh, G.F. Gridnev, V.L. Mikheev, V.V. Volkov and J. Wilczynski, Nucl. Phys., **A215** (1973) 91.

Ayi76a S. Ayik, B. Schurmann and W. Norenberg, Z. Phys., **A277** (1976) 299.

Ayi76b S. Ayik, B. Schurmann and W. Norenberg, Z. Phys., **A279** (1976) 145.

Bir78 J.R. Birkelund and J.R. Huizenga, Phys. Rev., **C17** (1978) 126.

Blo63 B. Block and H. Feshbach, Ann. Phys., **23** (1963) 47.

Blo77 J.P. Blocki, J. Randrup, C.F. Tsang and W.J. Swiatecki, Ann. Phys., **105** (1977) 427.

Blo78 J. Blocki, Y. Boneh, J.R. Nix, J. Randrup, M. Robel, A.J. Sierk and W.J. Swiatecki, Ann. Phys., 113 (1978) 330.

Boh69 A. Bohr and B.R. Mottelson, Nuclear Structure, volumes 1 and 2, W.A. Benjamin, Inc., Reading, Mass., 1969 and 1975.

Bon75 J.P. Bondorf, J.R. Huizenga, M.I. Sobel and D. Sperber, Phys. Rev., C11 (1975) 1265.

Bro76 R.A. Broglia, C.H. Dasso and A. Winther, Phys. Lett., 61B (1976) 113.

Cau78a B. Cauvin, R.C. Jared, P. Russo, R.P. Schmitt, R. Babinet and L.G. Moretto, Nucl. Phys., A301 (1978) 511.

Cau78b B. Cauvin, R.P. Schmitt, G.J. Wozniak, P. Glassel, P. Russo, R.C. Jared, J.B. Moulton and L.G. Moretto, Nucl. Phys., A294 (1978) 225.

Cha43 S. Chandrasekhar, Rev. Mod. Phys., 15 (1943) 1.

Chr76 P.R. Christensen and A. Winther, Phys. Lett., 65B (1976) 19.

Chr78 P.R. Christensen, F. Folkmann, Ole Hanson, O. Nathan, N. Trautner, F. Videback, S.Y. van der Werf, H.C. Britt, R.P. Chestnut, H. Freiesleben and F. Puhlhofer, Phys. Rev. Lett., 40 (1978) 245.

Col74 P. Colombani, preprint IPNO-PhN-74-21, 1974.

Fow75 M.M. Fowler and R.C. Jared, Nucl. Instr., **124** (1975) 341.

Gal70 J. Galin, D. Guerreau, M. Lefort, J. Peter, X. Tarrago and R. Basile, Nucl. Phys., **A159** (1970) 461.

Gal74 J. Galin, B. Gatty, D. Guerreau, C. Rousset, U.C. Schlotthauer-Voos and X. Tarrago, Phys. Rev., **C9** (1974) 1113.

Gal75 J. Galin, L.G. Moretto, R. Babinet, R. Schmitt, R. Jared and S.G. Thompson, Nucl. Phys., **A255** (1975) 472.

Gal76 J. Galin, J. Phys., **37** (1976) C5-83.

Gla77 P. Glassel, R.S. Simon, R.M. Diamond, R.C. Jared, I.Y. Lee, L.G. Moretto, J.O. Newton, R. Schmitt and F.S. Stephens, Phys. Rev. Lett., **38** (1977) 331.

Gol50 H. Goldstein, Classical Mechanics, Addison-Wesley, Cambridge, Mass, 1950.

Har69 B.G. Harvey, Introduction to Nuclear Physics and Chemistry, Prentice-Hall, Englewood Cliffs, N.J., 1969.

Har77 J.W. Harris, T.M. Cormier, D.V. Geesaman, L.L.

Lee, R.L. McGrath and J.P. Wurm, Phys. Rev. Lett., **38** (1977) 1460.

Hui72 J.R. Huizenga and L.G. Moretto, Ann. Rev. Nucl. Sci., **22** (1972) 427.

Kra74 J.V. Kratz, A.E. Norris and G.T. Seaborg, Phys. Rev. Lett., **33** (1974) 502.

Mah73 C. Mahaux, Ann. Rev. Nucl. Sci., **23** (1973) 193.

Mat77 G.J. Mathews, G.J. Wozniak, R.P. Schmitt and L.G. Moretto, Z. Phys., **A283** (1977) 247.

Mat79 G.J. Mathews, in preparation.

Mor73 L.G. Moretto, D. Heuneman, R.C. Jared, R.C. Gatti and S.G. Thompson, Physics and Chemistry of Fission, 1973, vol. 2 (IAEA, Vienna, 1974)351.

Mor75 L.G. Moretto and J.S. Sventek, Phys. Lett., **58B** (1975) 26.

Mor76 L.G. Moretto, J. Galin, R. Babinet, Z. Fraenkel, R. Schmitt, R. Jared and S.G. Thompson, Nucl. Phys., **A259** (1976) 172.

Mye77 W.D. Myers, W.J. Swiatecki, T. Kodama, L.J. El-Jaick and E.R. Hilf, Phys. Rev., **C15** (1977) 2032.

Nat78 J.B. Natowitz, M.N. Namboodiri, P. Kasiraj, R.

Eggers, L. Adler, P. Gonthier, C. Cerruti and T. Allenan, Phys. Rev. Lett., **40** (1978) 751.

Nix65 J.R. Nix and W.J. Swiatecki, Nucl. Phys., **A71** (1965) 1.

Nor74 W. Norenberg, Phys. Lett., **52B** (1974) 289.

Nor75 W. Norenberg, Z. Phys., **A274** (1975) 241.

Nor76a W. Norenberg, J. Phys., **37** (1976) C5-141.

Nor76b W. Norenberg, Z. Phys., **A276** (1976) 84.

Per77 N. Perrin and J. Peter, presented at the Winter School on Nuclear Physics, Zakopane, Poland, February 1977, IPNO-RC-77-02.

Ran77 J. Randrup, preprint, NORDITA 77/45 (Rev.), 1977.

Ran78 J. Randrup, Ann. Phys., **112** (1978) 356.

Rei65 F. Reif, Fundamentals of Statistical and Thermal Physics, McGraw-Hill, New York, 1965.

Rus77a P. Russo, R.P. Schmitt, G.J. Wozniak, R.C. Jared, P. Glassel, B. Cauvin, J.S. Sventek and L.G. Moretto, Nucl. Phys., **A281** (1977) 509.

Rus77b P. Russo, B. Cauvin, P. Glassel, R.C. Jared, R.P. Schmitt, G.J. Wozniak and L.G. Moretto, Phys. Lett., **67B** (1977) 155.

Sch77 W.U. Schroder and J.R. Huizenga, Ann. Rev. Nucl. Sci., **27** (1977) 465 and references cited therein.

Sch78 R.P. Schmitt, Ph.D. thesis, Lawrence Berkeley Laboratory report LBL-7168, 1978.

Ste50 H. Steinwedel and J.H. Jensen, Z. Naturforsch., **52** (1950) 413.

Sve78 J.S. Sventek and L.G. Moretto, Phys. Rev. Lett., **40** (1978) 697.

Tra77 W. Trautmann, J. de Boer, W. Dunnweber, G. Graw, R. Kopp, C. Lautebach, H. Puchta and U. Lymen, Phys. Rev. Lett., **39** (1977) 1062.

Tsa74 C.F. Tsang, Phys. Scr., **A10** (1974) 90.

Van73 R. Vandenbosch and J.R. Huizenga, Nuclear Fission, Academic Press, New York, 1973.

Van76 R. Vandenbosch, M.P. Webb and T.D. Thomas, Phys. Rev. Lett., **36** (1976) 459.

Wei77 H.A. Weidenmuller, proceedings of the Fall Creek Falls Meeting on Heavy-Ion Collisions, Pikeville, Tennessee, June, 1977.

Whi44 G.T. Whittaker, Analytic Dynamics, Dover Publications, New York, 4th Edition(1944)230.

Wil73 J. Wilczynski, Phys. Lett., **47B** (1973) 484.

Wol74 K.L. Wolf, J.P. Unik, J.R. Huizenga, J.R. Birkelund, H. Freiesleben and V.E. Viola, Phys. Rev. Lett., 33 (1974) 1105.

Woz78 G.J. Wozniak, R.P. Schmitt, P. Glassel and L.G. Moretto, Nucl. Phys., A298 (1978) 169.

Zwa64 R.W. Zwanzig, Physica, 30 (1964) 1109.

Table I

System	E/B	angle	side-peaked
365MeV Cu + Au	1.19	91	yes
220MeV Ar + Au	1.21	90	yes
280MeV Cu + Nb	1.23	87	yes
170MeV Ar + Ag	1.24	81	yes
443MeV Cu + Au	1.45	57	yes
979MeV Xe + Au	1.48	62	yes
629MeV Kr + Au	1.56	50	yes
979MeV Xe + Tb	1.59	52	yes
288MeV Ar + Au	1.58	43	yes
620MeV Kr + Ta	1.62	45	yes
620MeV Kr + Tb	1.71	39	yes
340MeV Ar + Au	1.87	26	no
620MeV Kr + Ag	1.91	26	no
288MeV Ar + Ag	2.11	13	no
340MeV Ar + Ag	2.49	-8	no

Table II

C_1	C_2	q
5	5	0
4	6	0.013
3	7	0.014
2	8	0.010
1	9	0.006

Figure Captions

1. Kinetic energy distributions observed for various Z's in the reaction 288MeV ^{40}Ar + ^{197}Au at various laboratory angles. Note the existence of the relaxed peak for all Z's at all angles and the quasi-elastic component for Z's near the projectile Z (18) and angles near the grazing angle.

2. Same as figure 1 for the reaction 620MeV ^{86}Kr + ^{107}Ag.

3. Save as figure 1 for the reaction 620MeV ^{86}Kr + ^{197}Au.

4. Centroids of the relaxed energy component of the kinetic energy distributions observed in figure 1 as a function of observed Z. The two solid lines are the expected values assuming the complex shape to be two touching spheres and two touching spheroids. Note the Z-independence of the widths of the distributions.

5. Same as figure 4 for the reaction 620MeV ^{86}Kr + ^{197}Au. No decomposition of the energy spectrum into relaxed and quasi-elastic components has been performed. The data for 40.4°, which is approximately the grazing angle, reflects the large cross-section observed for small energy loss, as seen in figure 3. The data averaged over all angles shows the same pattern as that of figure 4.

6. Contours of constant cross-section in the θ_{cm}-E_{cm} plane

for potassium ions (K) in the reaction ^{40}Ar + ^{232}Th [Wil73].

7. Same as figure 6 for various Z's in the reaction 620MeV ^{86}Kr + ^{197}Au.

8. Schematic portrayal of two trajectories in a heavy-ion reaction. Trajectory 1 corresponds to a quasi-elastic reaction product being observed at angle θ , while trajectory 2 corresponds to a relaxed reaction product.

9. Wilczynski diagram (see figure 6) for Z=35 in the reaction 731MeV ^{86}Kr + ^{197}Au. The quasi-elastic peak moves to forward angles as the centroid energy decreases. This is an example of a "partially orbiting" system.

10. Same as figure 9 for the reaction 506MeV ^{86}Kr + ^{197}Au. Here, the quasi-elastic peak displays essentially no angular motion as the energy is dissipated. This is an example of a "strongly focussed" system.

11. Display of energy loss vs. the width of the Z-distribution for the products displaying that energy loss [Sch77].

12. Contours of constant number of events in the E_{lab}- Mass plane for Cl isotopes formed in the reaction 280MeV ^{40}Ar + ^{58}Ni [Gal76].

13. Same as figure 12 for K isotopes at two different

laboratory angles [Gal76].

14. (a) N/Z ratio for each mass for two reactions. The upper smooth curve is that expected for ^{40}Ca + ^{64}Ni from liquid-drop considerations, the lower curve the same quantity for ^{40}Ar + ^{58}Ni. The jagged lines are the measured data points.
(b) Same as (a) above. The triangles correspond to the data and the circles correspond to the smooth liquid-drop calculations modified to include the effects of neutron evaporation [Gal76].

15. Gamma-ray multiplicities for various Z's at various laboratory angles in the reaction 175MeV ^{20}Ne + ^{107}Ag. The solid smooth curves are the values expected from rigid rotors at two ℓ-values. The dashed horizontal lines correspond to the rolling limit.

16. Same as figure 15 for the reactions 620MeV ^{86}Kr + target. The smooth curves correspond to the value expected in the two limits for the average angular momentum in the reactions.

17. Same as figure 15 for the reactions 620MeV ^{86}Kr + target with only quasi-elastic events included.

18. Z-distributions at various laboratory angles in the reaction 620MeV ^{86}Kr + ^{197}Au.

19. Same as figure 18 for the reaction 288MeV ^{40}Ar + ^{197}Au.

20. Same as figure 19 for the reaction 979MeV ^{136}Xe + ^{197}Au.

21. Liquid drop potential energy of two touching spheres for N + Ag for various values of the angular momentum. The dashed curve displays the expected yield distribution for the $\ell = 50\hbar$ curve if the temperature of the complex is 3 MeV.

22. Angular distributions for the various Z's in the reactions 175MeV and 252MeV ^{20}Ne + ^{107}Ag.

23. Same as figure 22 for the reactions 288MeV and 340MeV ^{40}Ar + ^{197}Au.

24. Same as figure 22 for the reaction 620MeV ^{86}Kr + ^{197}Au.

25. Same as figure 22 for the reaction 979MeV ^{136}Xe + ^{197}Au.

26. Same as figure 22 for the reactions 288MeV and 340MeV ^{40}Ar + ^{107}Ag.

27. Definition of coordinates used in the dynamical model.

28. Time dependence of various quantities from the dynamical model. r_o is the strong absorption radius (interaction radius), ℓ_{in} is the incoming angular momentum value and E^* is the exit channel excitation energy. In this case, $E^*_{final} \approx 50$ MeV.

29. Interaction time as a function of $\eta \equiv \ell/\ell_{max}$ for damped and undamped nuclear motion.

30. Potential energies as a function of r/r_0 for various values of $\eta \equiv \ell/\ell_{max}$.

31. Average energy of nucleons above the internuclear barrier as a function of the internuclear separation for different temperatures.

32. Potential energies as a function of Z for various values of $\eta \equiv \ell/\ell_{max}$ in the reaction 252MeV ^{20}Ne + ^{107}Ag.

33. Same as figure 32 for the reaction 288MeV ^{40}Ar + ^{107}Ag.

34. Same as figure 32 for the reaction 288MeV ^{40}Ar + ^{197}Au.

35. Same as figure 32 for the reaction 620MeV ^{86}Kr + ^{197}Au.

36. Same as figure 32 for the reaction 979MeV ^{136}Xe + ^{197}Au.

37. (a-c) Contours of constant probability as calculated from the master-equation using the potential energy curves in figure 32.

38. Same as figure 37 using the potential curves from figure 33.

39. Same as figure 37 using the potential curves from figure 34.

40. Same as figure 37 using the potential curves from figure 35.

41. Same as figure 37 using the potential curves from figure 36.

42. (a) Expected shape of curves corresponding to constant angular momentum if no angular momentum is transferred from orbital angular momentum into spin of the nuclei in the Z-TKE plane.

    (b) Same quantity as in (a) assuming rigid rotation of the complex.

    (c) Realistic expectations (dots) of quantity displayed in (a) and (b).

43. Display that indicates that all possible initial assumptions of the sharing of angular momentum between orbital and spin angular momenta converge to the same limit.

44. Values of $\frac{\ell_{rel}}{\ell_{in}}$ as a function of Z at various stages of the iteration.

45. Same quantity displayed in figure 42 as calculated by the model. The estimated realistic shape of figure 42c is shown to be correct.

46. Plots of $d\sigma/dZ$ as a function of Z for various projectiles + ^{197}Au.

47. Potential energy vs. Z for the average angular momentum for the three projectiles + ^{197}Au reactions displayed in figure 46.

48. Same as figure 46 for ^{86}Kr + various targets.

49. Same as figure 46 for ^{86}Kr + ^{197}Au at various energies.

50. Plots of $\partial^2\sigma/\partial\Omega\partial Z$ as a function of θ for various Z's in the reaction ^{86}Kr + ^{197}Au at 506MeV.

51. Same as figure 50 at 620MeV.

52. Same as figure 50 at 731MeV.

53. Plot of M_γ vs. Z for the quasi-elastic component in the reaction 620MeV ^{86}Kr + ^{197}Au.

54. Same as figure 53 for comparable experimental and calculated angular settings.

55. Same as figure 53 for various Z's as a function of angle.

56. Expected form of the density distribution and the single-particle potential in the interaction region as two nuclei collide.

57. The probability distribution $\Pi(t)$ for the nuclear case.

58. Variance of $\Pi(t)$ vs. log(τ) [τ is the centroid of $\Pi(t)$] for various assumptions about the relative strength of the nuclear damping vs. the inter-nuclear potential energy.

59. Modifications to standard proximity potential form factor due to finite extent of interacting, identical, spherical nuclei for various values of the effective radius, C. The curve labeled ∞ corresponds to the unmodified values.

60. Coordinate system used in Appendix D.

61. Same as figure 59 for unequal spherical nuclei for various assumptions about the two effective radii. Again, ∞ labels the unmodified values.

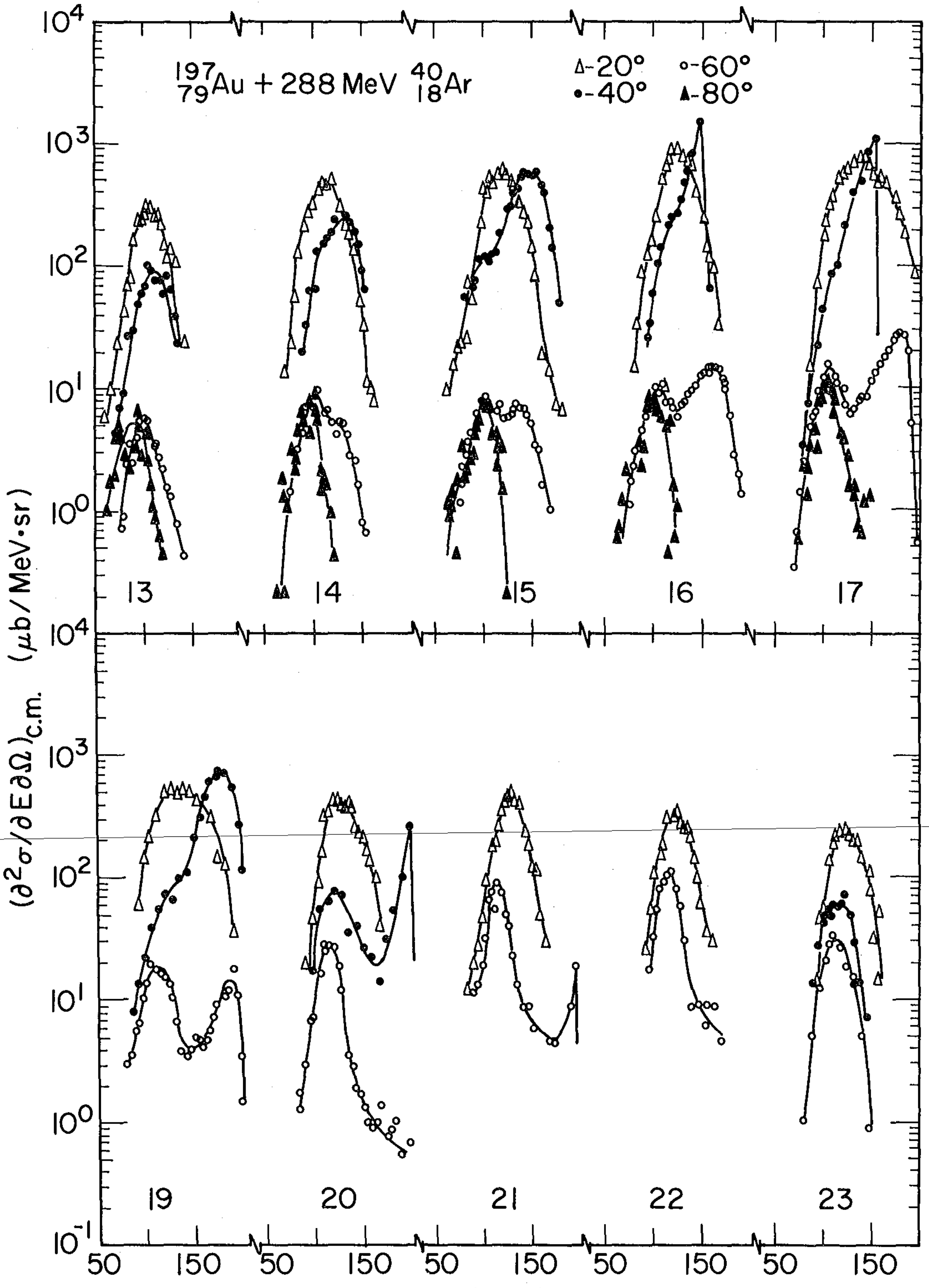

XBL759-4574

Fig. 1

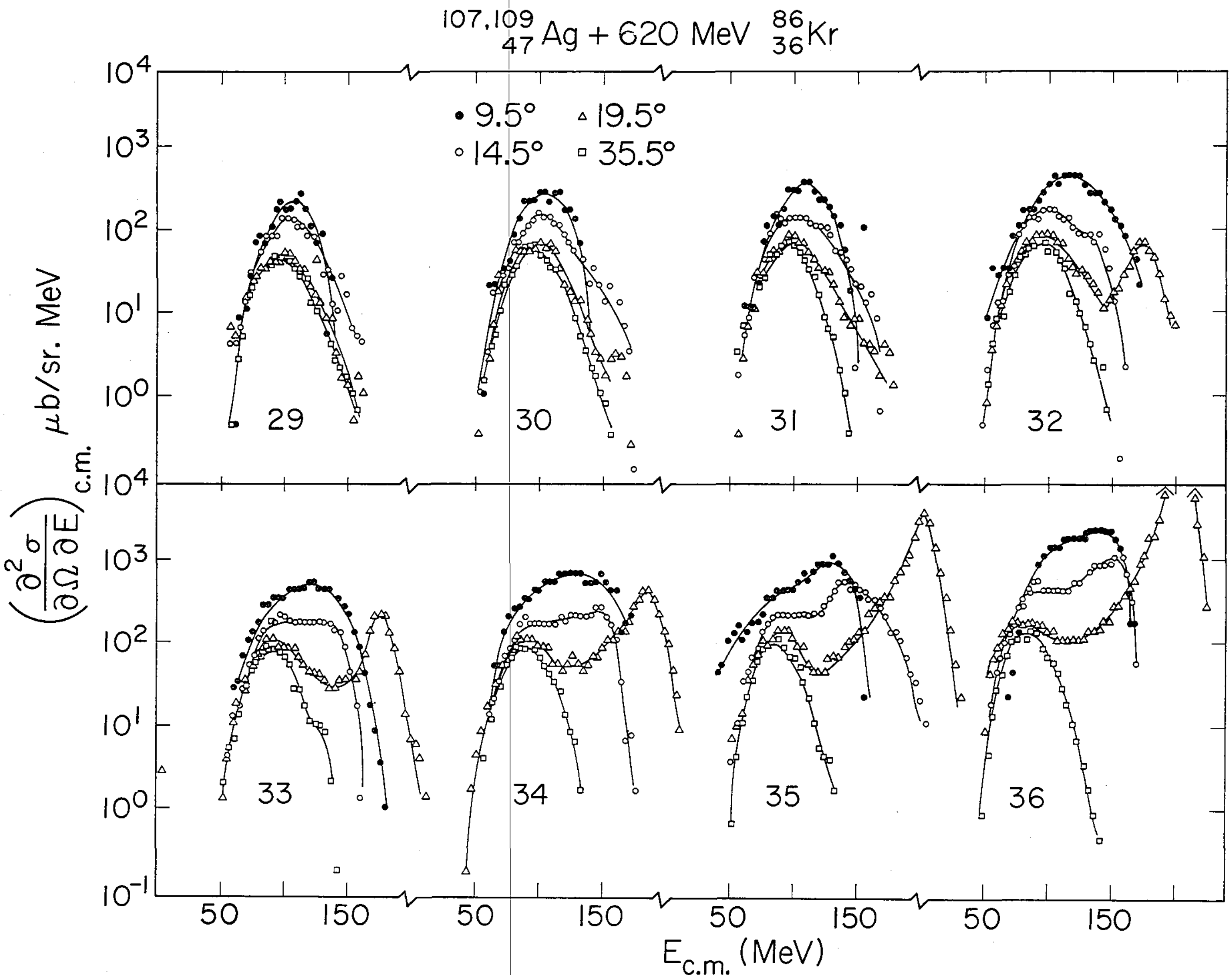

Fig. 2

XBL 766-3004

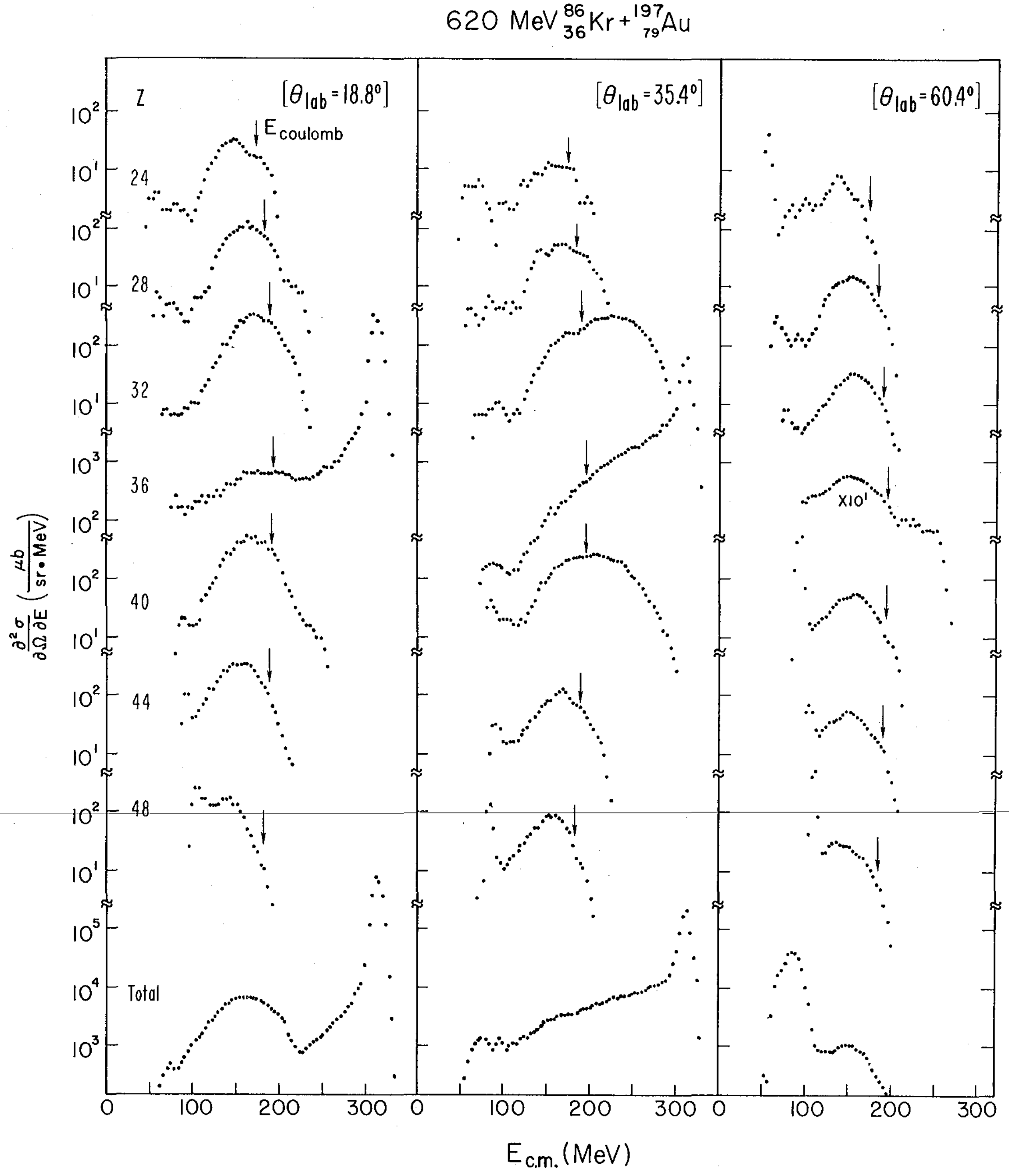

XBL 7610-4211

Fig. 3

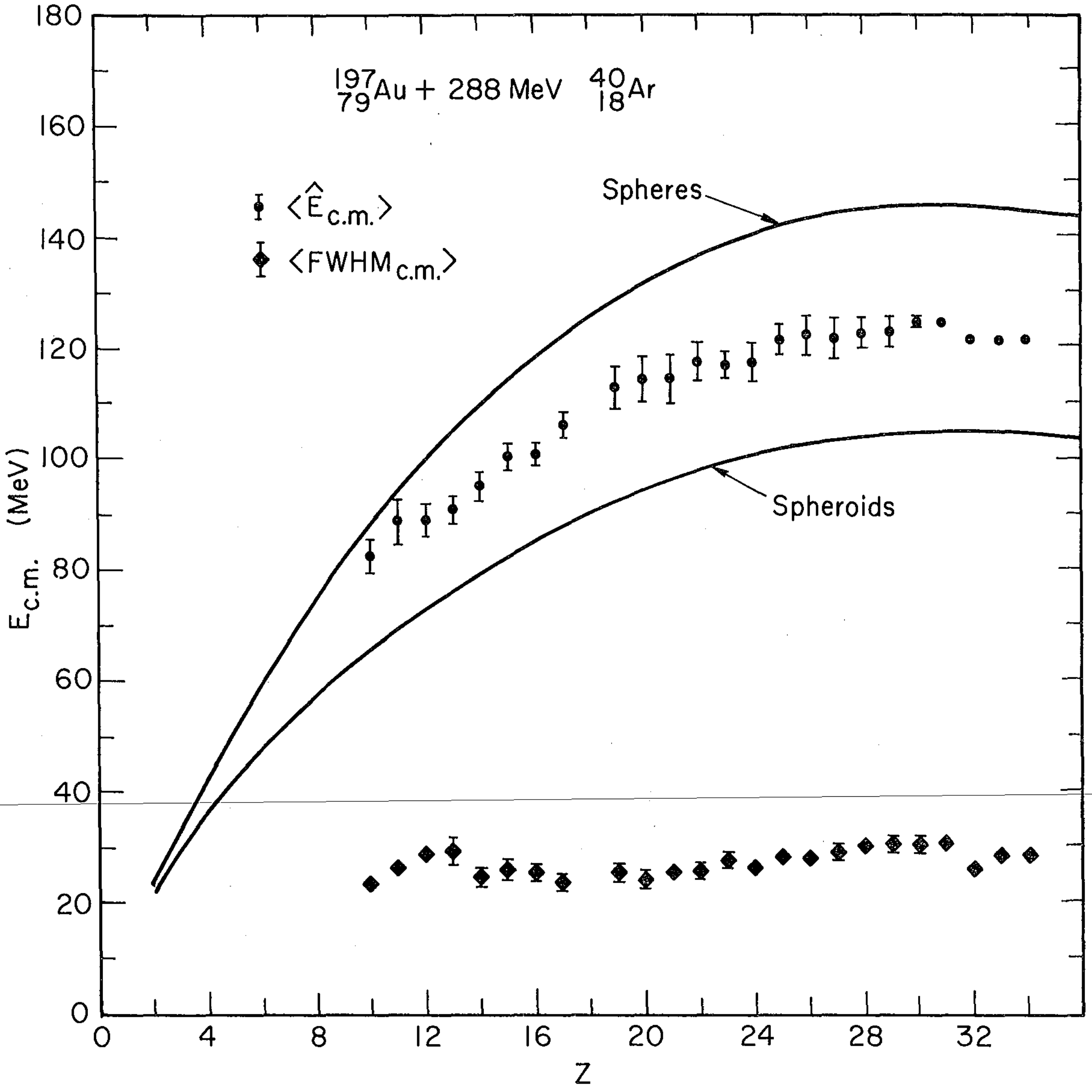

XBL759-4575

Fig. 4

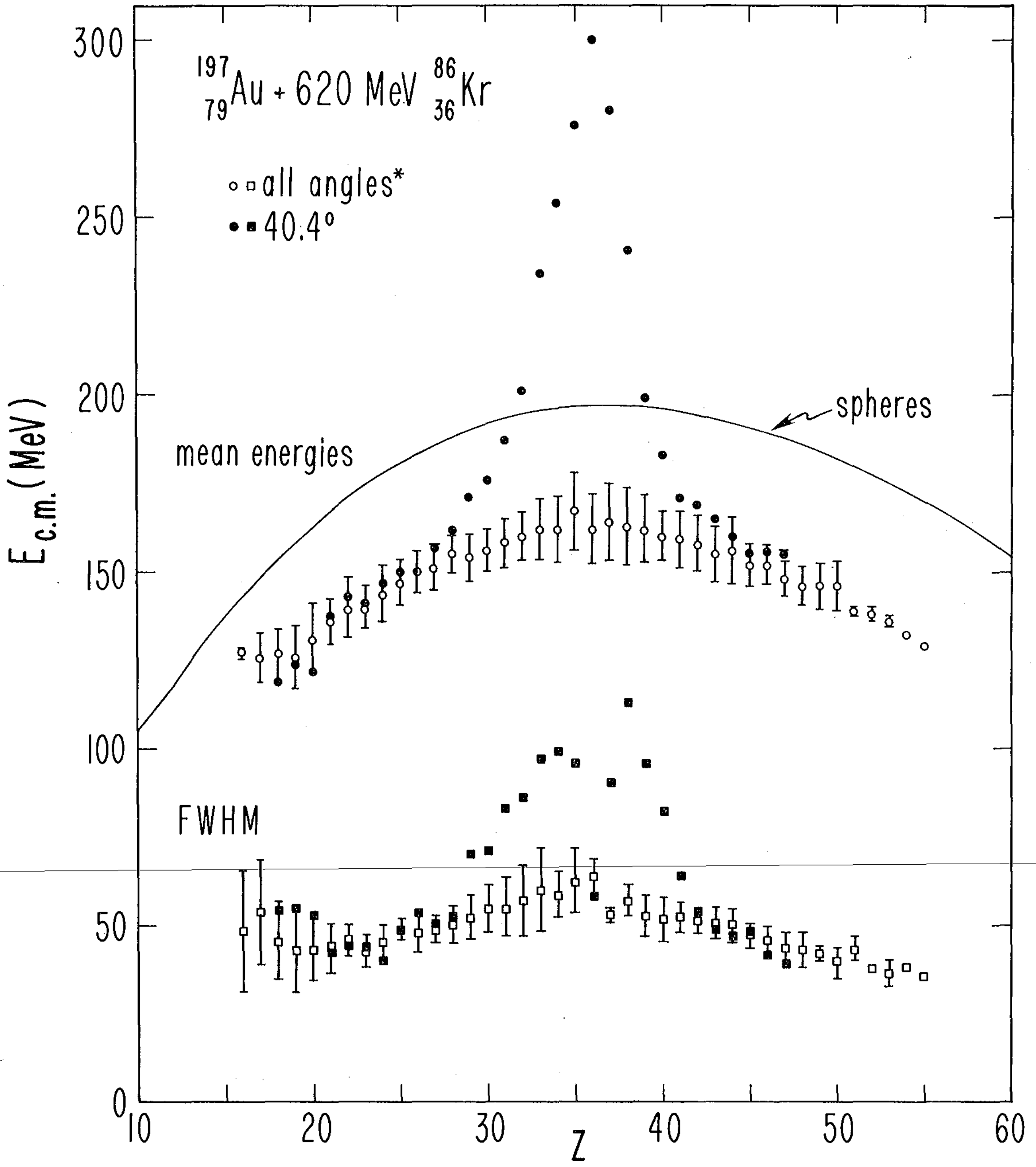

XBL 7611-4477

Fig. 5

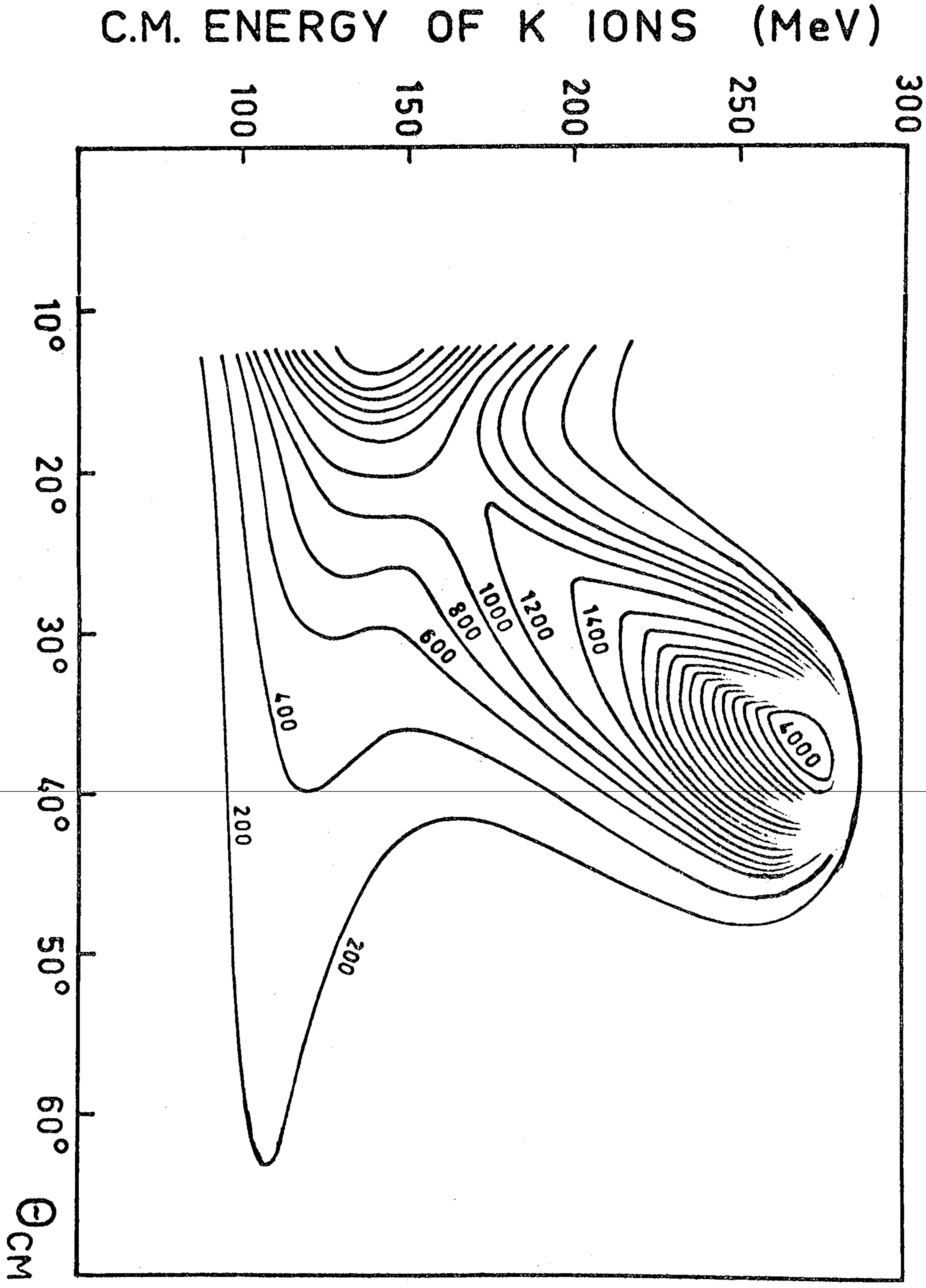

XBL 746-963

Fig. 6

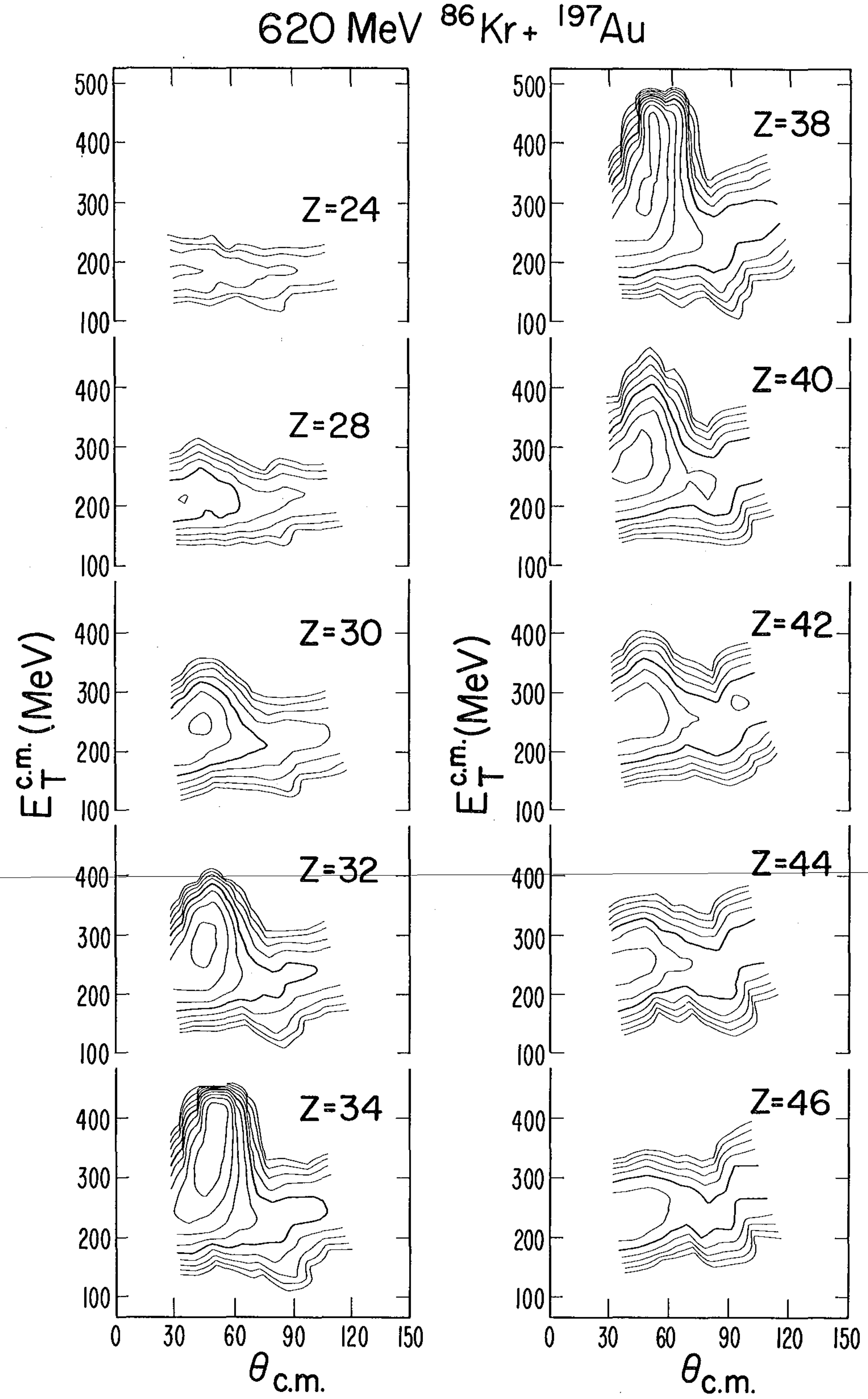

XBL 769 4077

Fig. 7

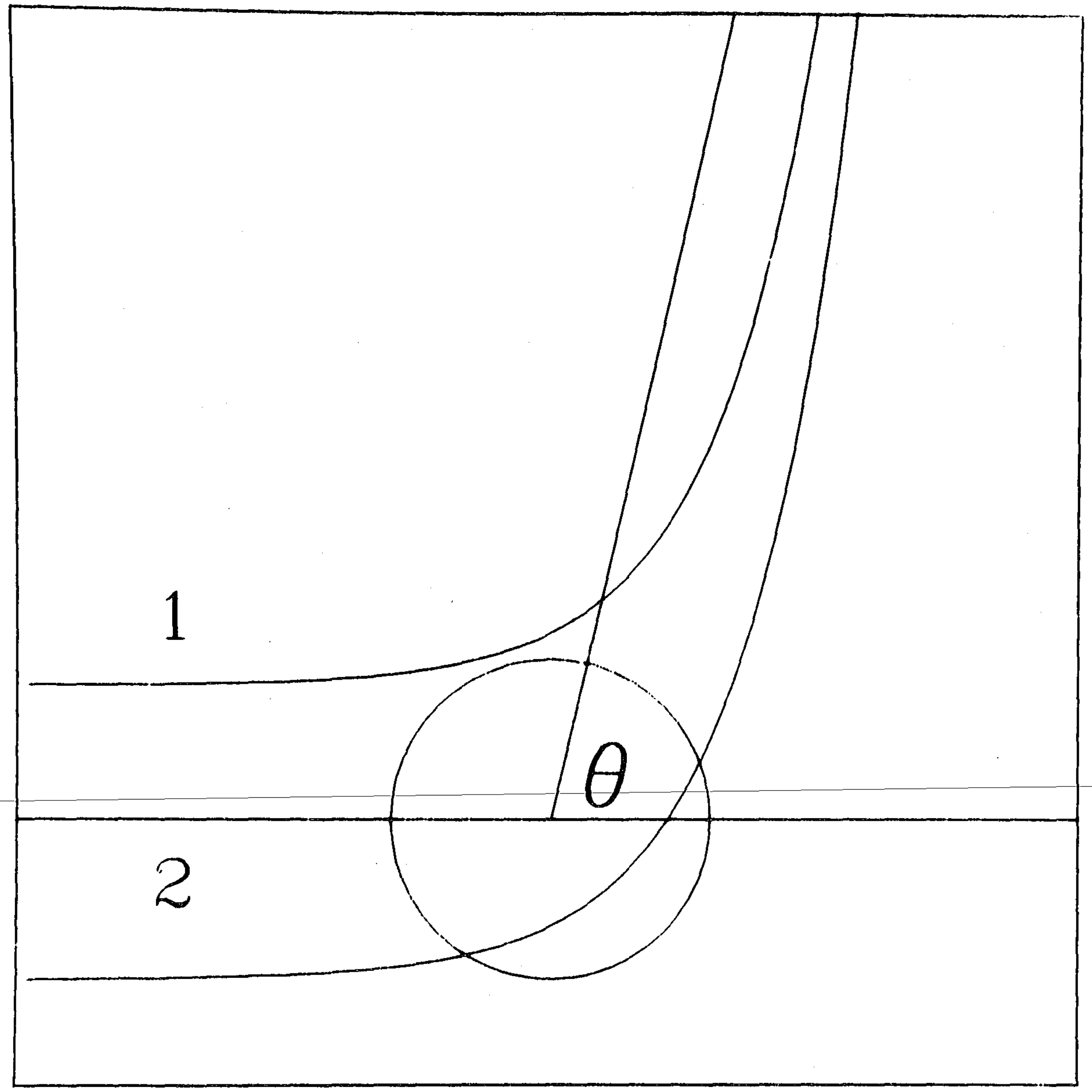

XBL7910-12521

Fig. 8

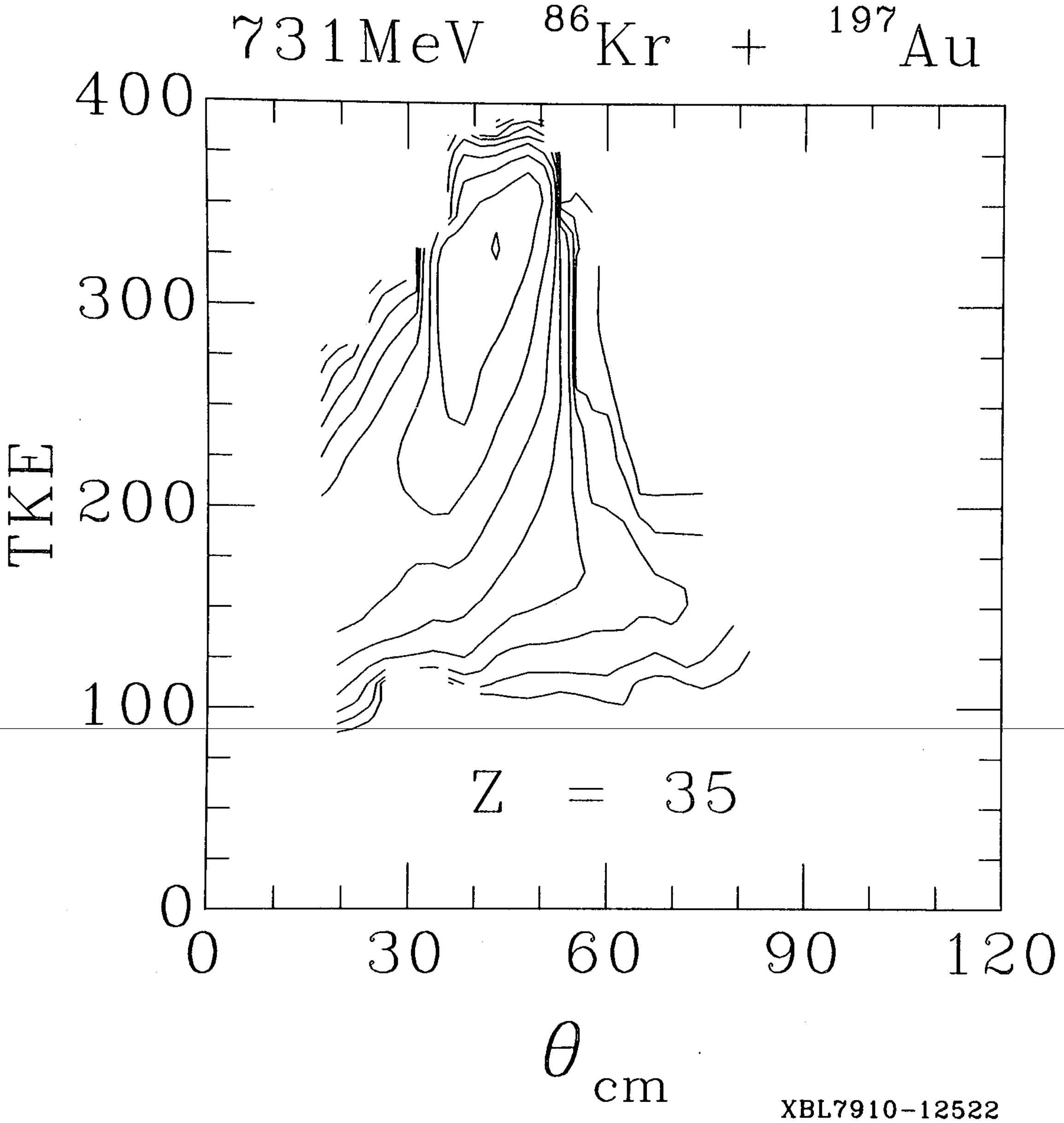

XBL7910-12522

Fig. 9

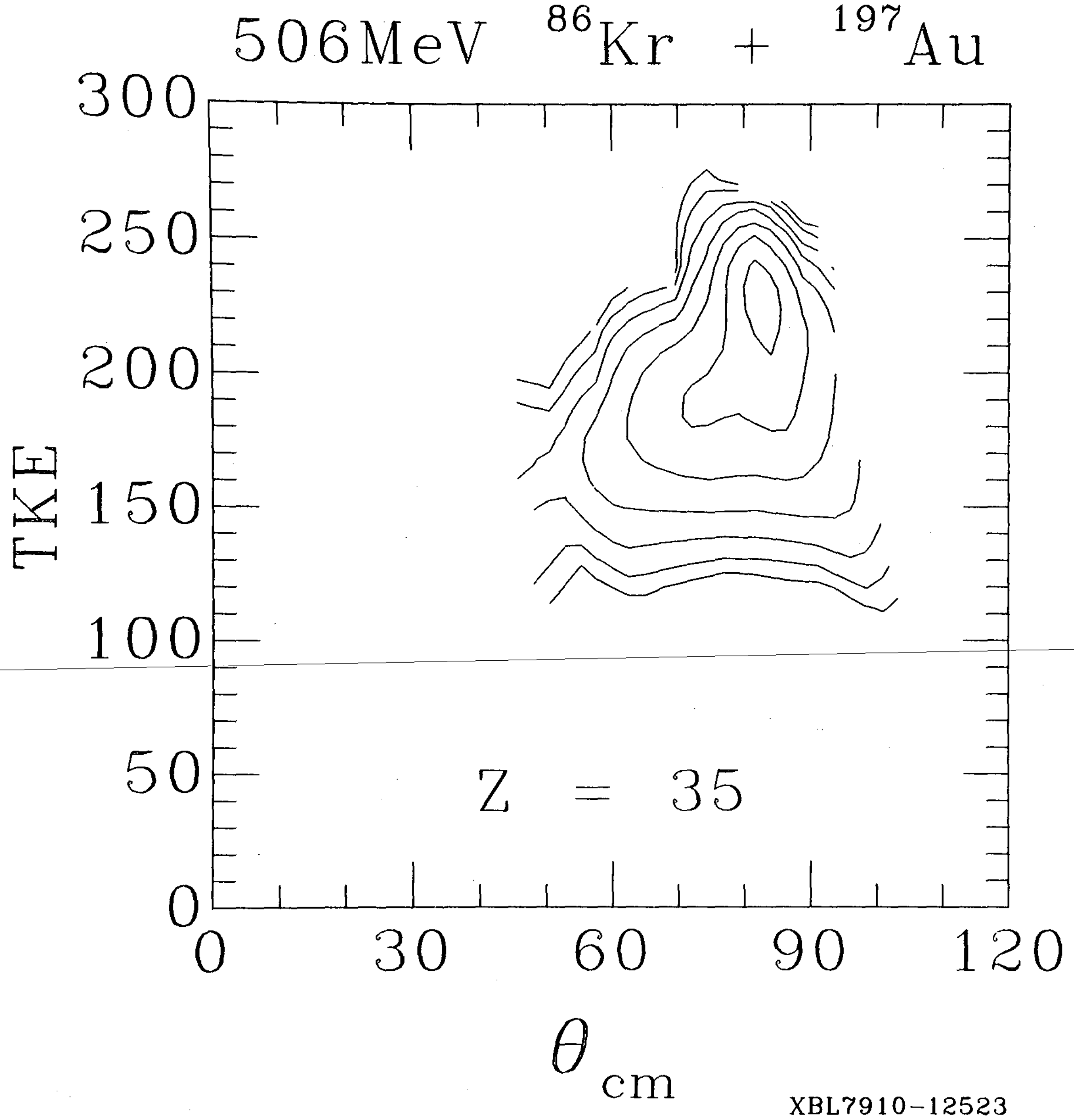
506MeV ^{86}Kr + ^{197}Au
TKE
0
50
100
150
200
250
300
θ_{cm}
0
30
60
90
120
Z = 35
XBL7910-12523

Fig. 10

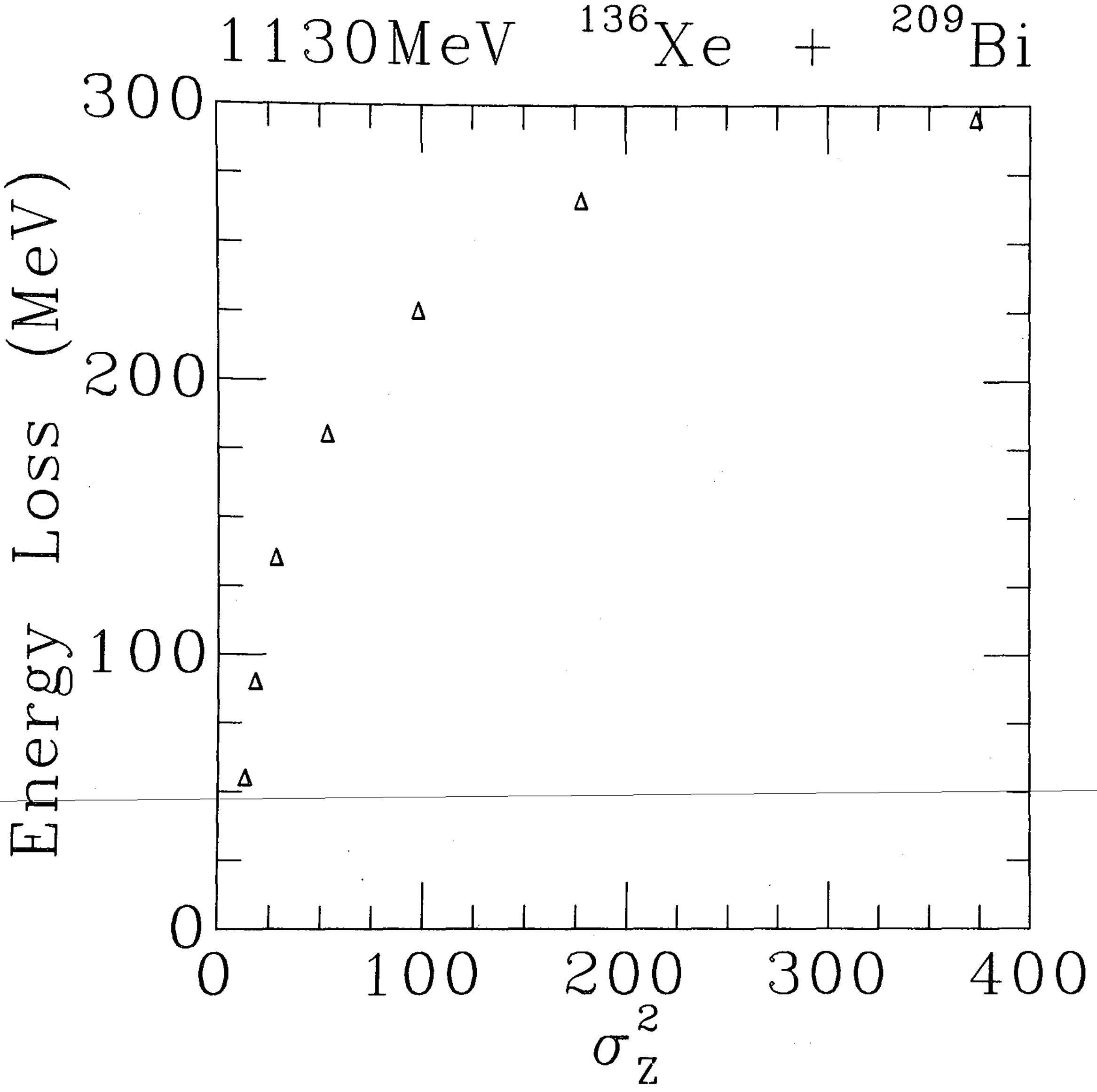

XBL7910-12524

Fig. 11

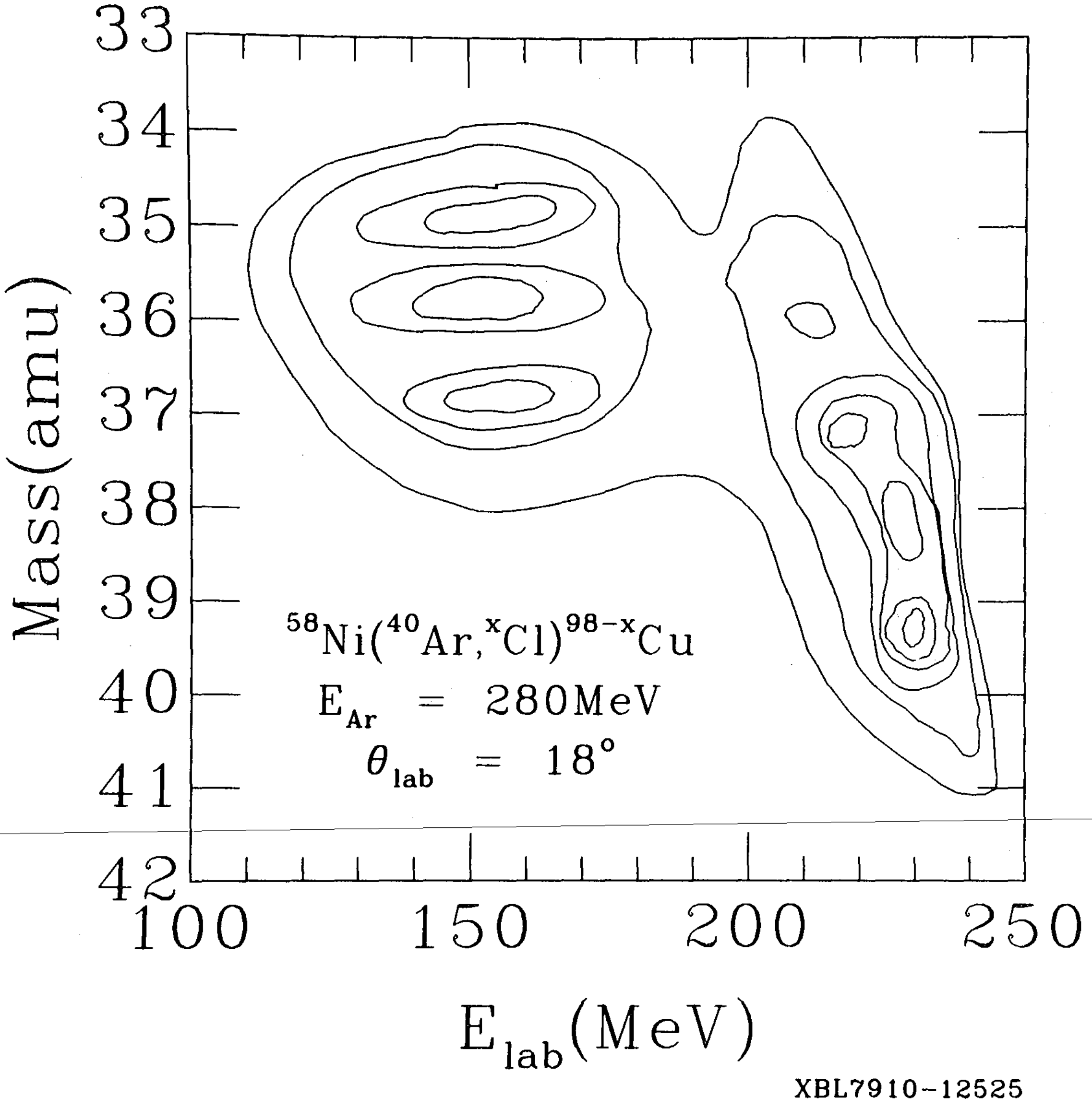

Mass(amu)
33
34
35
36
37
38
39
40
41
42
100
150
200
250
E_{lab}(MeV)
$^{58}Ni(^{40}Ar,^{x}Cl)^{98-x}Cu$
E_{Ar} = 280MeV
θ_{lab} = 18°
XBL7910-12525

Fig. 12

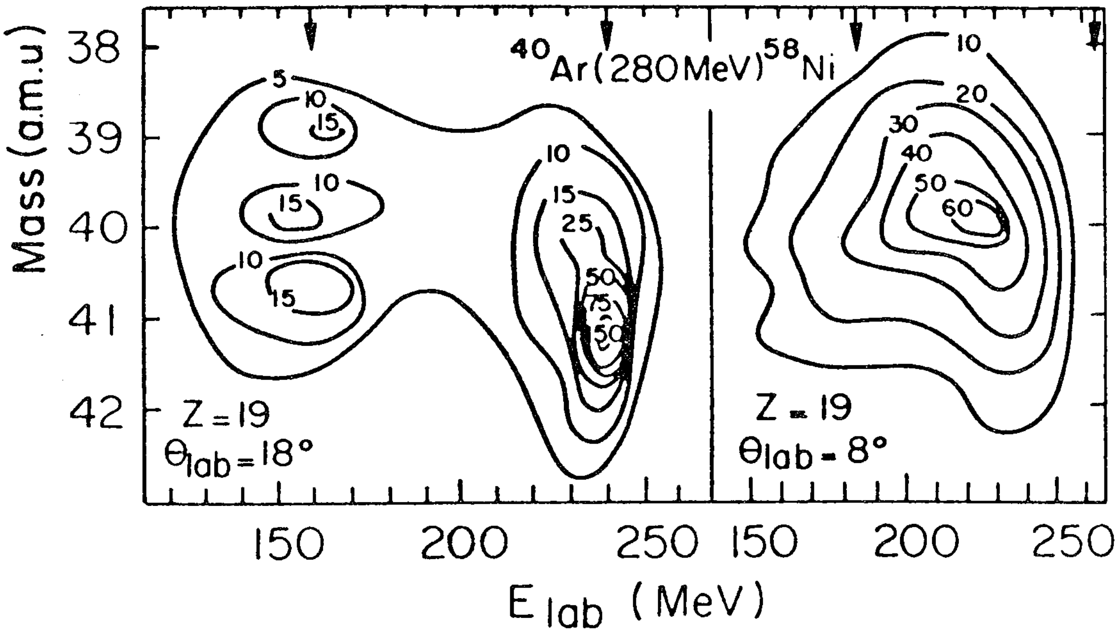

XBL 788-9931

Fig. 13

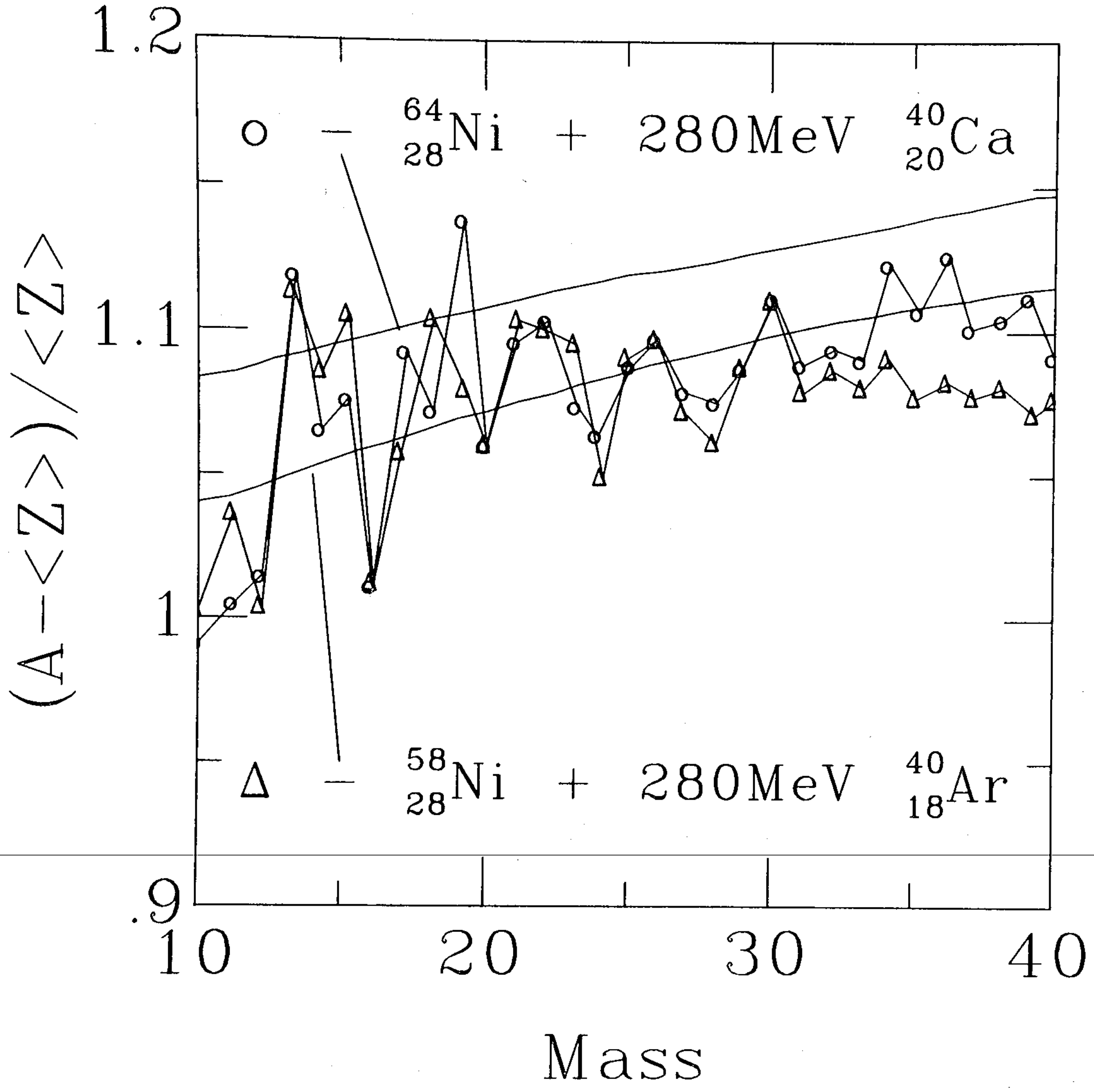

XBL7910-12526

Fig. 14a

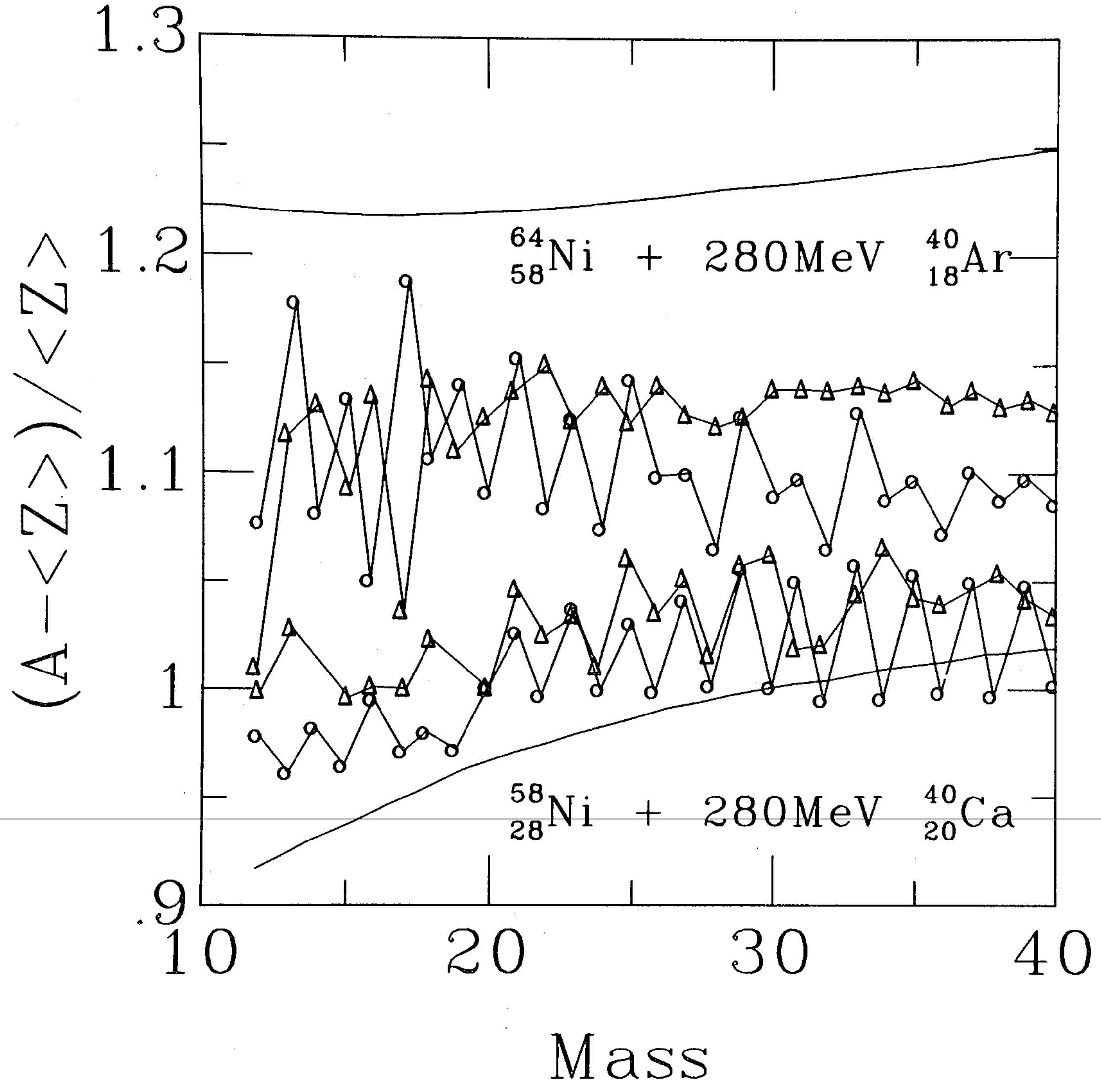

XBL7910-12527

Fig. 14b

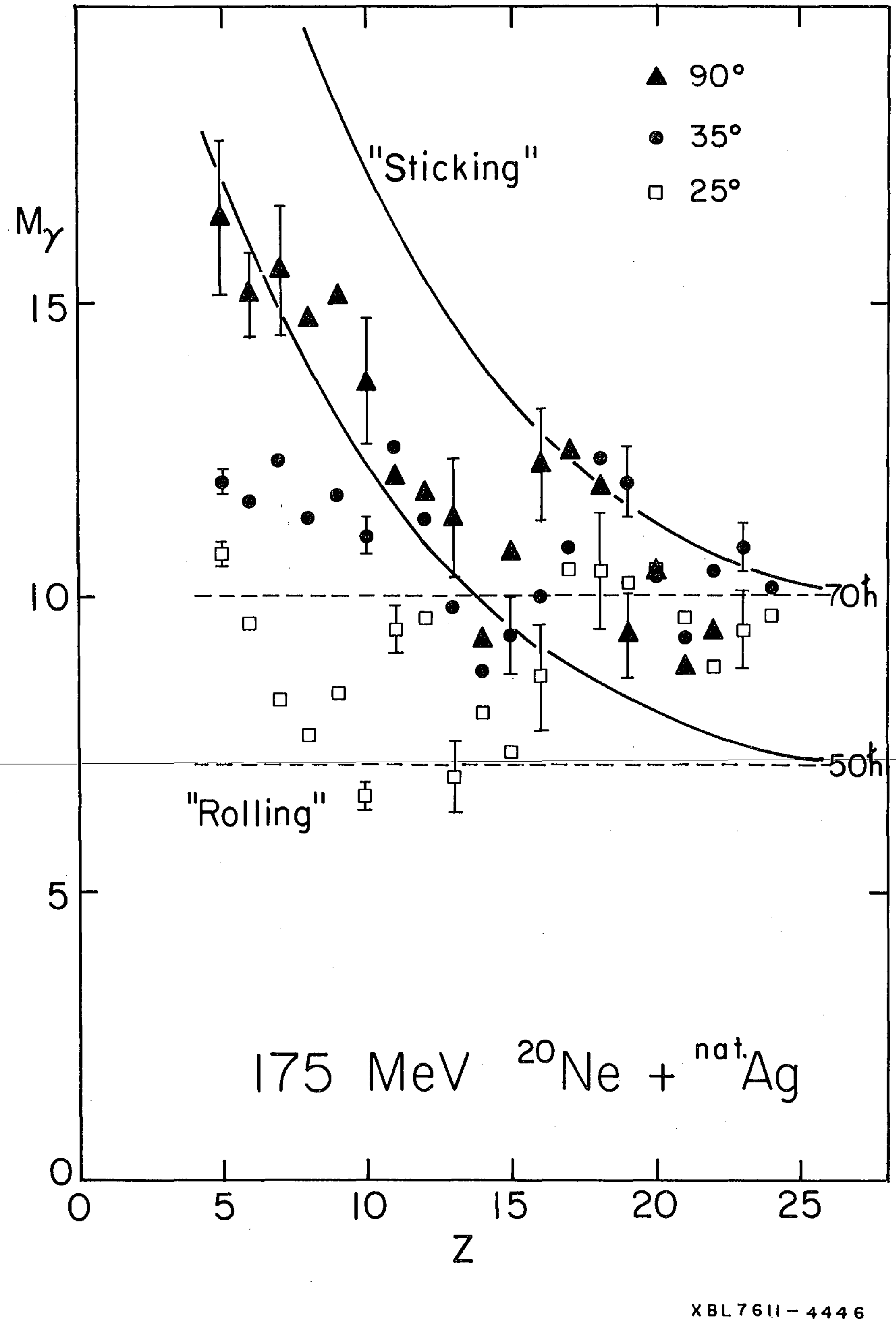
▲ 90°
● 35°
□ 25°
"Sticking"
"Rolling"
M_γ
70ħ
50ħ
175 MeV ^{20}Ne + $^{nat.}$Ag
0
5
10
15
20
25
Z
XBL7611-4446

Fig. 15

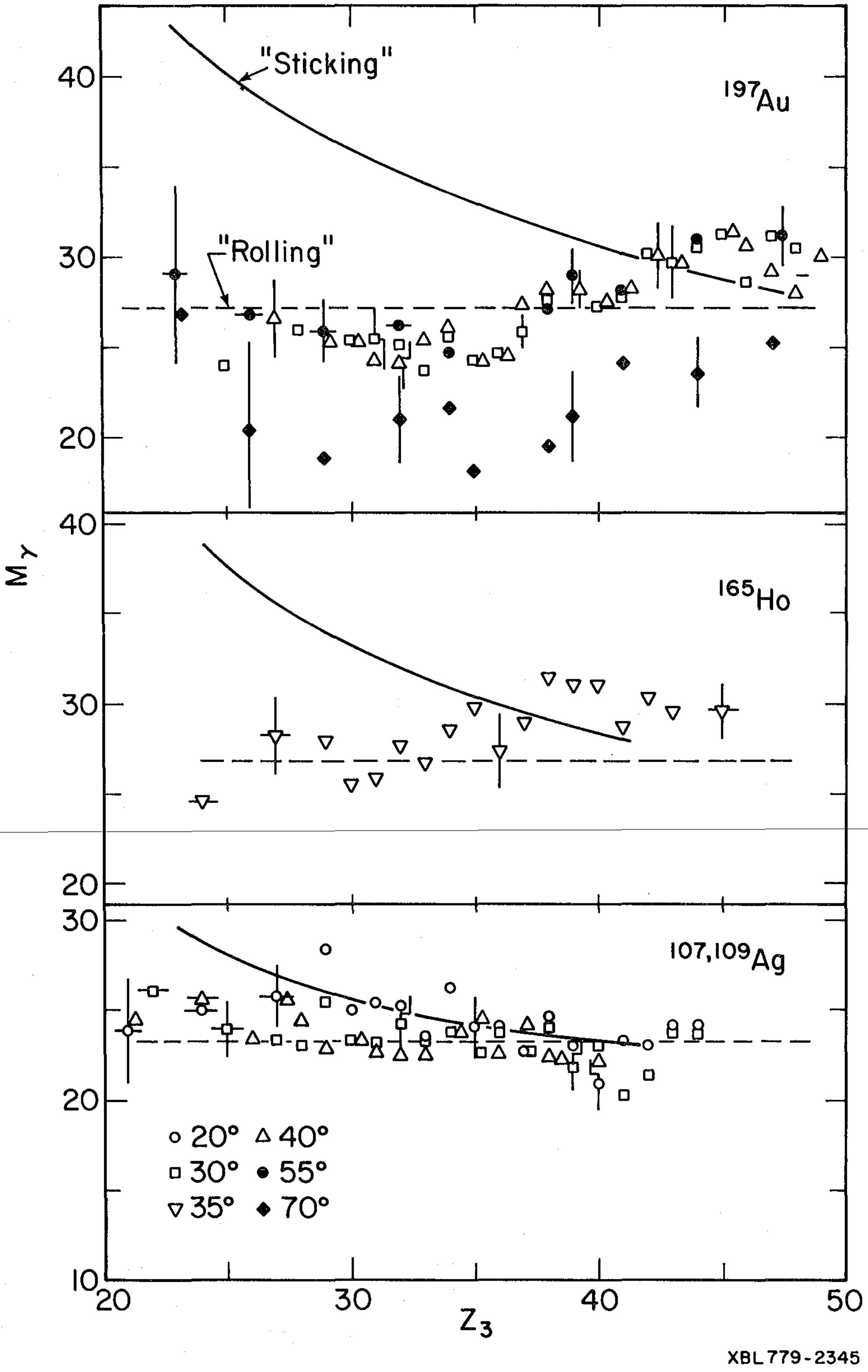
"Sticking"
"Rolling"
197Au
165Ho
107,109Ag
M_γ
Z_3
40
30
20
40
30
20
30
20
10
20
30
40
50
○ 20° △ 40°
□ 30° ● 55°
▽ 35° ◆ 70°
XBL 779-2345

Fig. 16

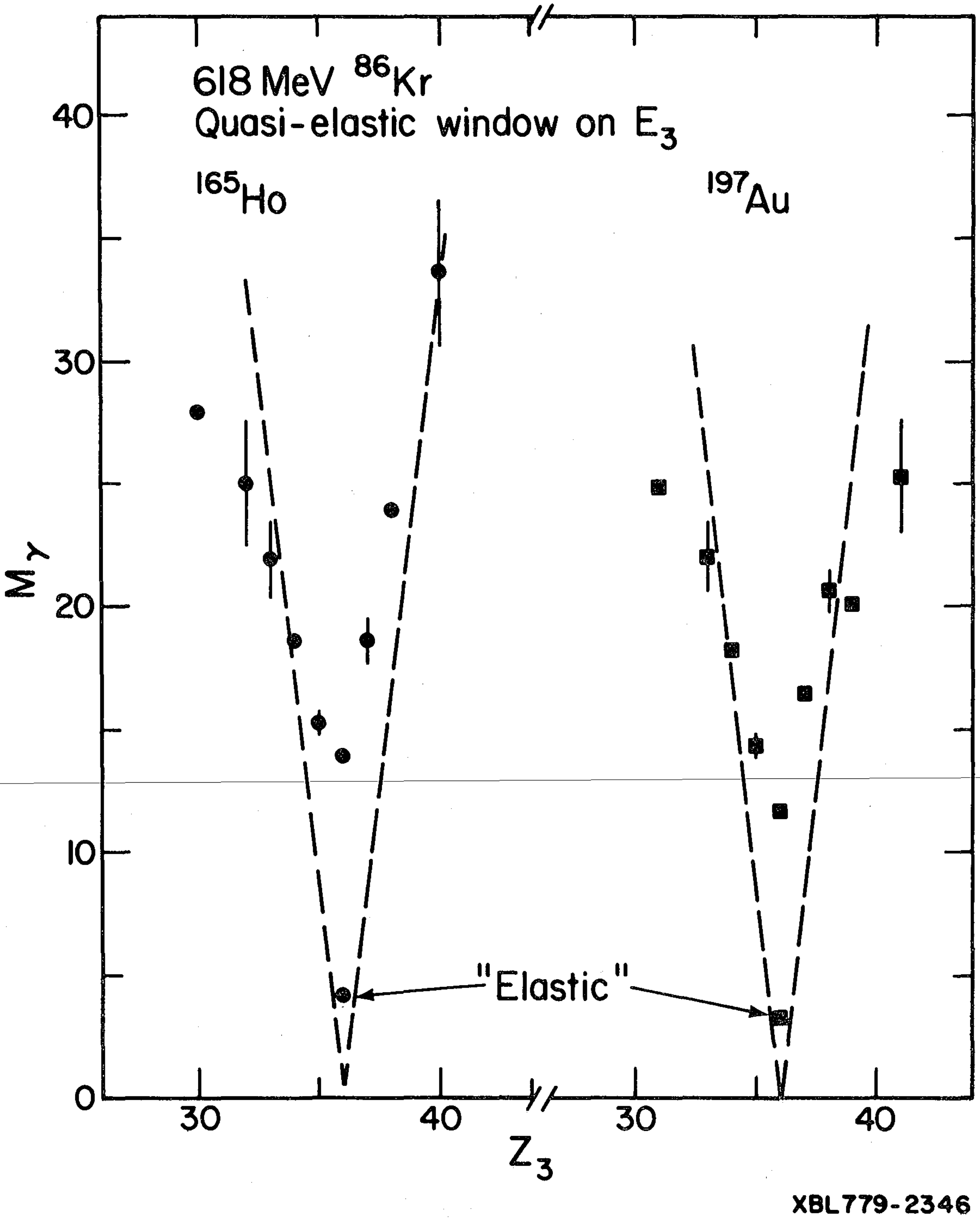
618 MeV ^{86}Kr
Quasi-elastic window on E_3
^{165}Ho
^{197}Au
"Elastic"
M_γ
Z_3
0
10
20
30
40
30
40
30
40
XBL779-2346

Fig. 17

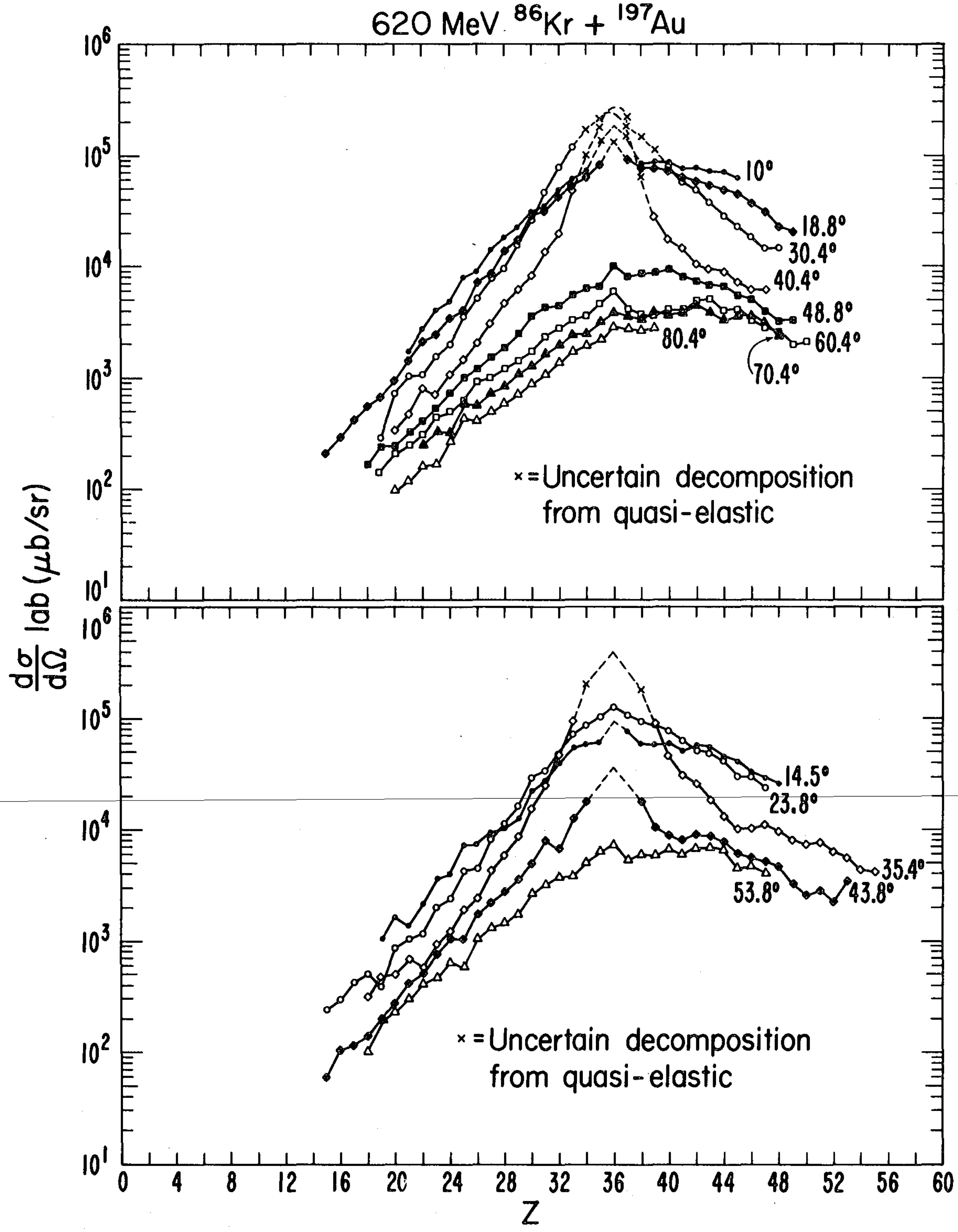

XBL761-2088

Fig. 18

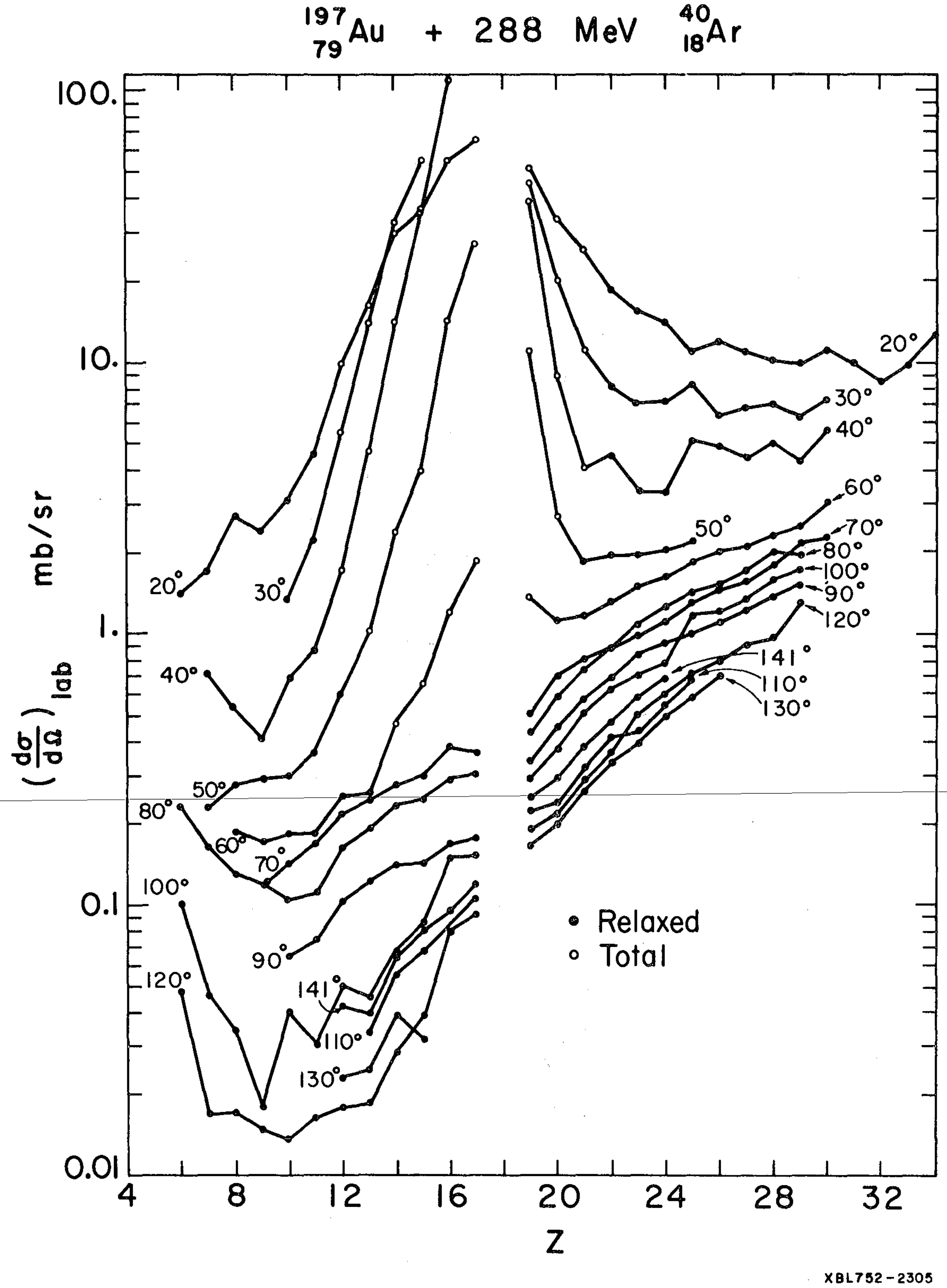
$^{197}_{79}$Au + 288 MeV $^{40}_{18}$Ar
$\left(\frac{d\sigma}{d\Omega}\right)_{lab}$ mb/sr
Z
100.
10.
1.
0.1
0.01
4
8
12
16
20
24
28
32
20°
30°
40°
50°
60°
70°
80°
90°
100°
110°
120°
130°
141°
● Relaxed
○ Total
XBL752-2305

Fig. 19

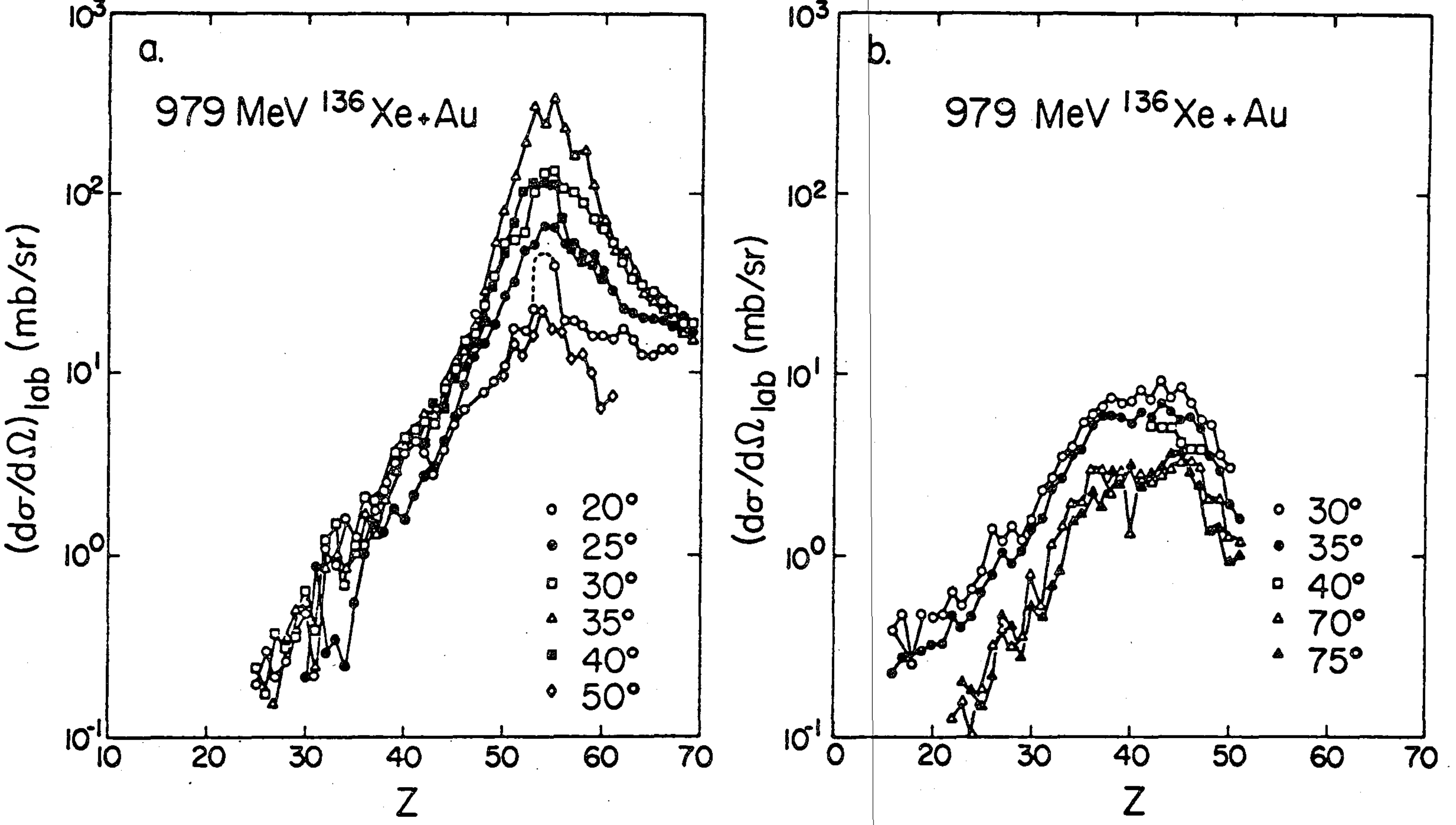

XBL 767 3171

Fig. 20

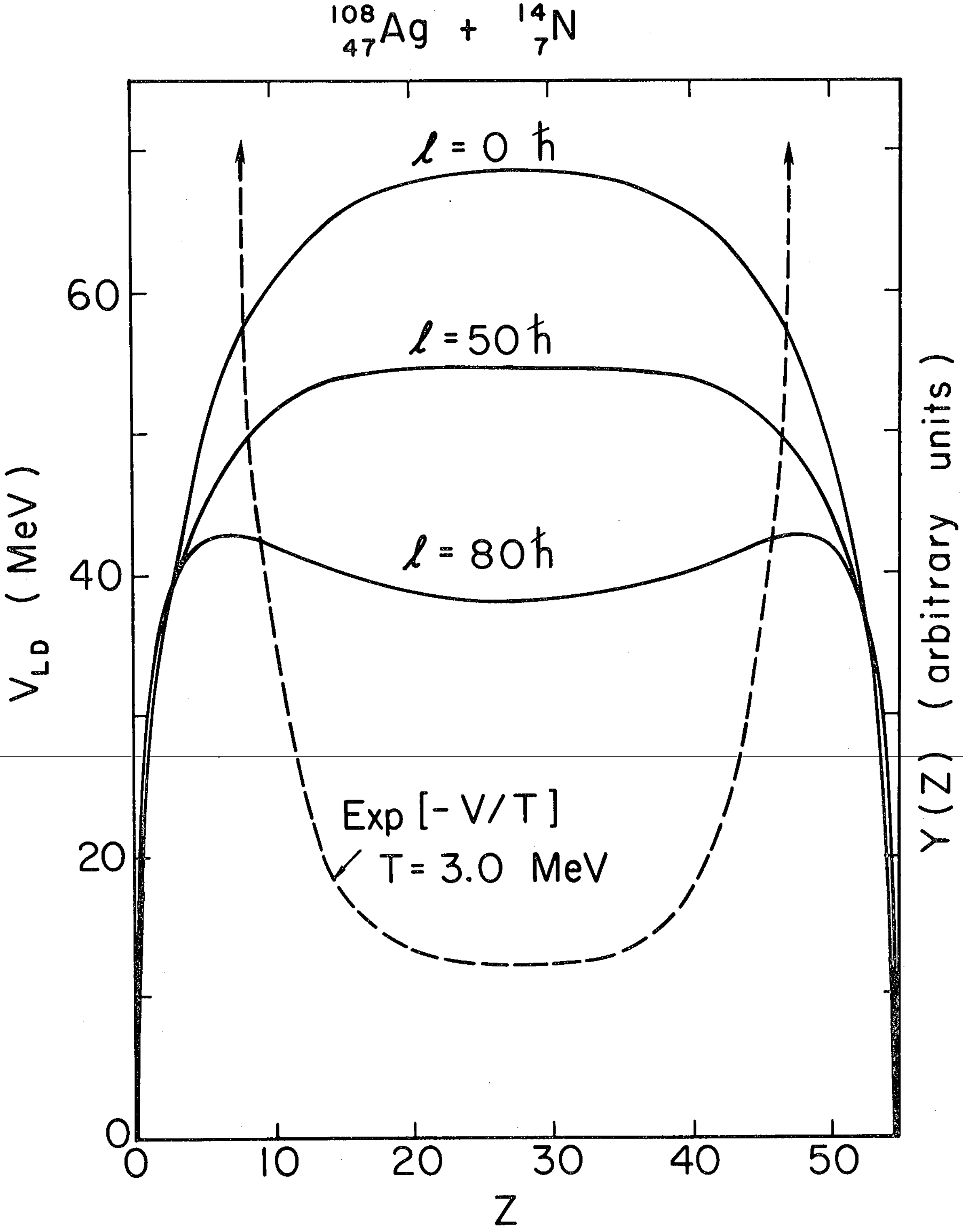

XBL759-3863

Fig. 21

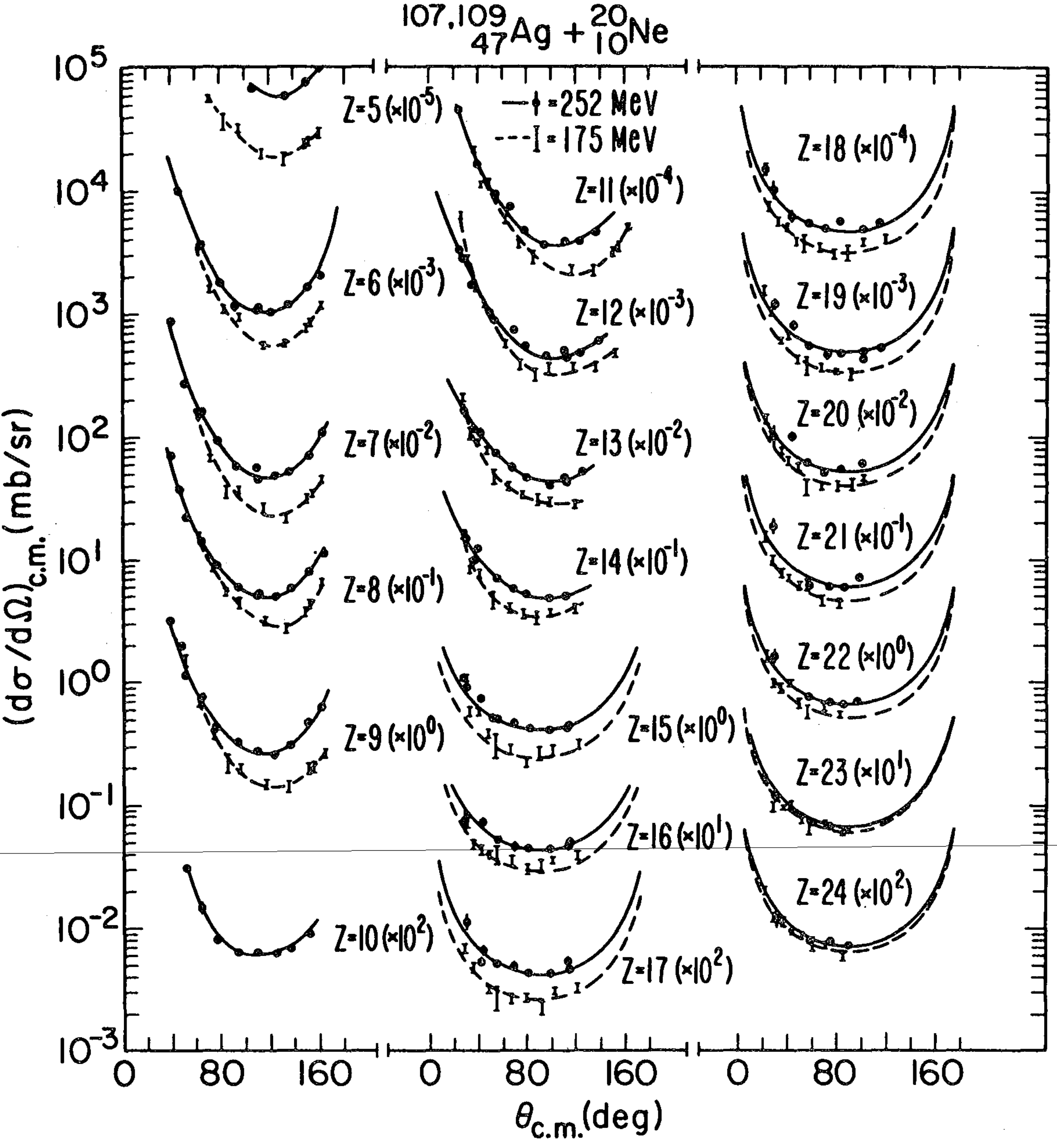
$^{107,109}_{47}Ag + ^{20}_{10}Ne$
—ϕ = 252 MeV
---I = 175 MeV
Z=5 (×10^{-5})
Z=6 (×10^{-3})
Z=7 (×10^{-2})
Z=8 (×10^{-1})
Z=9 (×10^{0})
Z=10 (×10^{2})
Z=11 (×10^{-4})
Z=12 (×10^{-3})
Z=13 (×10^{-2})
Z=14 (×10^{-1})
Z=15 (×10^{0})
Z=16 (×10^{1})
Z=17 (×10^{2})
Z=18 (×10^{-4})
Z=19 (×10^{-3})
Z=20 (×10^{-2})
Z=21 (×10^{-1})
Z=22 (×10^{0})
Z=23 (×10^{1})
Z=24 (×10^{2})
$(d\sigma/d\Omega)_{c.m.}$ (mb/sr)
10^5
10^4
10^3
10^2
10^1
10^0
10^{-1}
10^{-2}
10^{-3}
0
80
160
0
80
160
0
80
160
$\theta_{c.m.}$(deg)
XBL 757-3612

Fig. 22

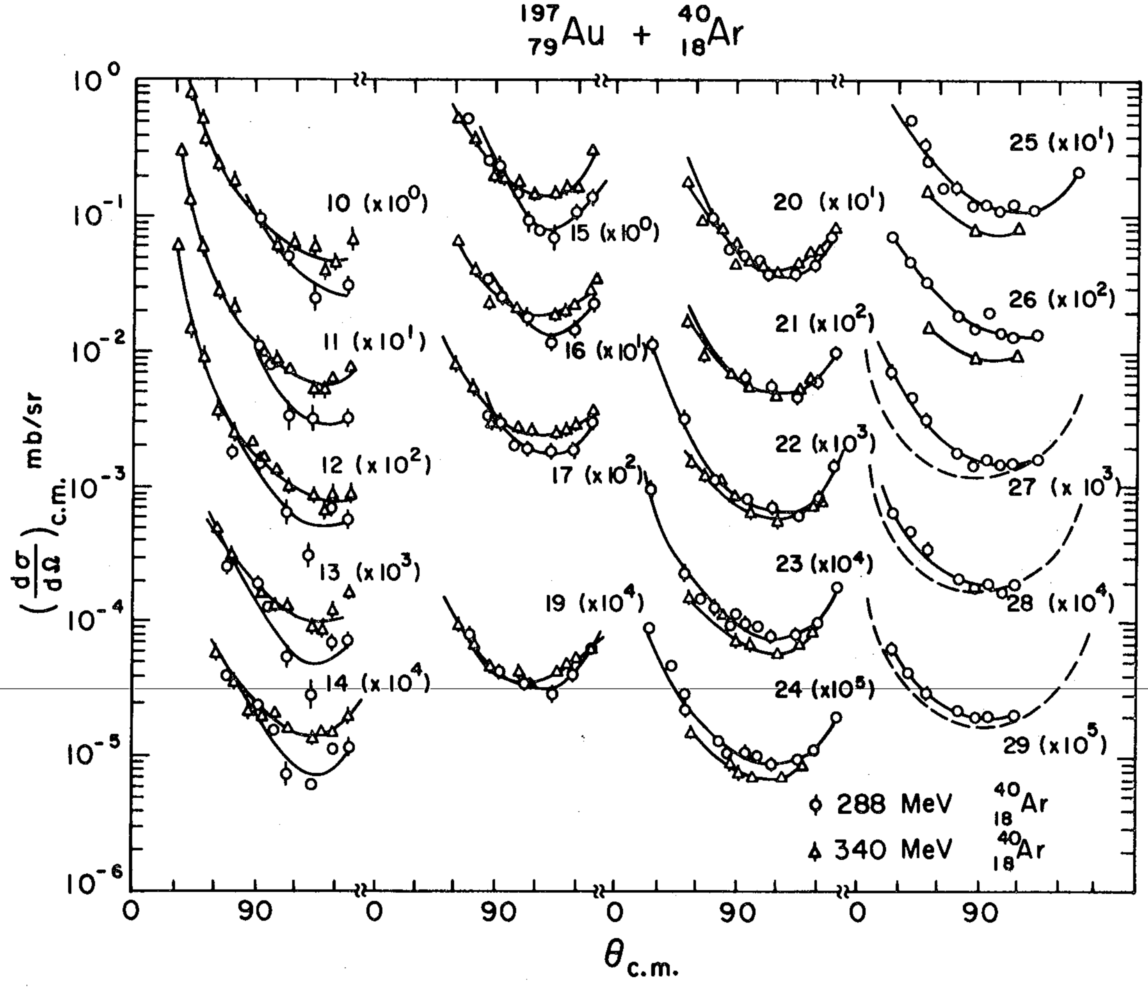

XBL 752-2307 A

Fig. 23

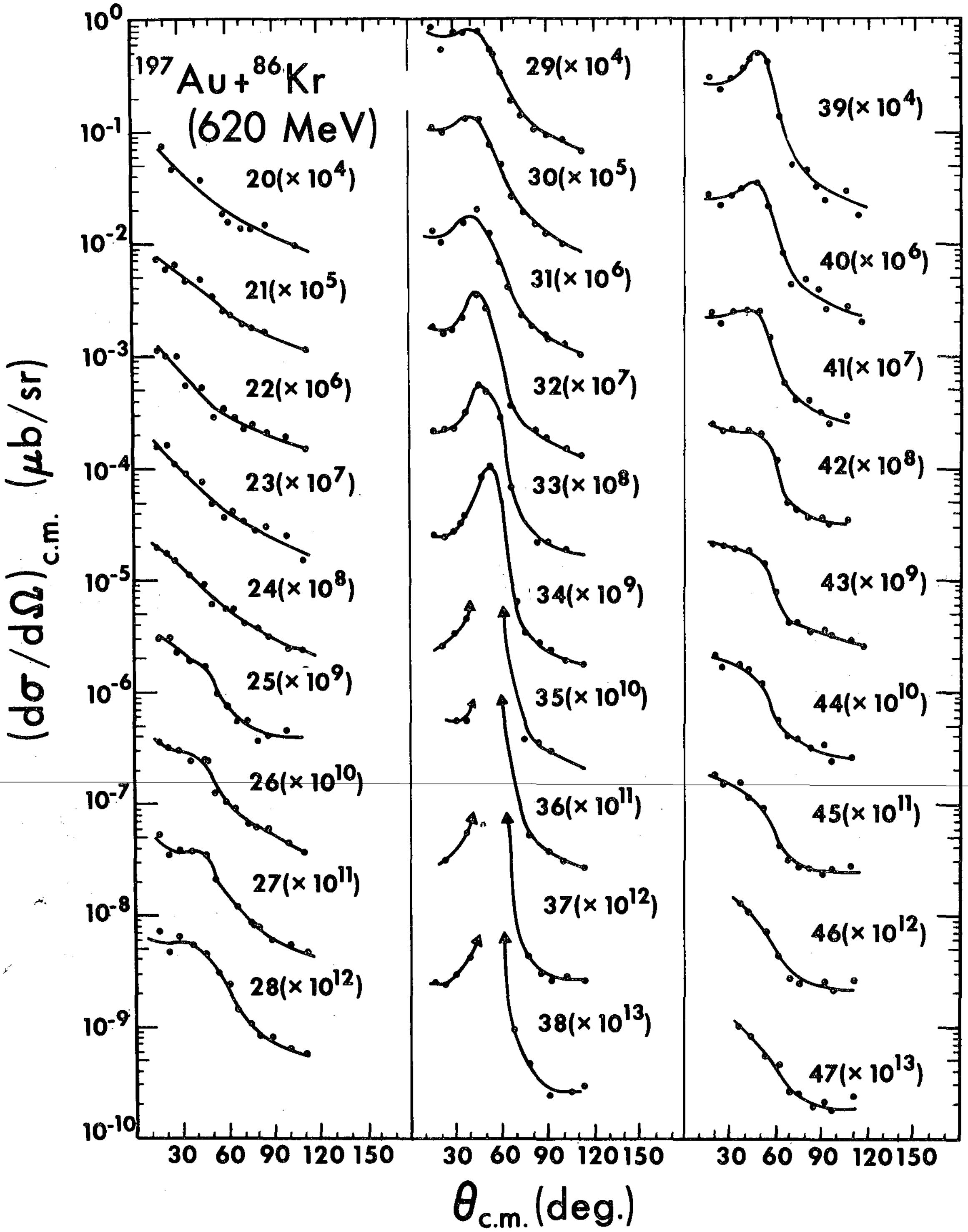

XBL 7512-9891

Fig. 24

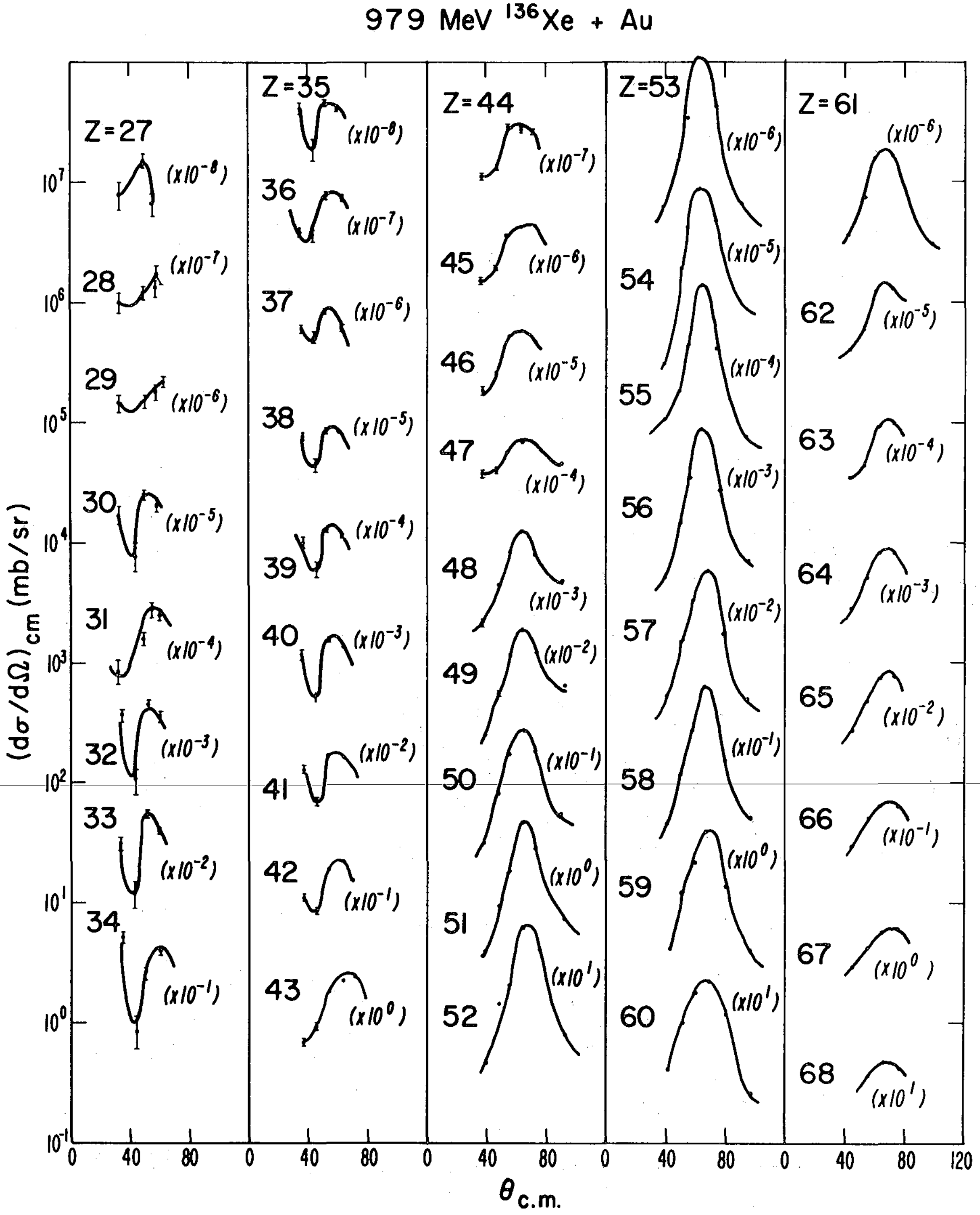

XBL 766-3007

Fig. 25

Fig. 26

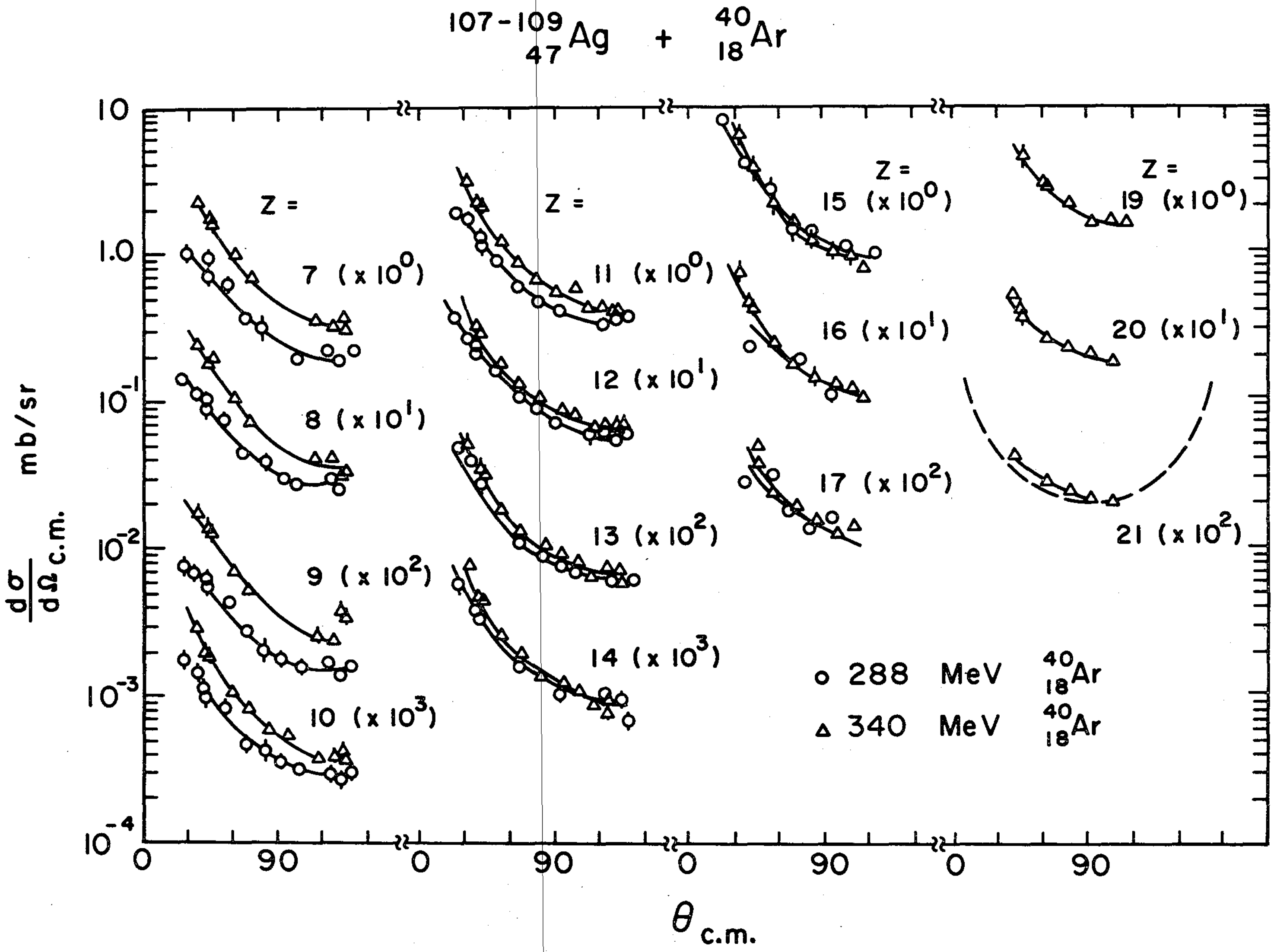

XBL752-2302

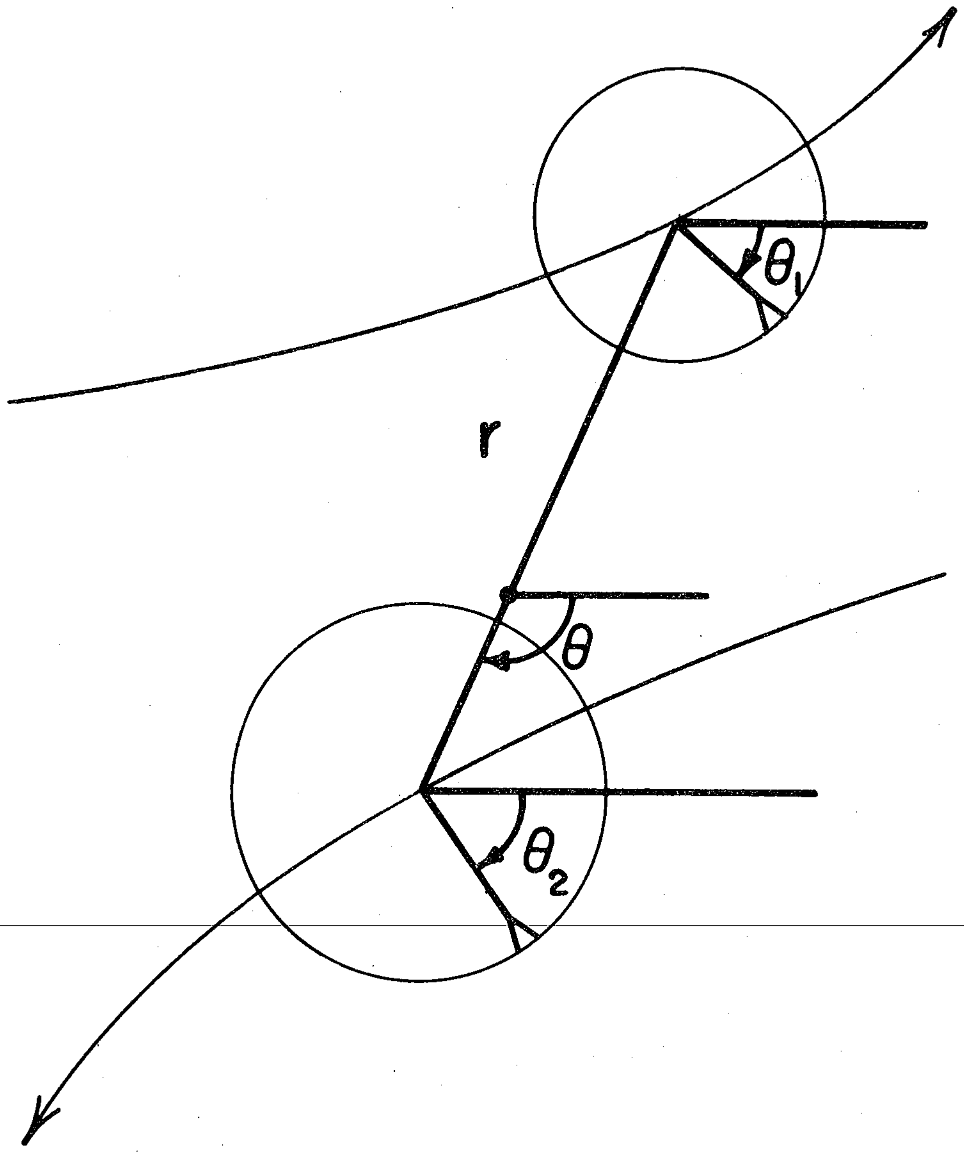

XBL745-3266

Fig. 27

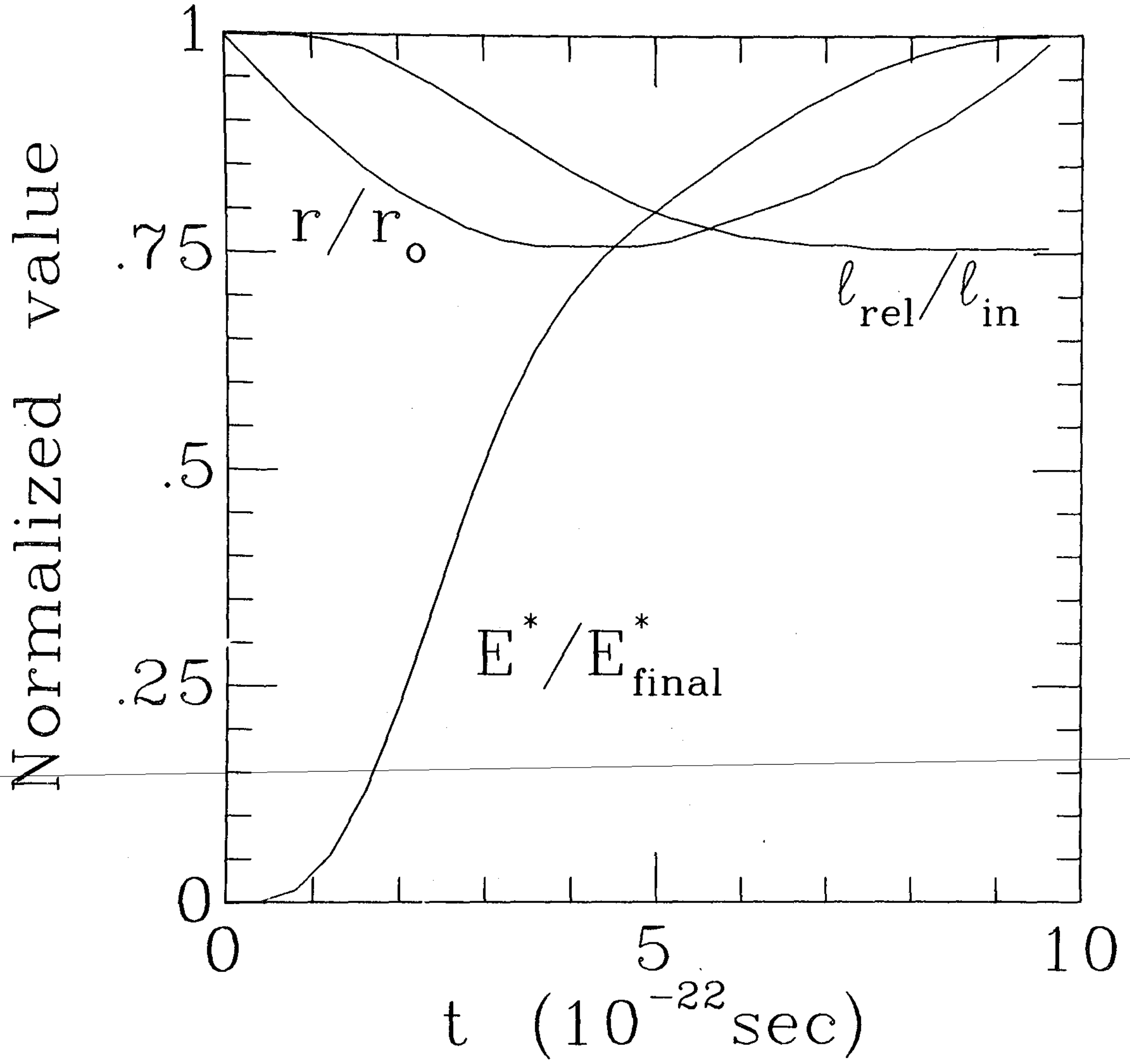

XBL7910-12528

Fig. 28

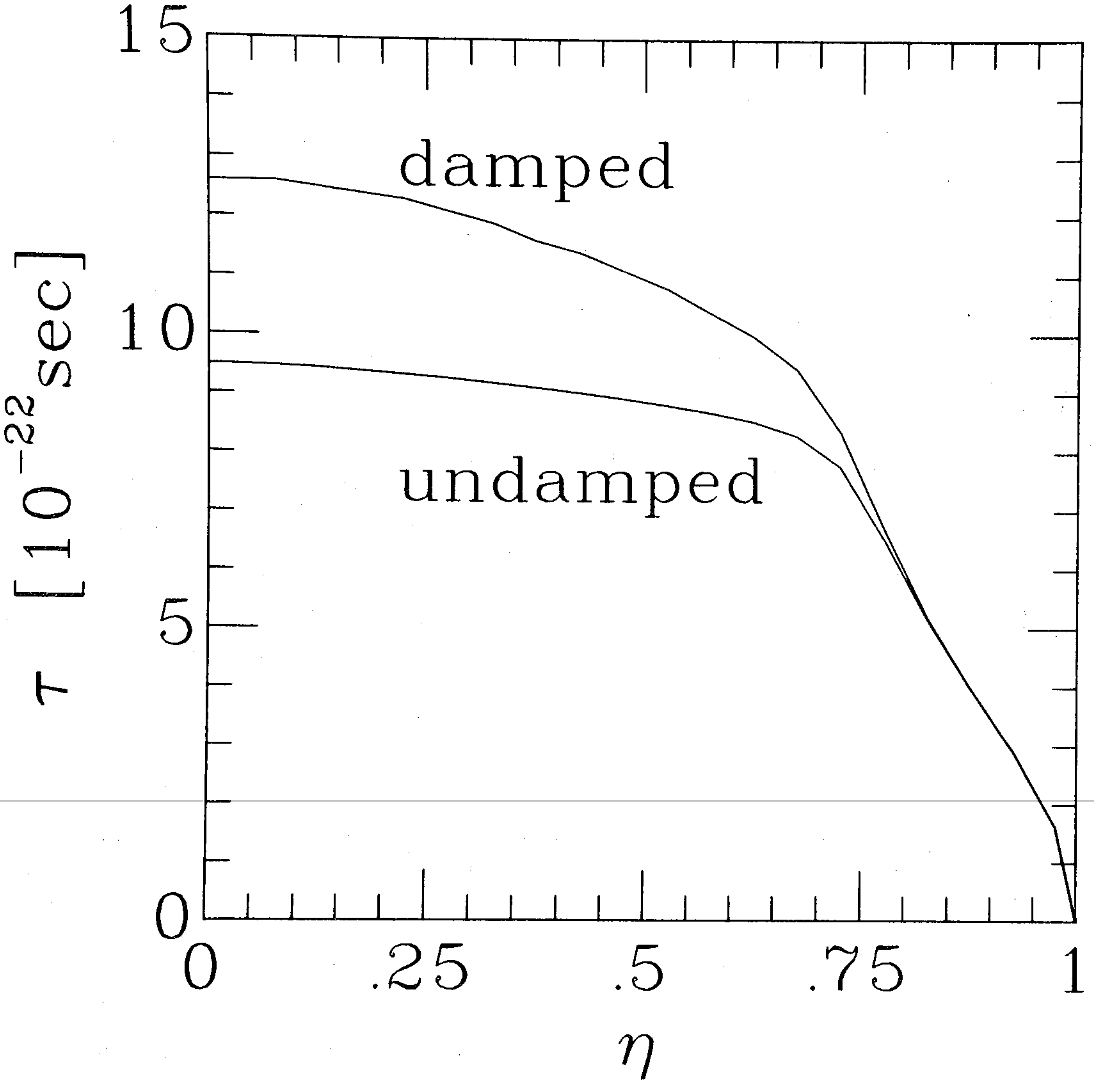

XBL7910-12529

Fig. 29

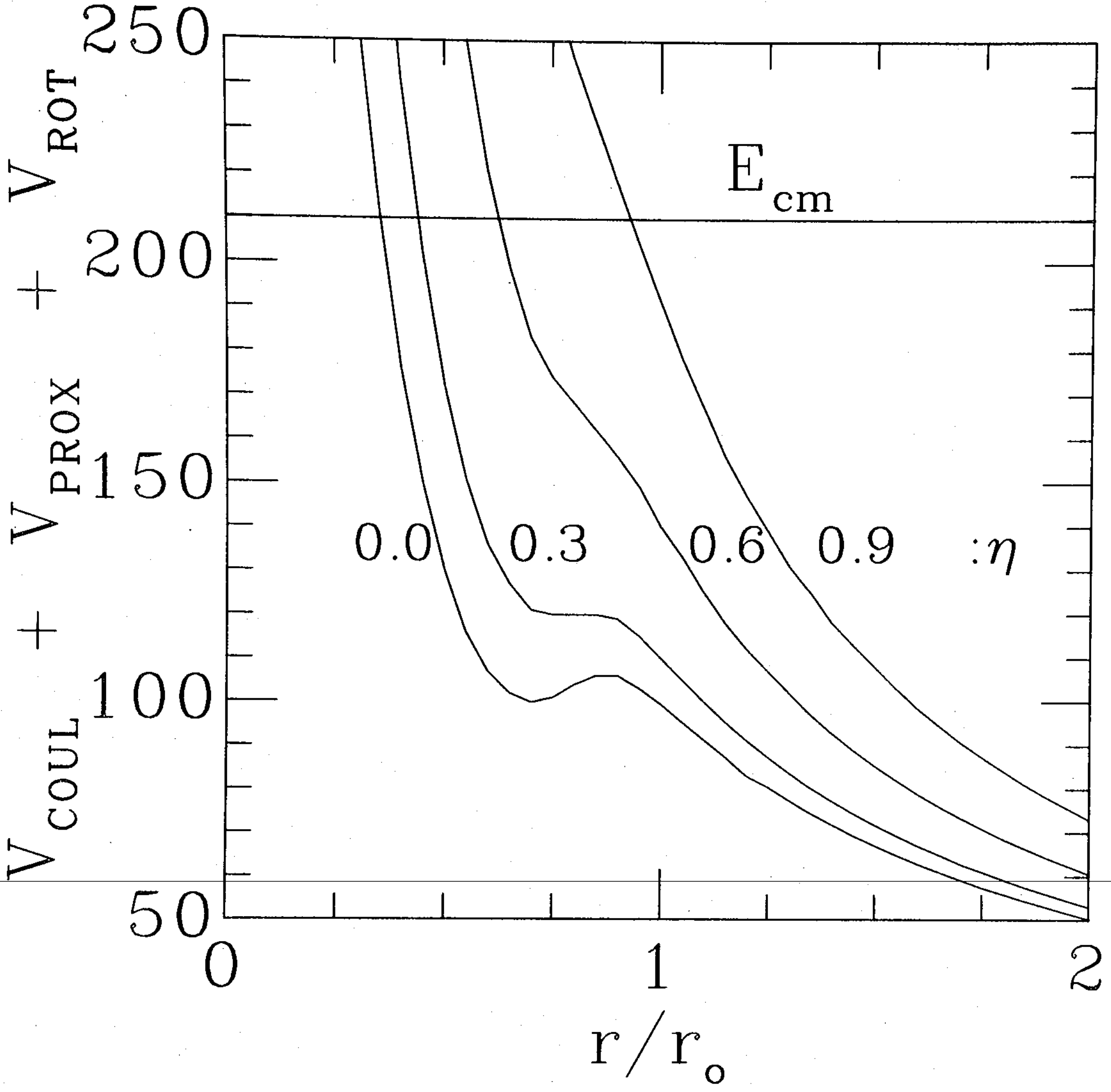

XBL7910-12530

Fig. 30

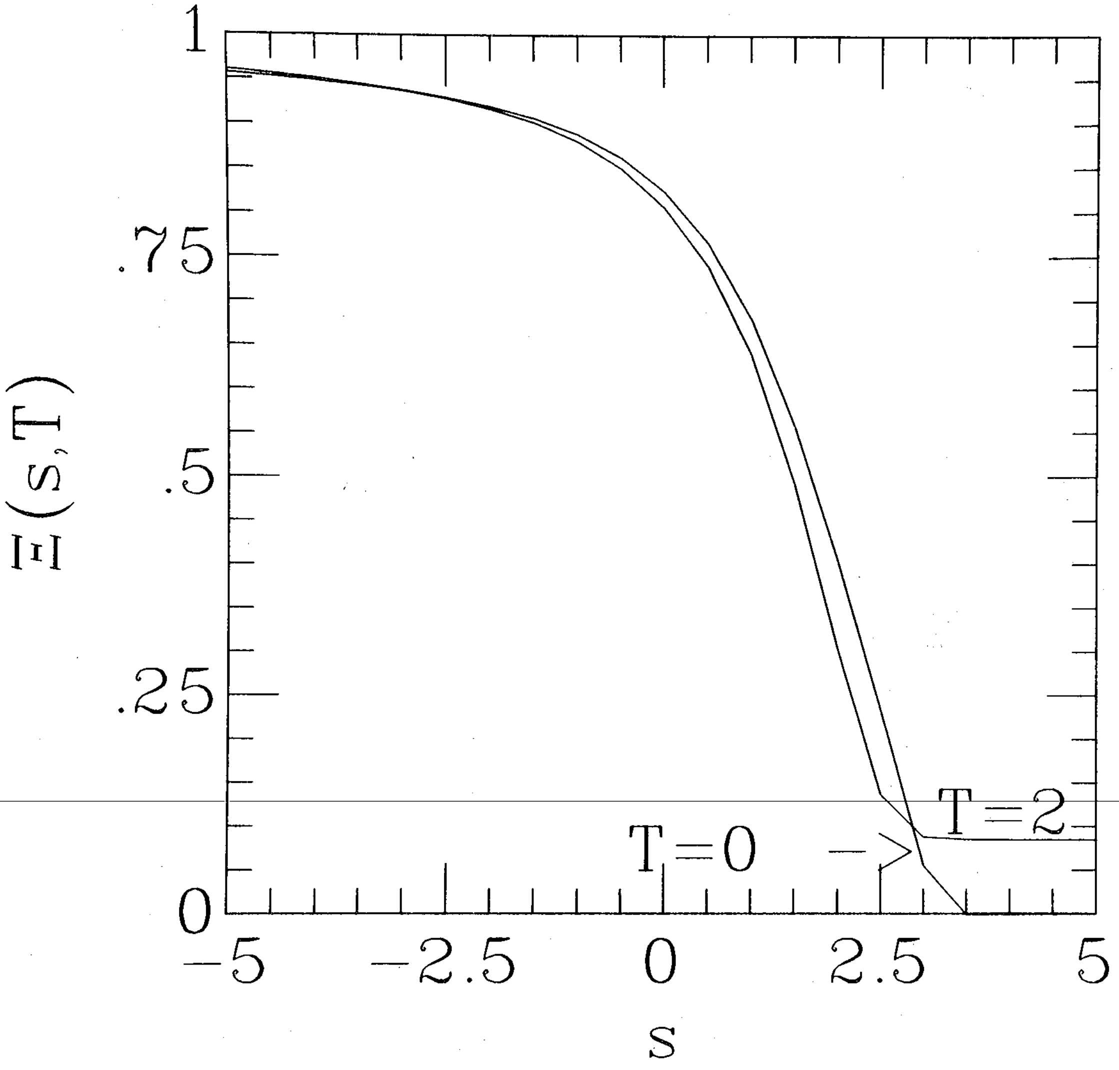

XBL7910-12531

Fig. 31

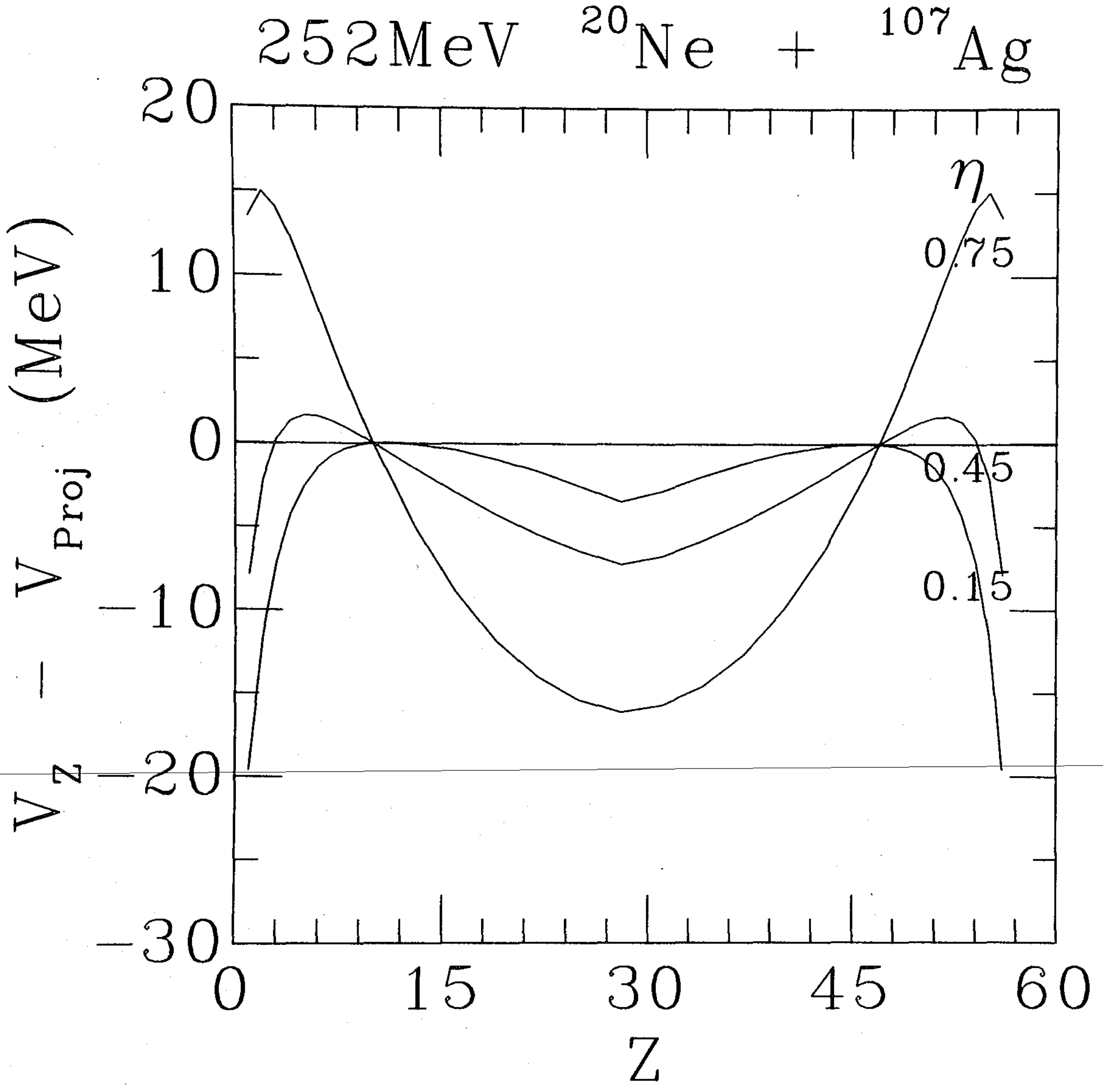

XBL7910-12532

Fig. 32

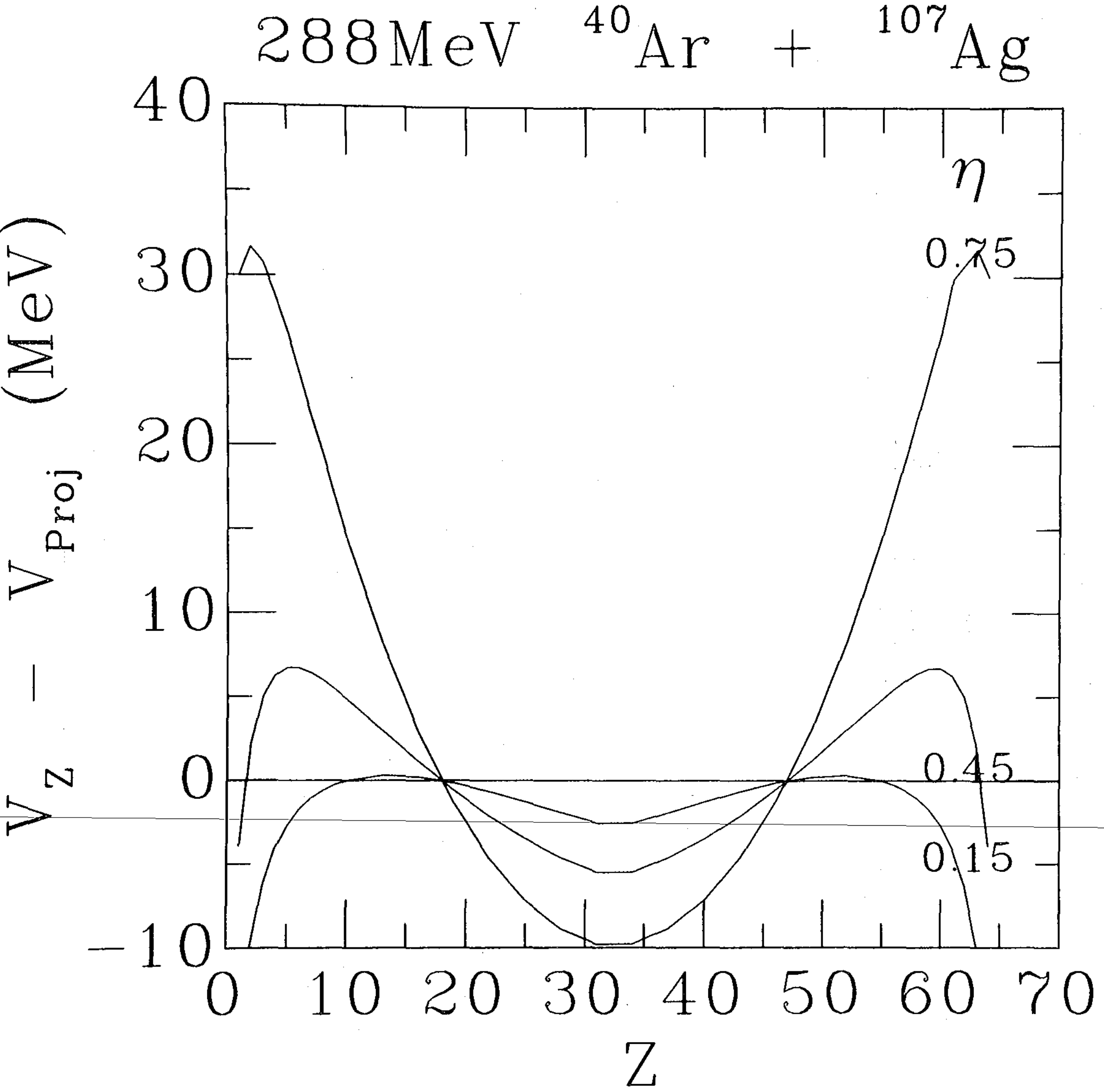

XBL7910-12533

Fig. 33

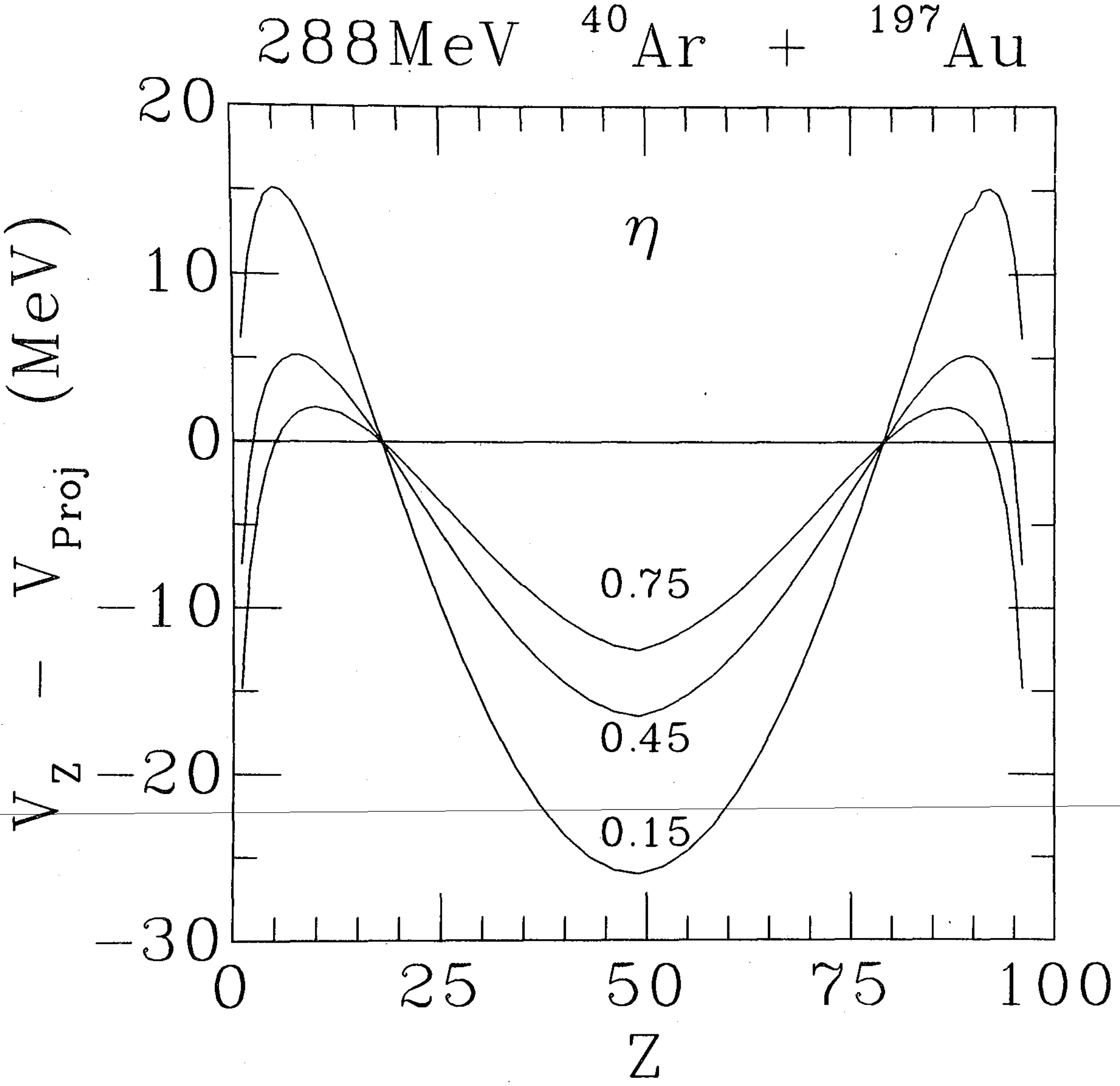

XBL7910-12534

Fig. 34

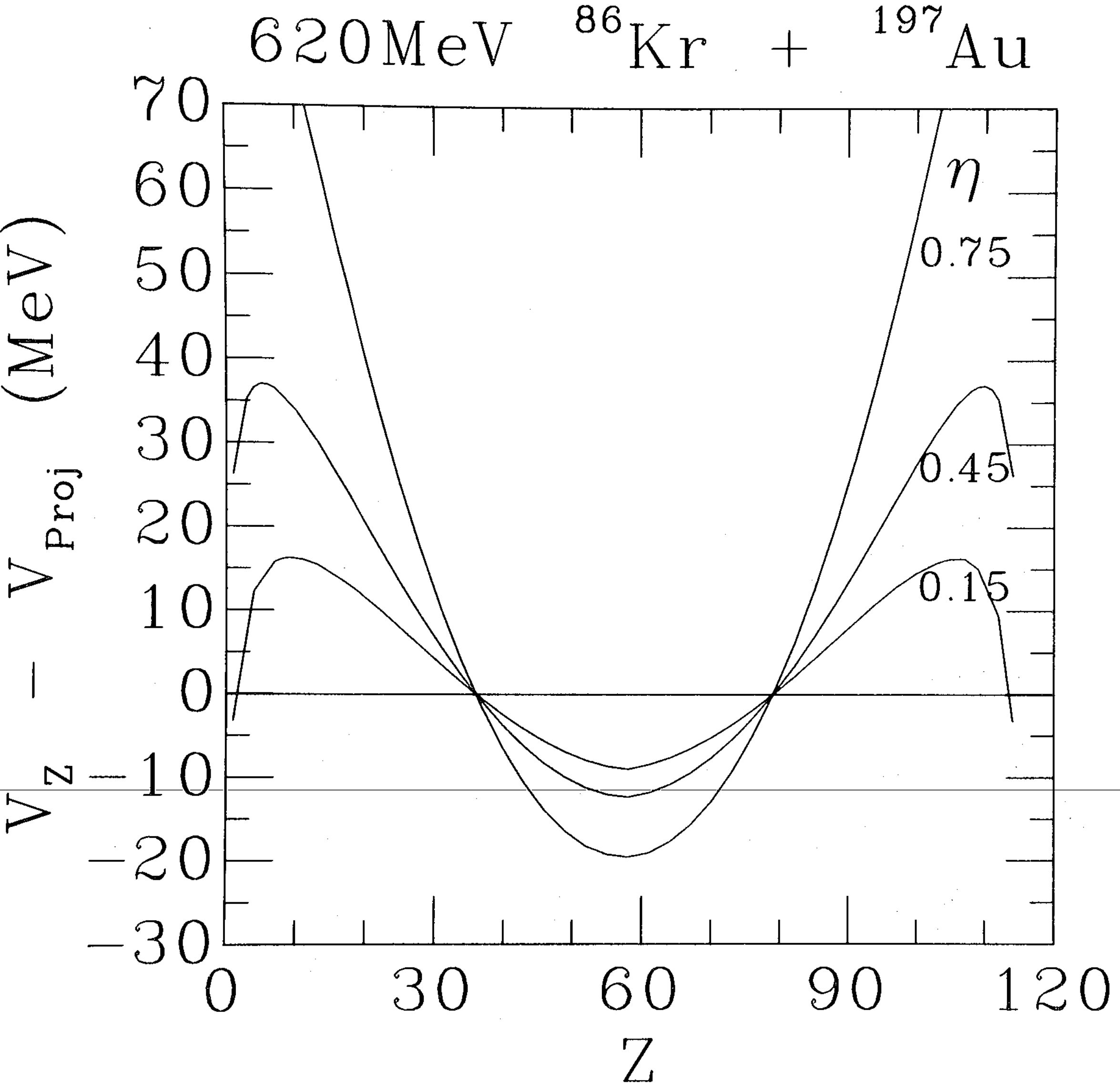

XBL7910-12535

Fig. 35

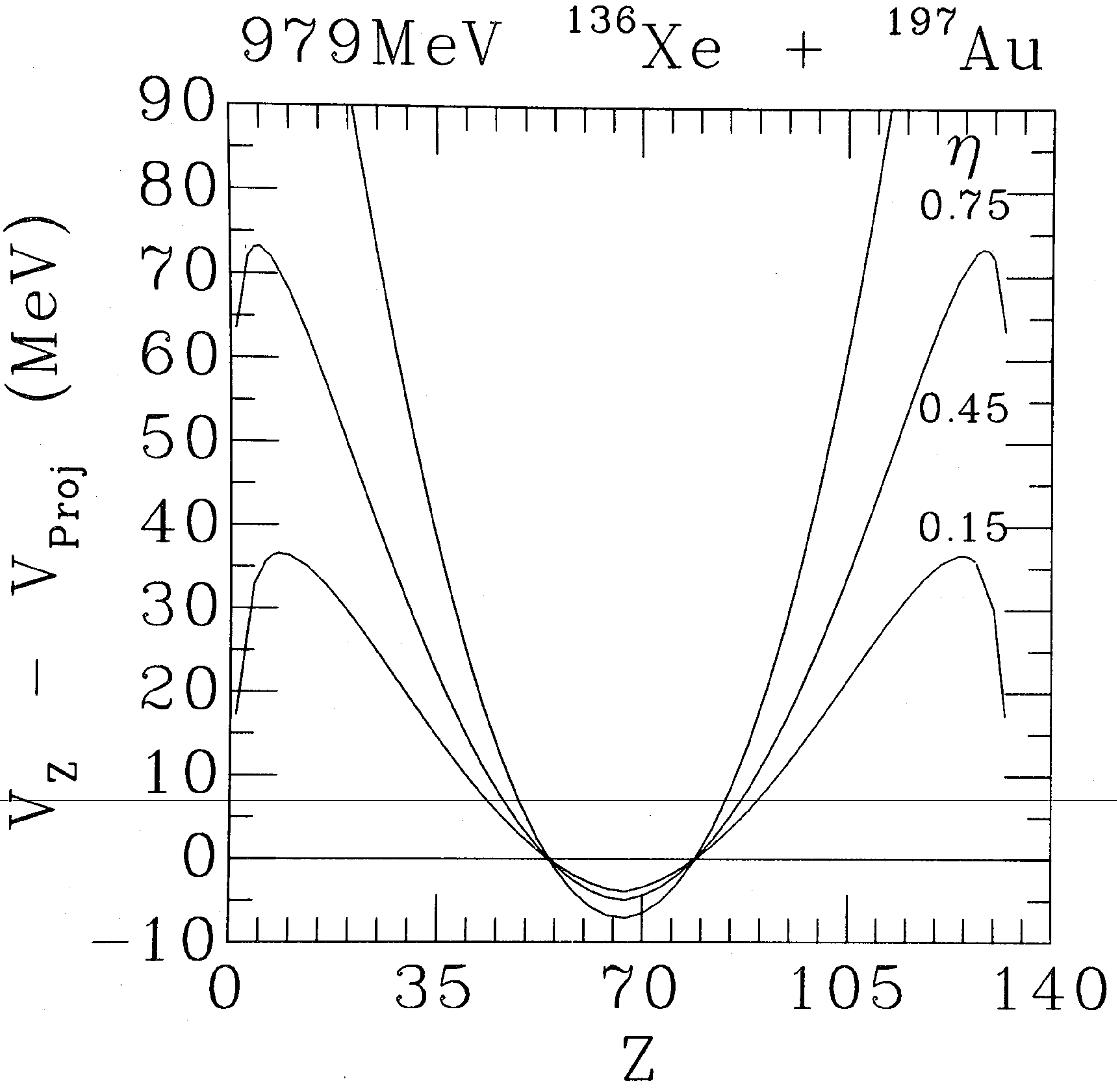

XBL7910-12536

Fig. 36

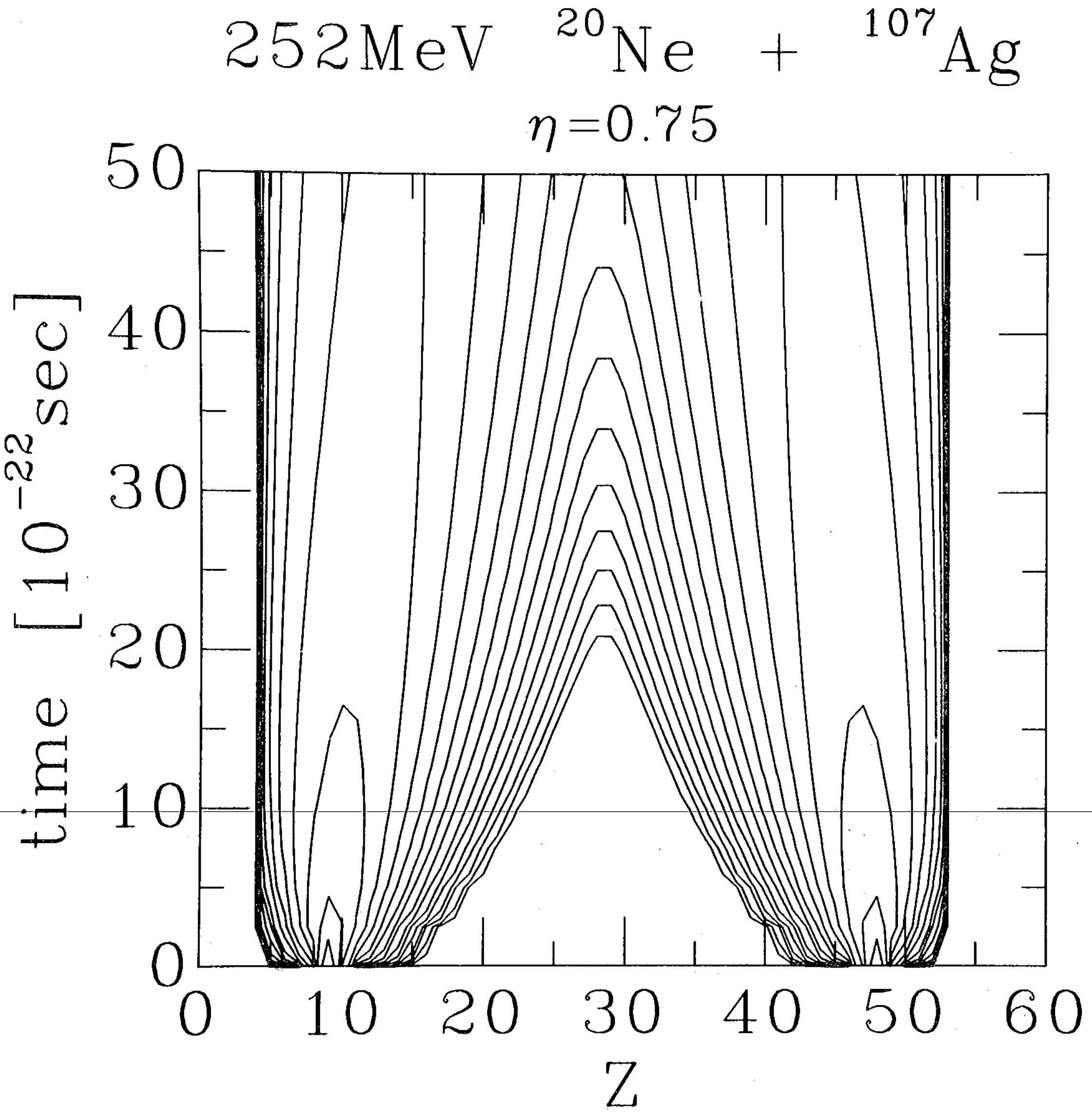

XBL7910-12537

Fig. 37a

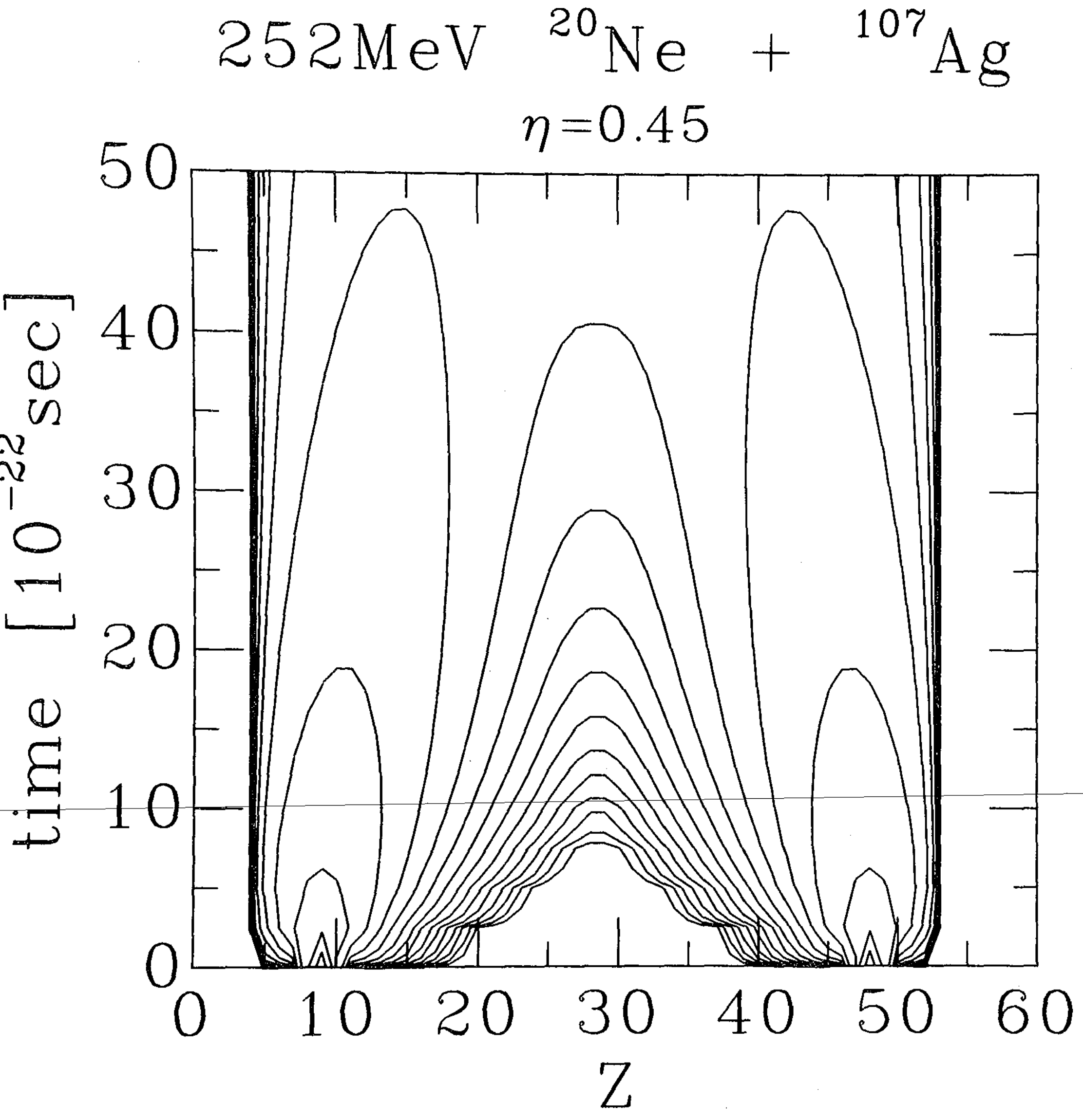

XBL7910-12538

Fig. 37b

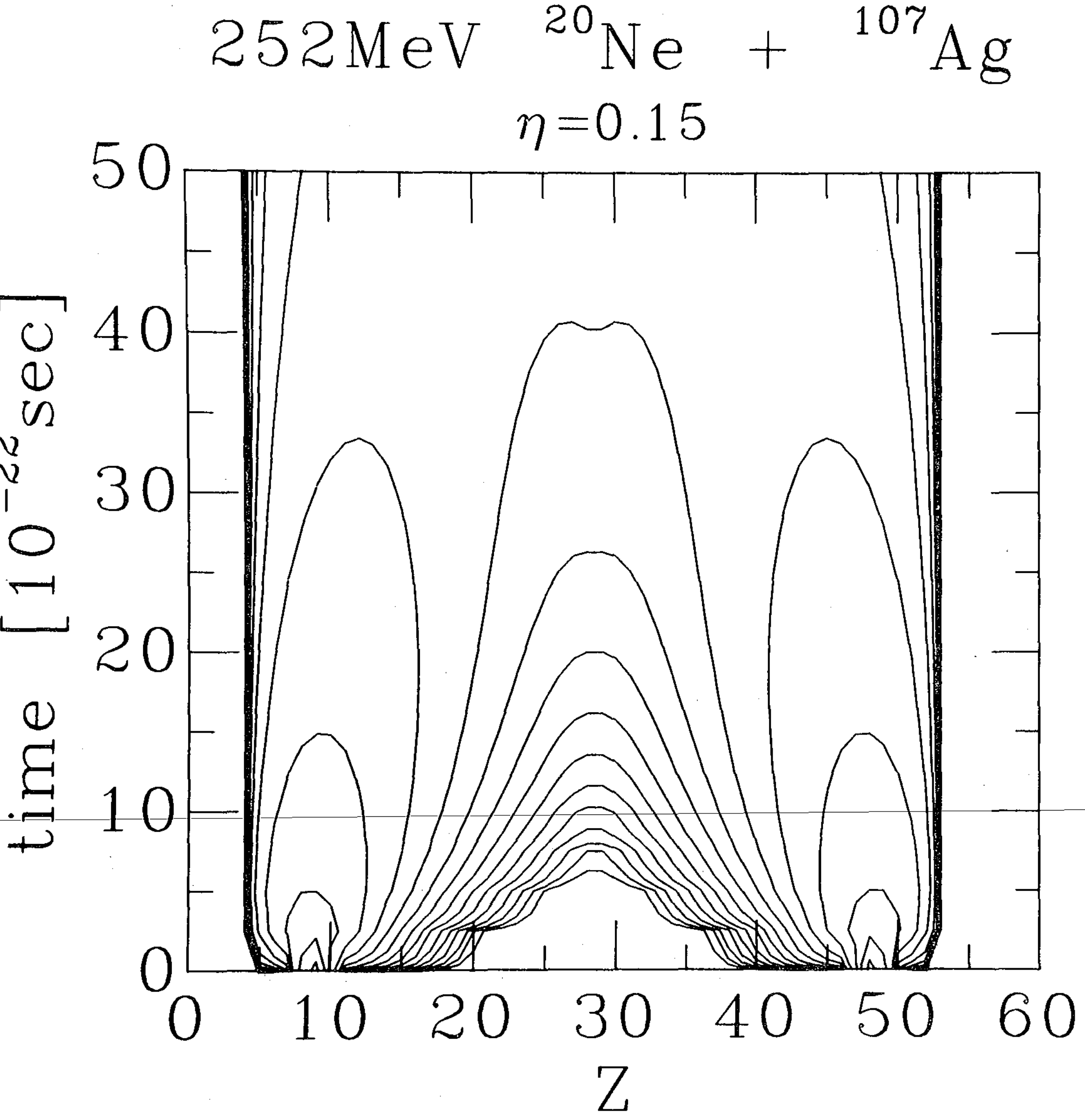

XBL7910-12539

Fig. 37c

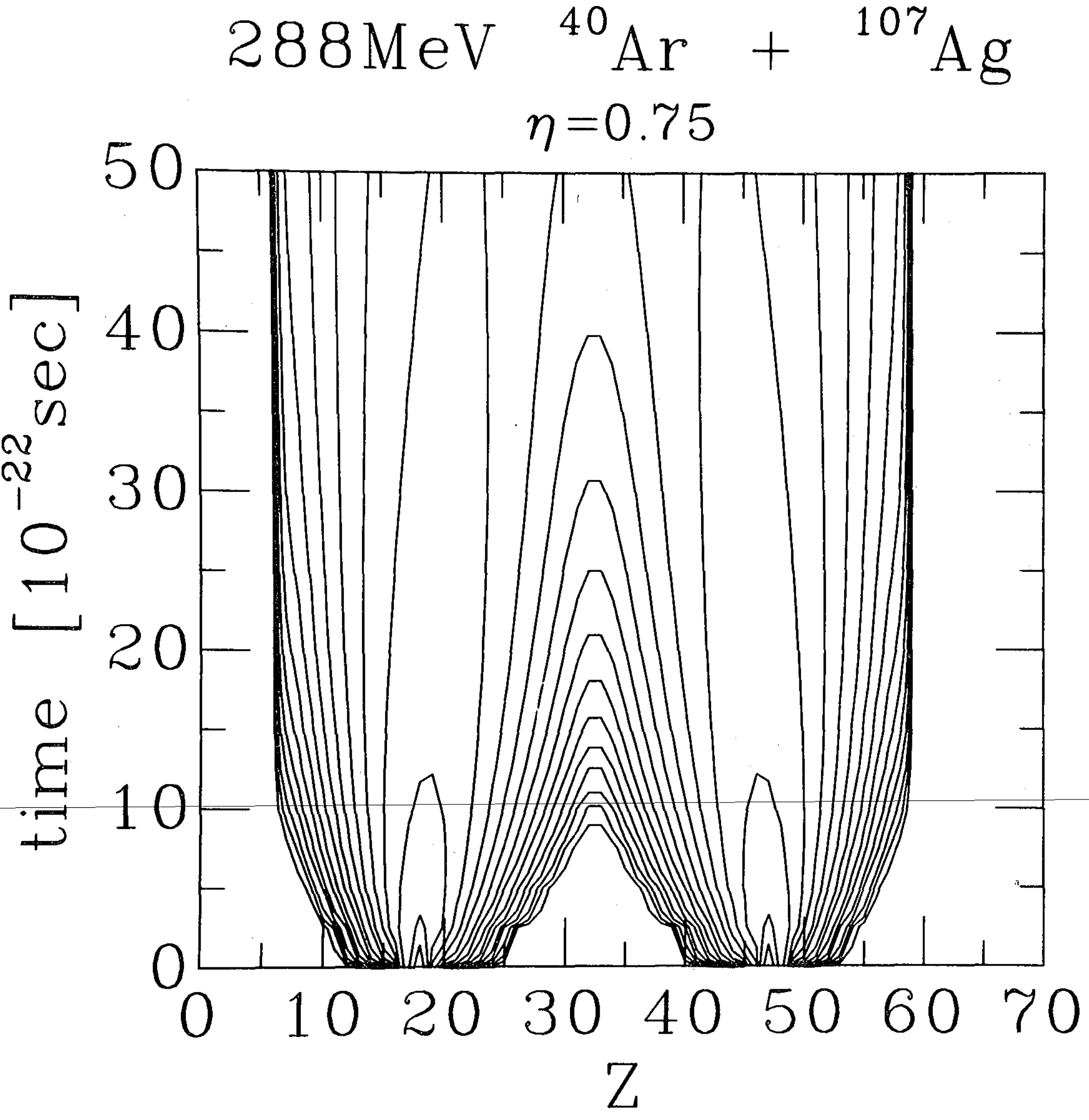

XBL7910-12540

Fig. 38a

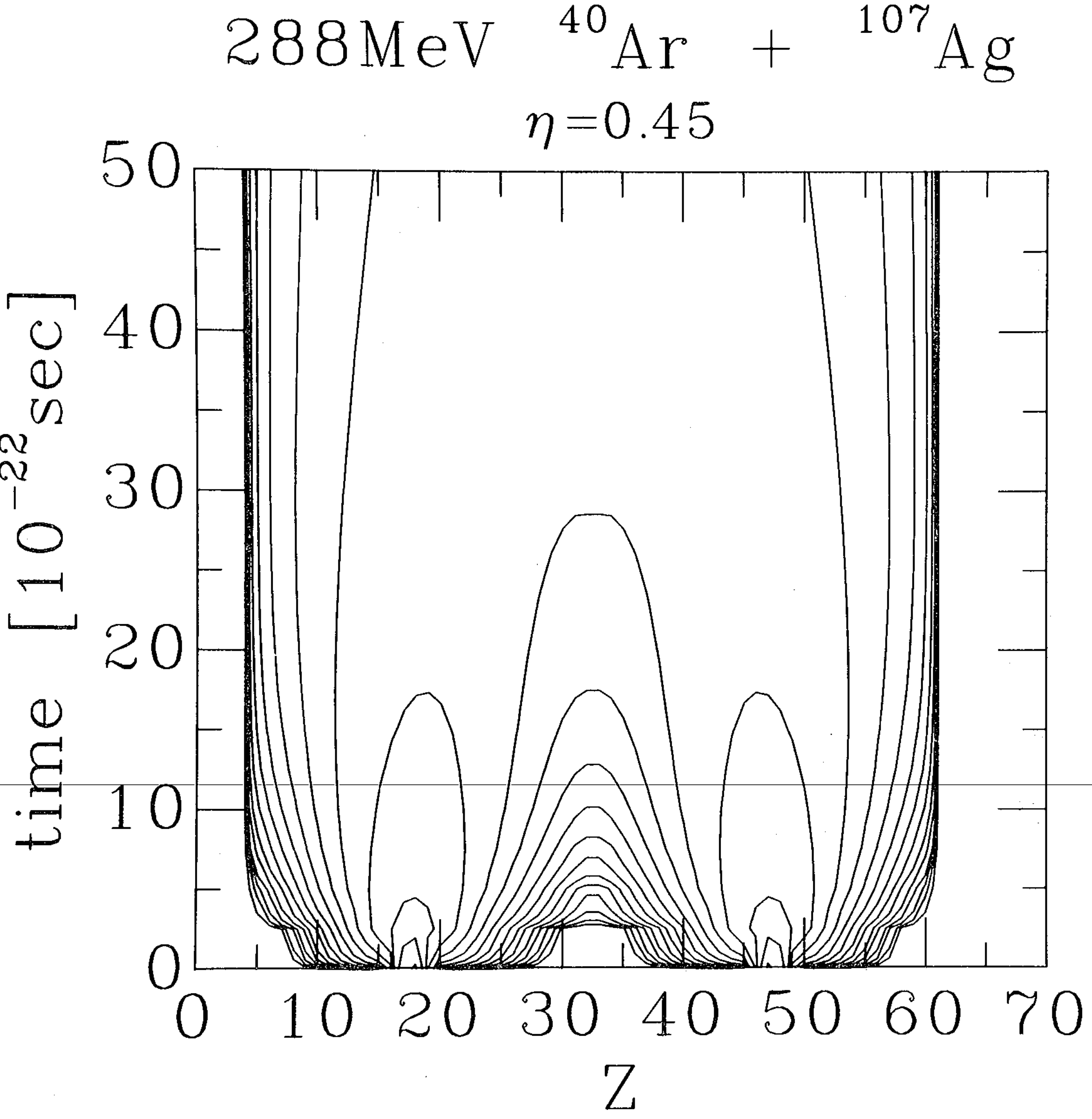

XBL7910-12541

Fig. 38b

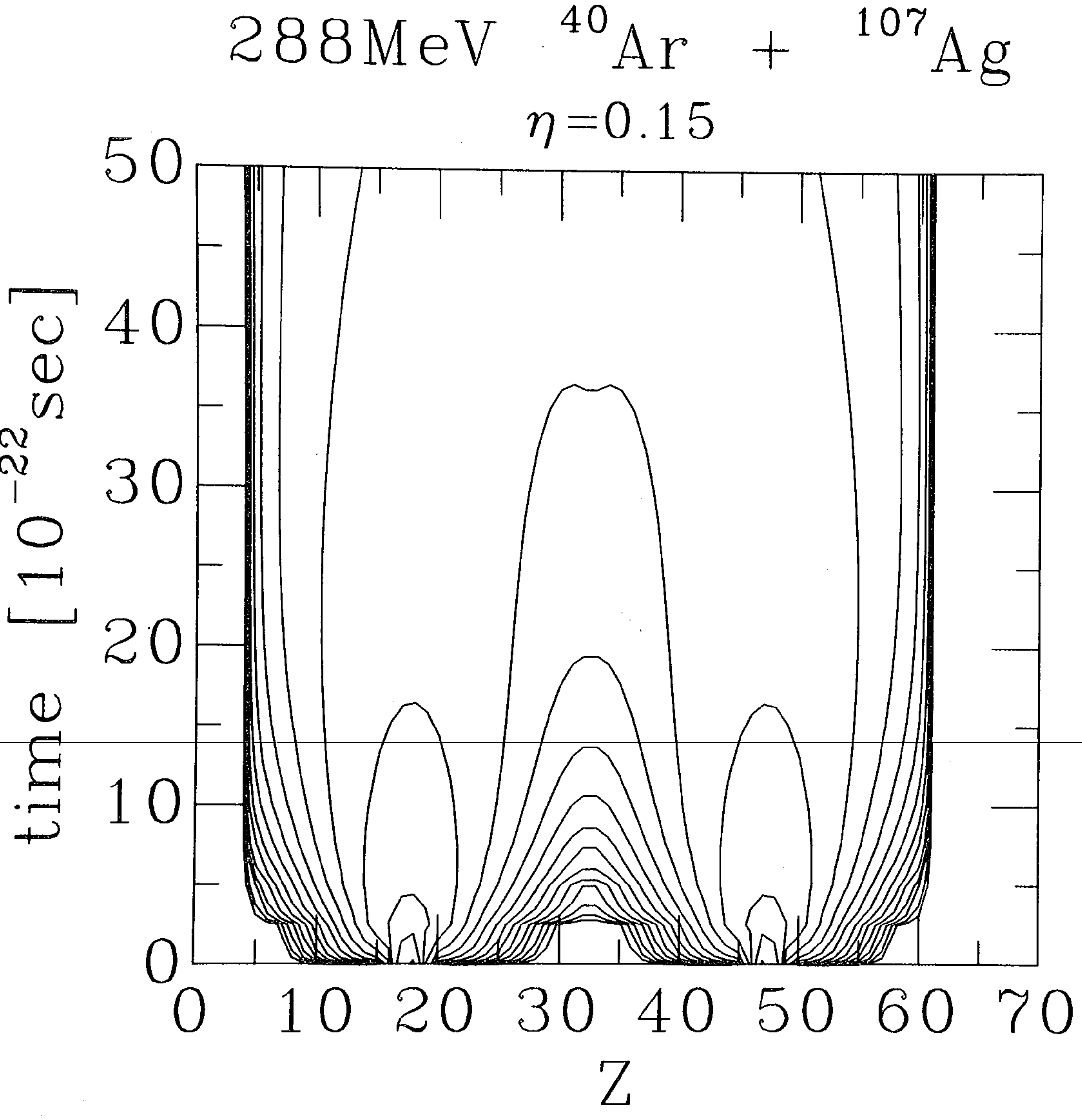

XBL7910-12542

Fig. 38c

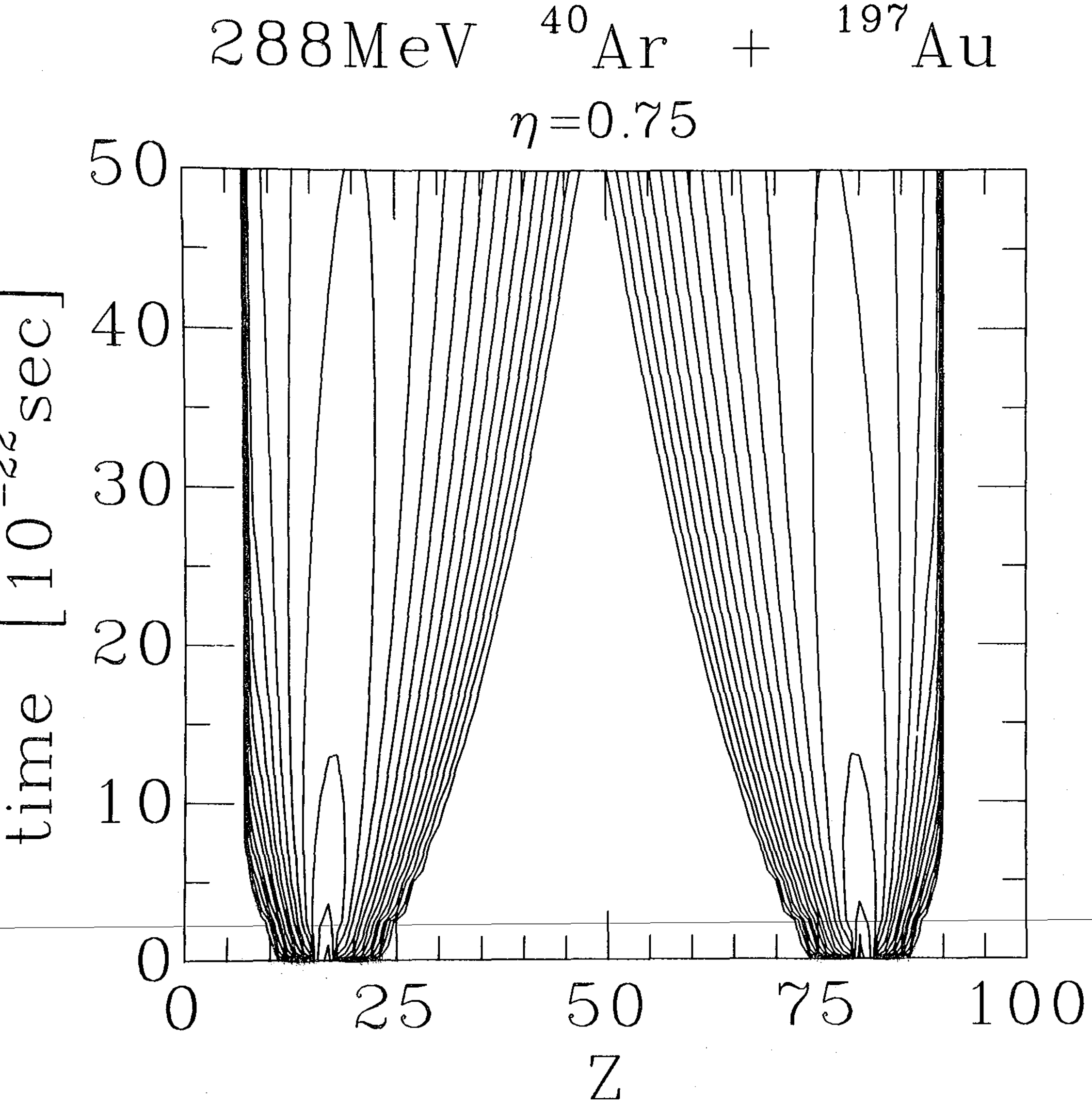

XBL7910-12543

Fig. 39a

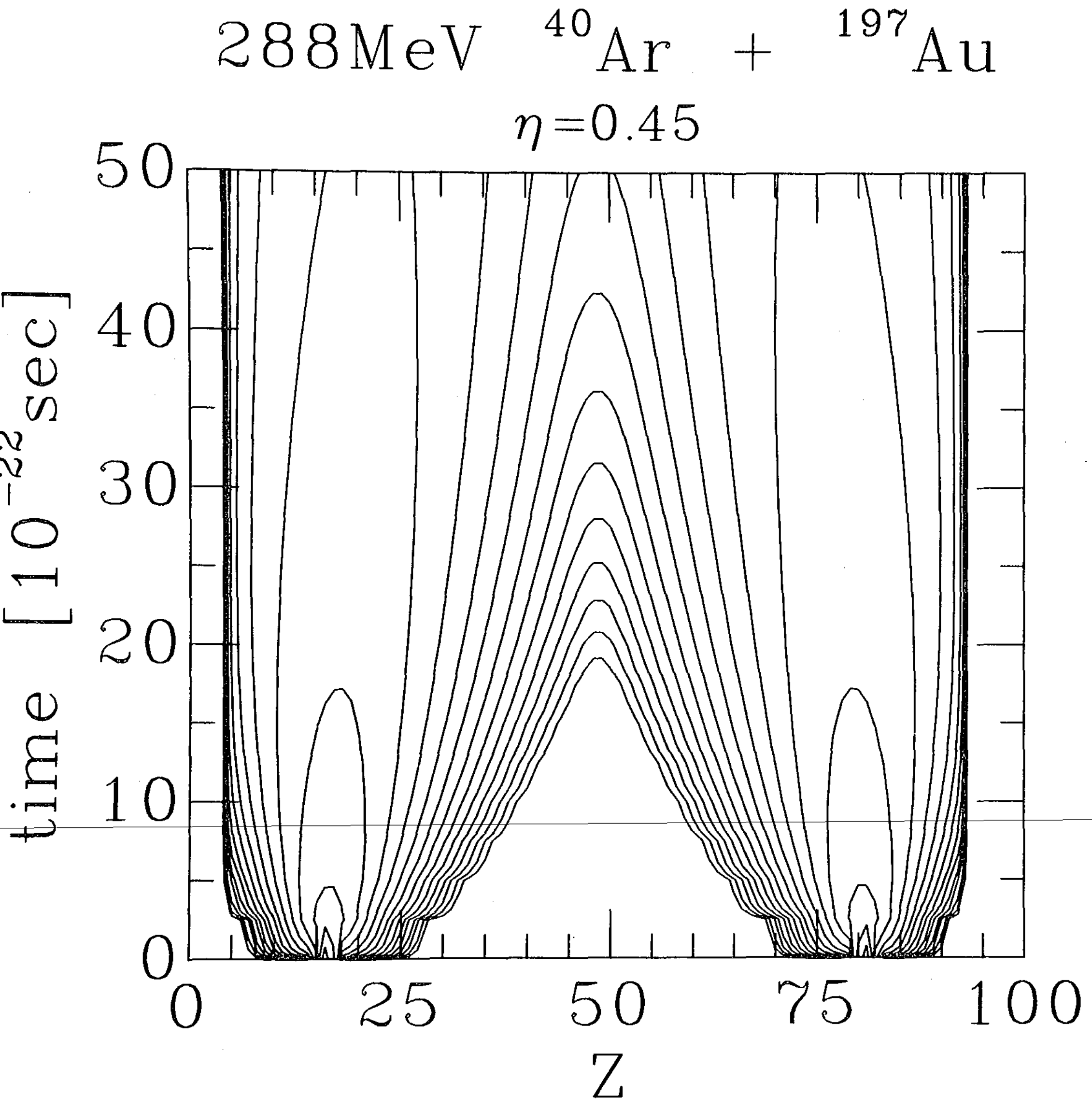

XBL7910-12544

Fig. 39b

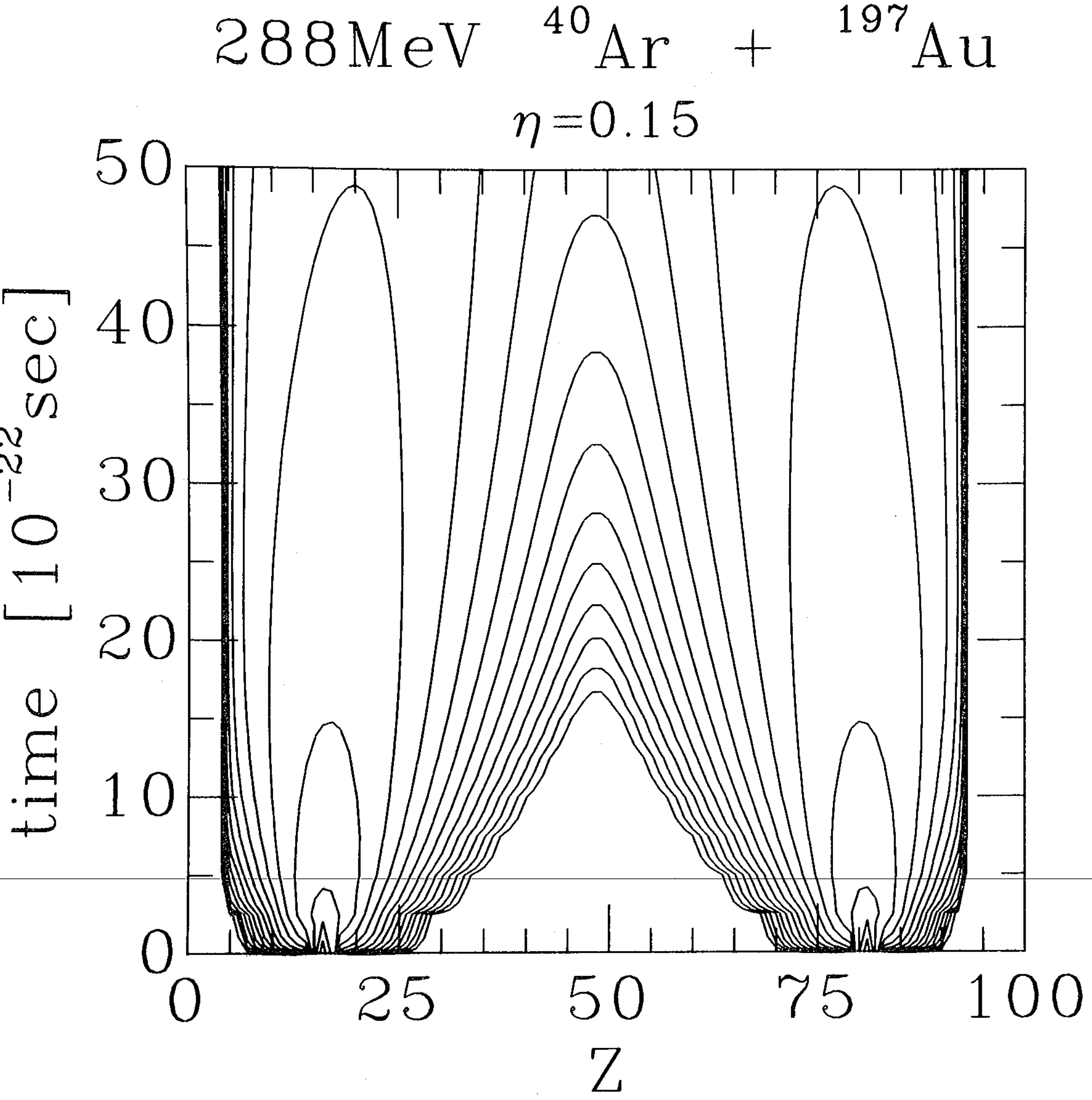

XBL7910-12545

Fig. 39c

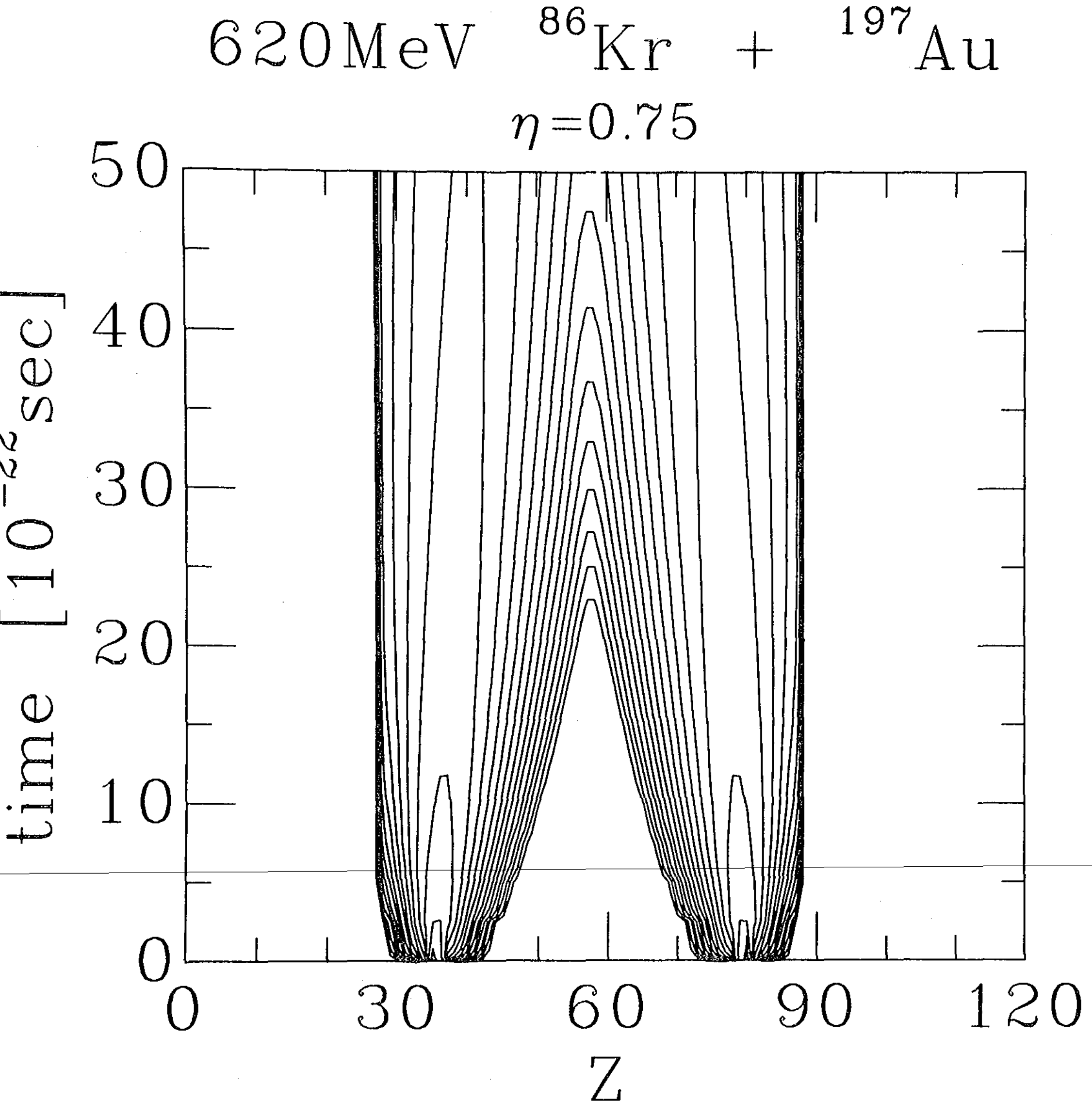

XBL7910-12546

Fig. 40a

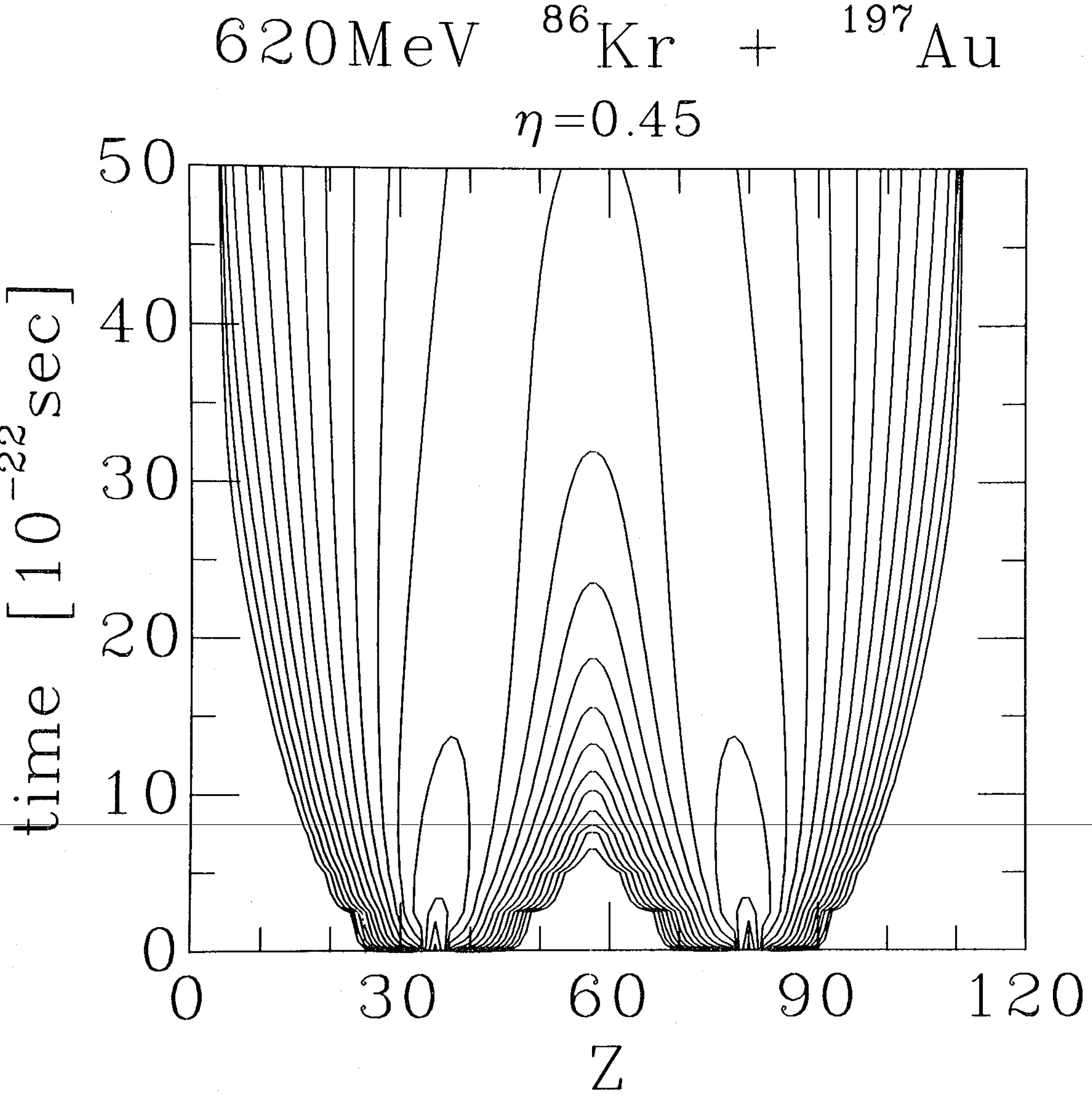

XBL7910-12547

Fig. 40b

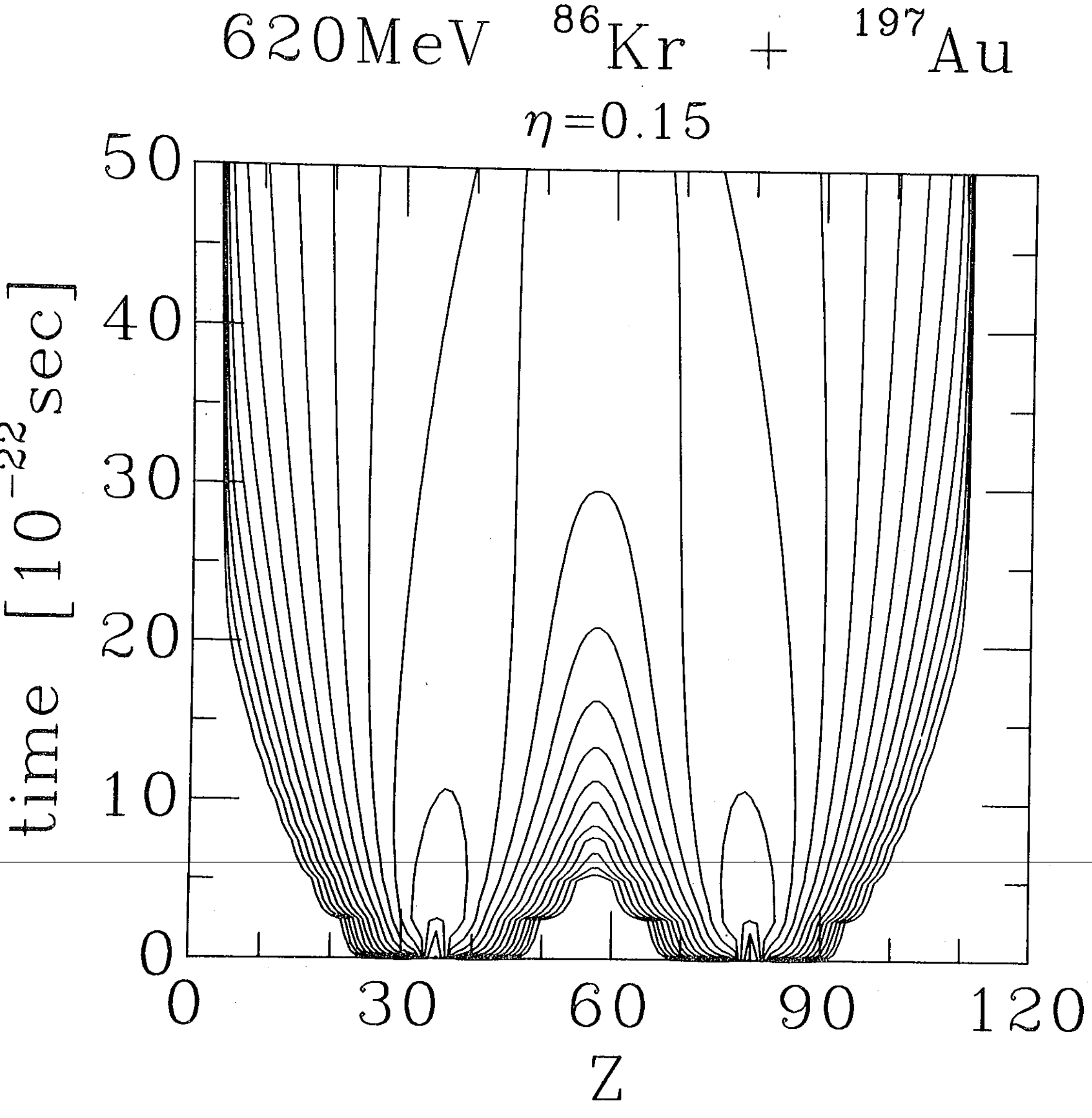

XBL7910-12548

Fig. 40c

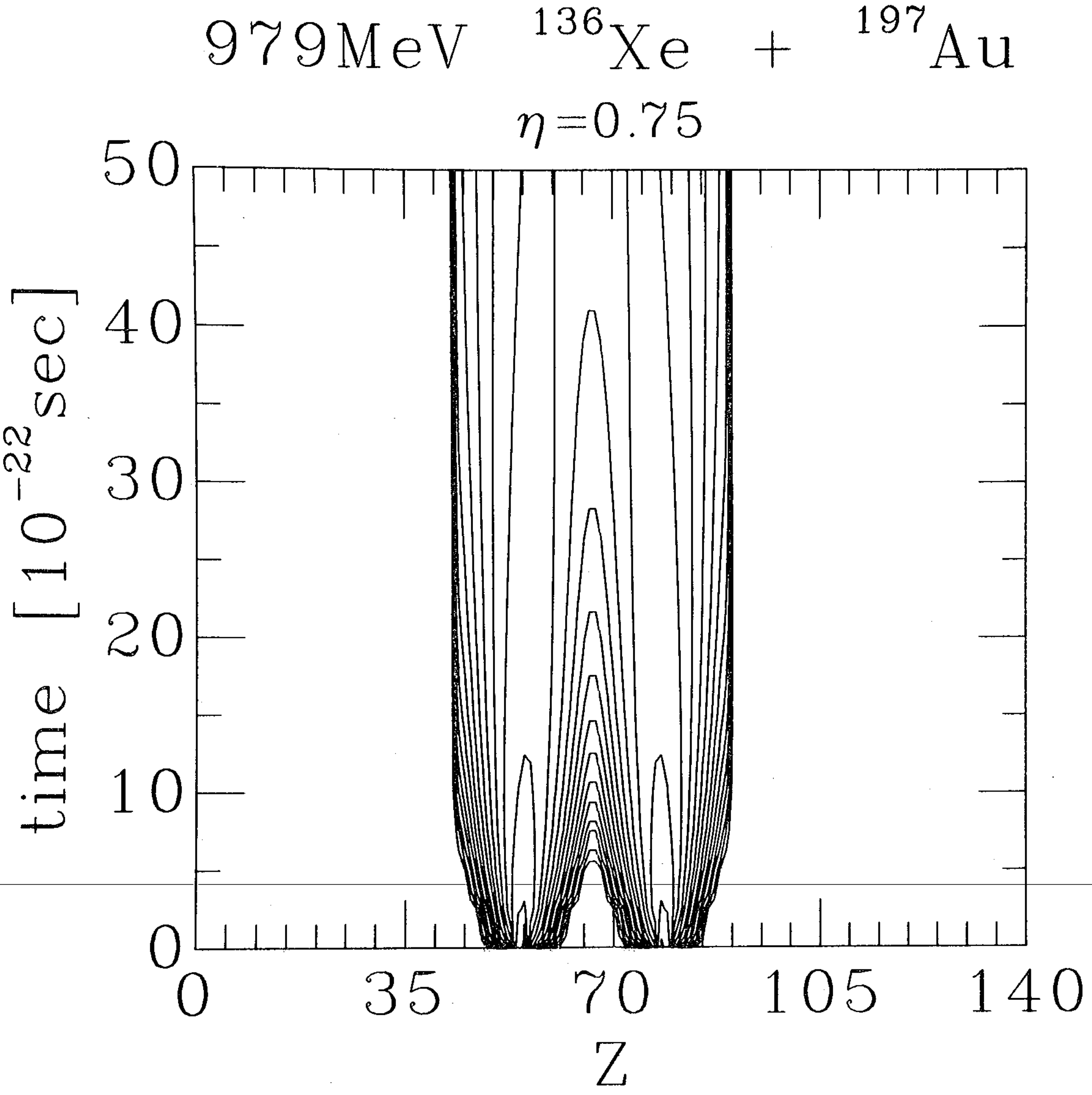

XBL7910-12549

Fig. 41a

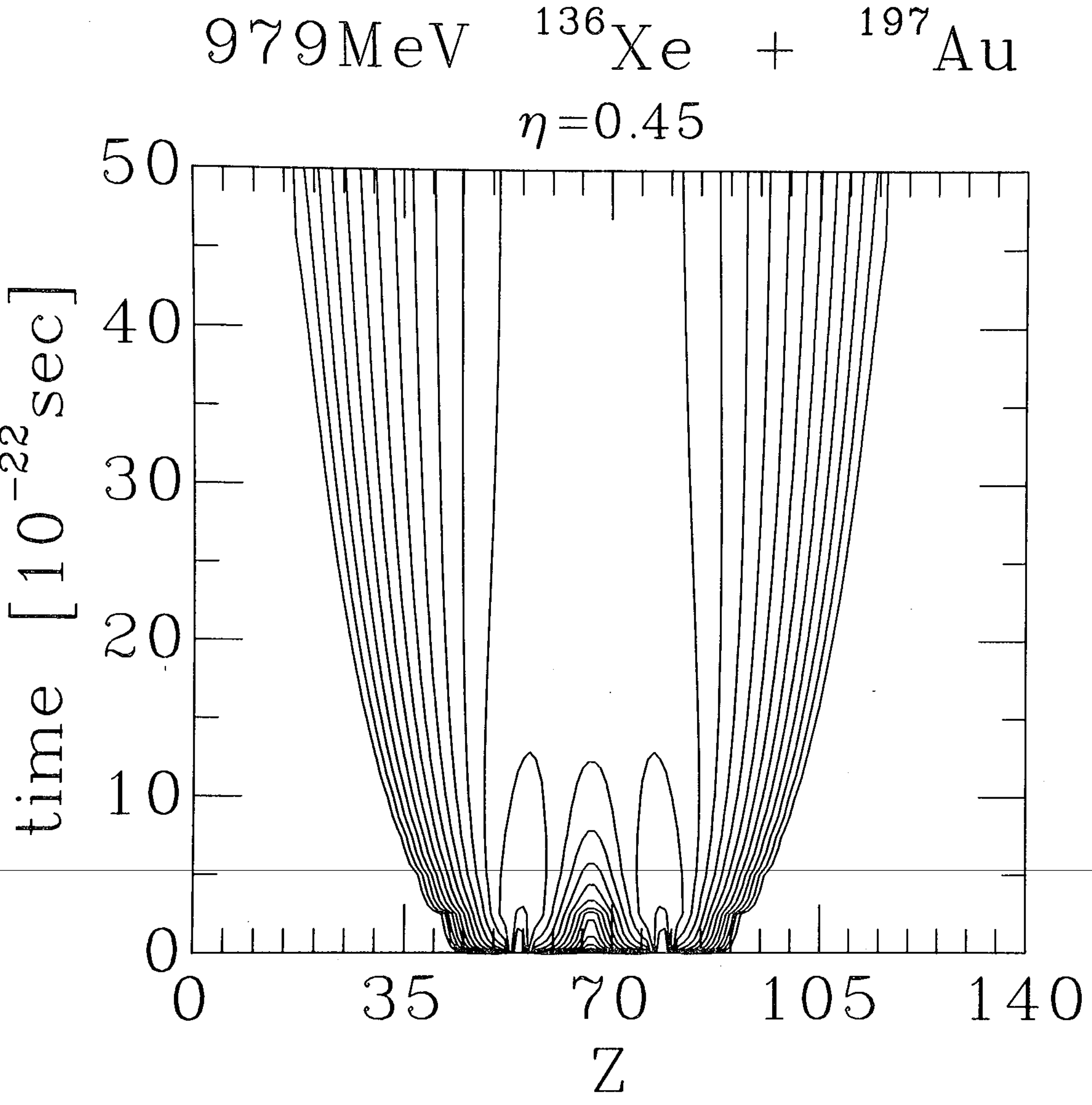

XBL7910-12550

Fig. 41b

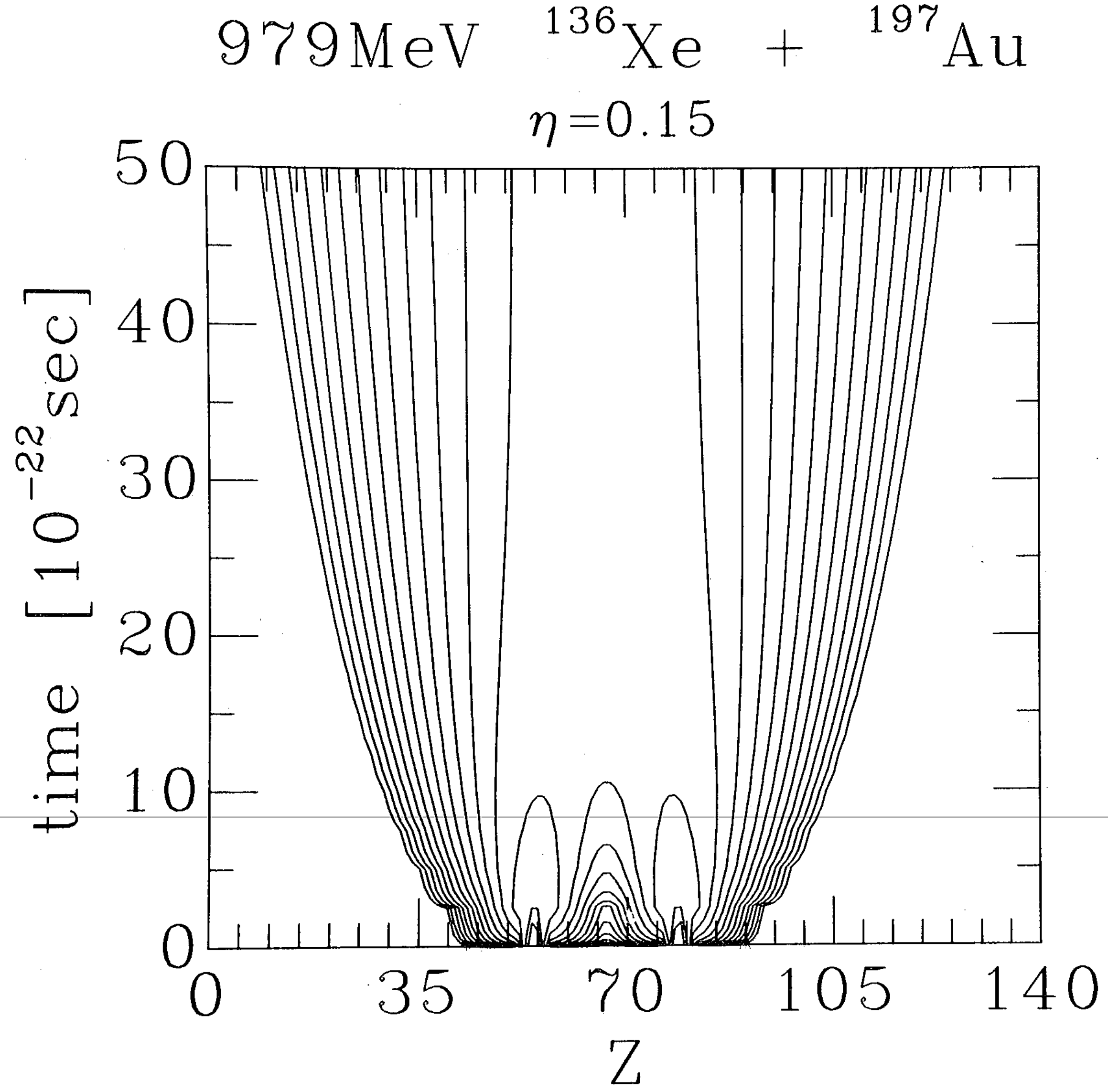

XBL7910-12551

Fig. 41c

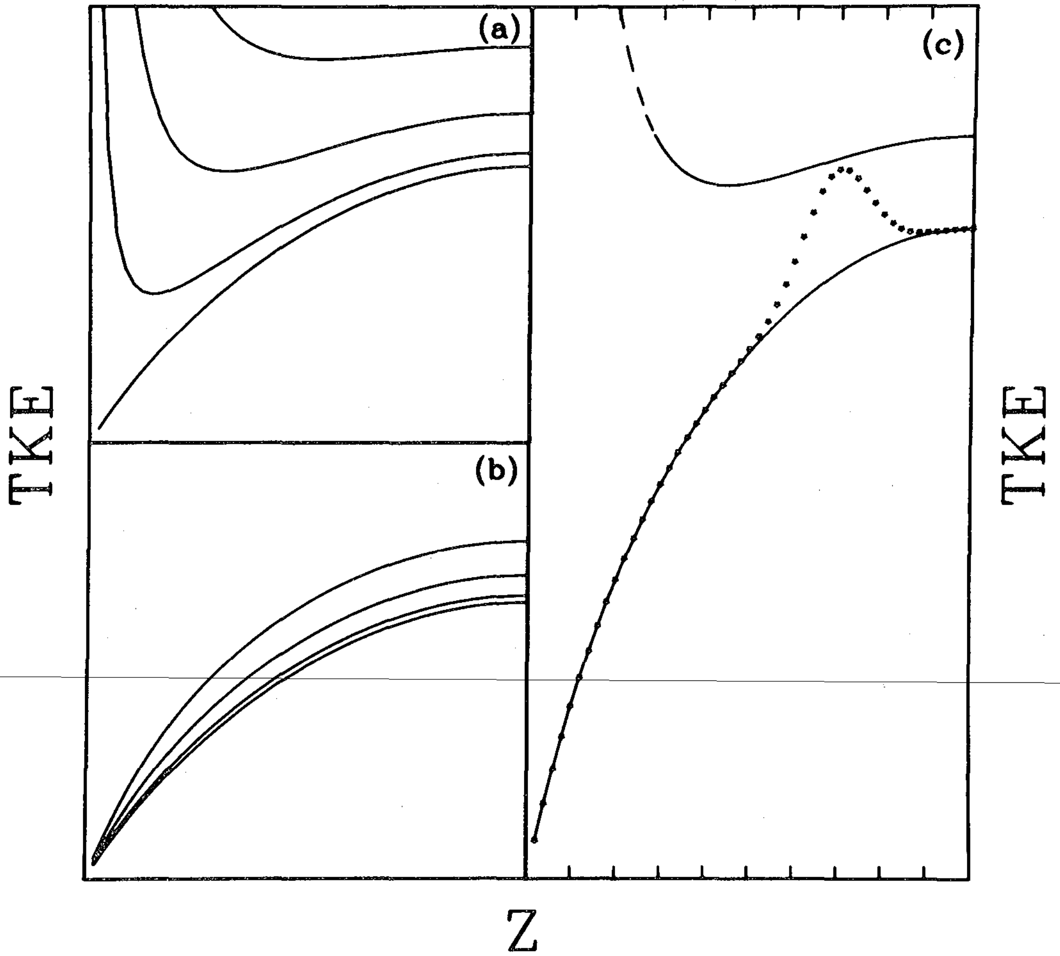

XBL7711-10426

Fig. 42

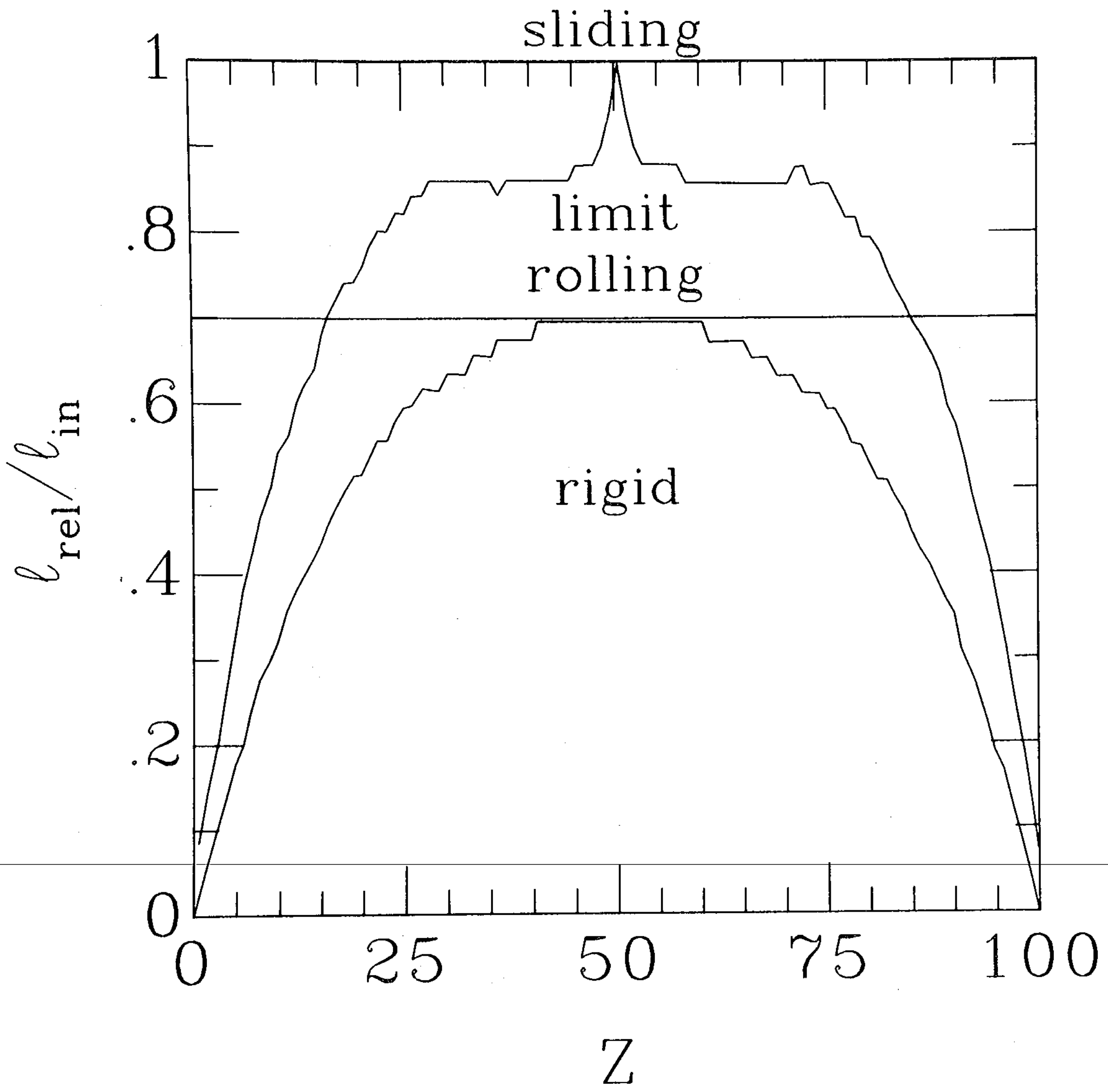

XBL7910-12552

Fig. 43

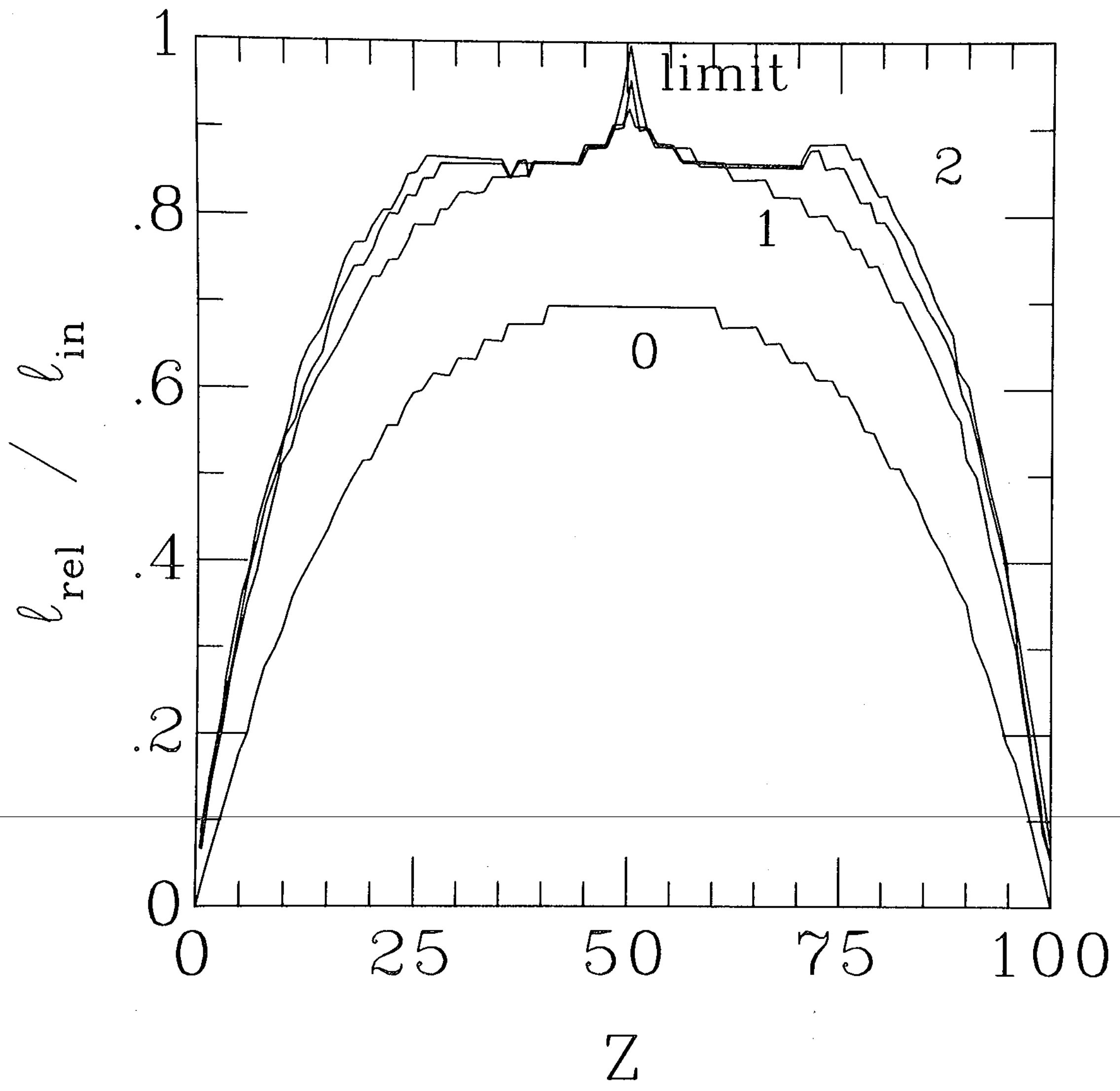

XBL7910-12553

Fig. 44

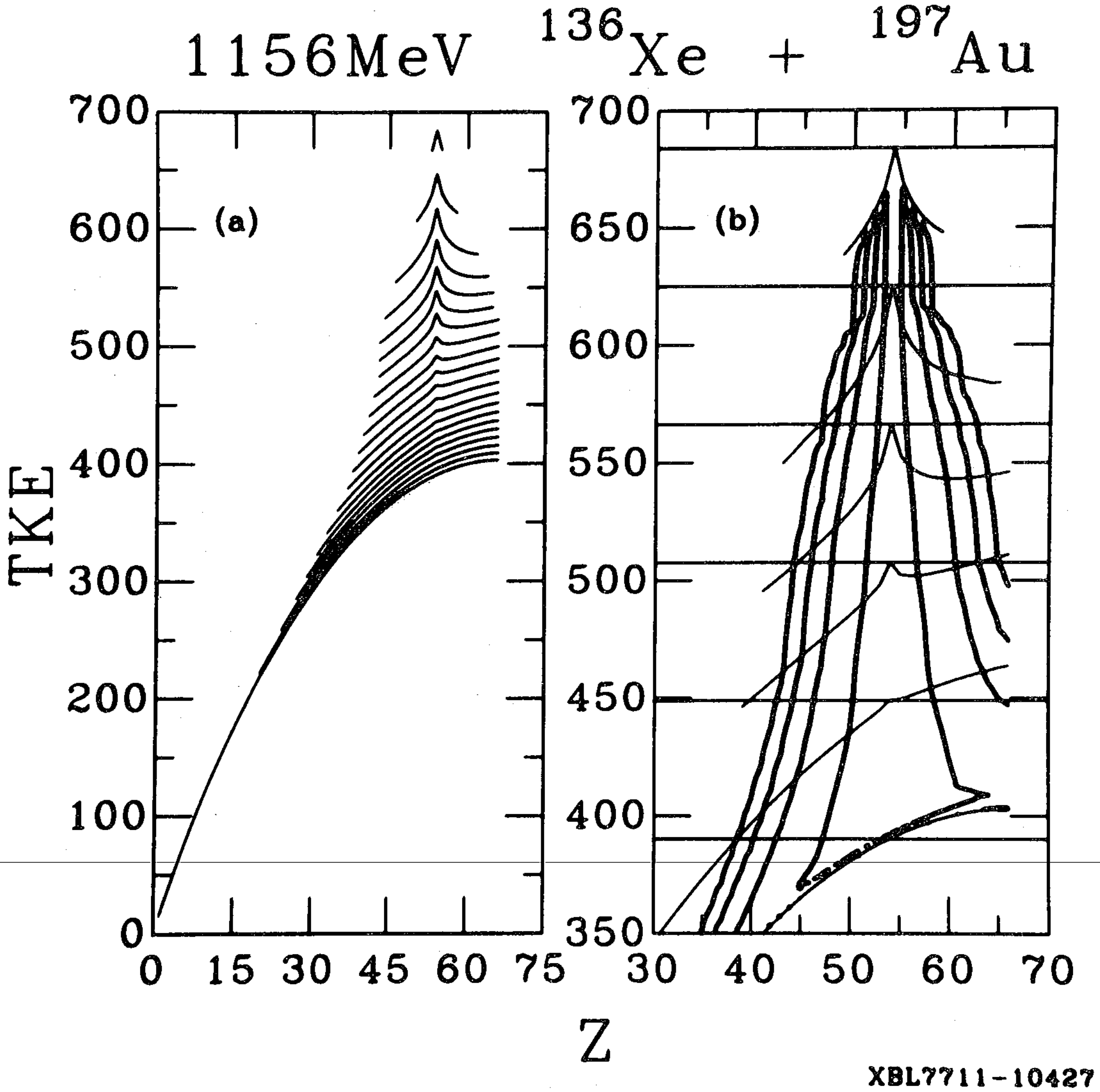
1156MeV ^{136}Xe + ^{197}Au
TKE
(a)
0
100
200
300
400
500
600
700
0
15
30
45
60
75
(b)
350
400
450
500
550
600
650
700
30
40
50
60
70
Z
XBL7711-10427

Fig. 45

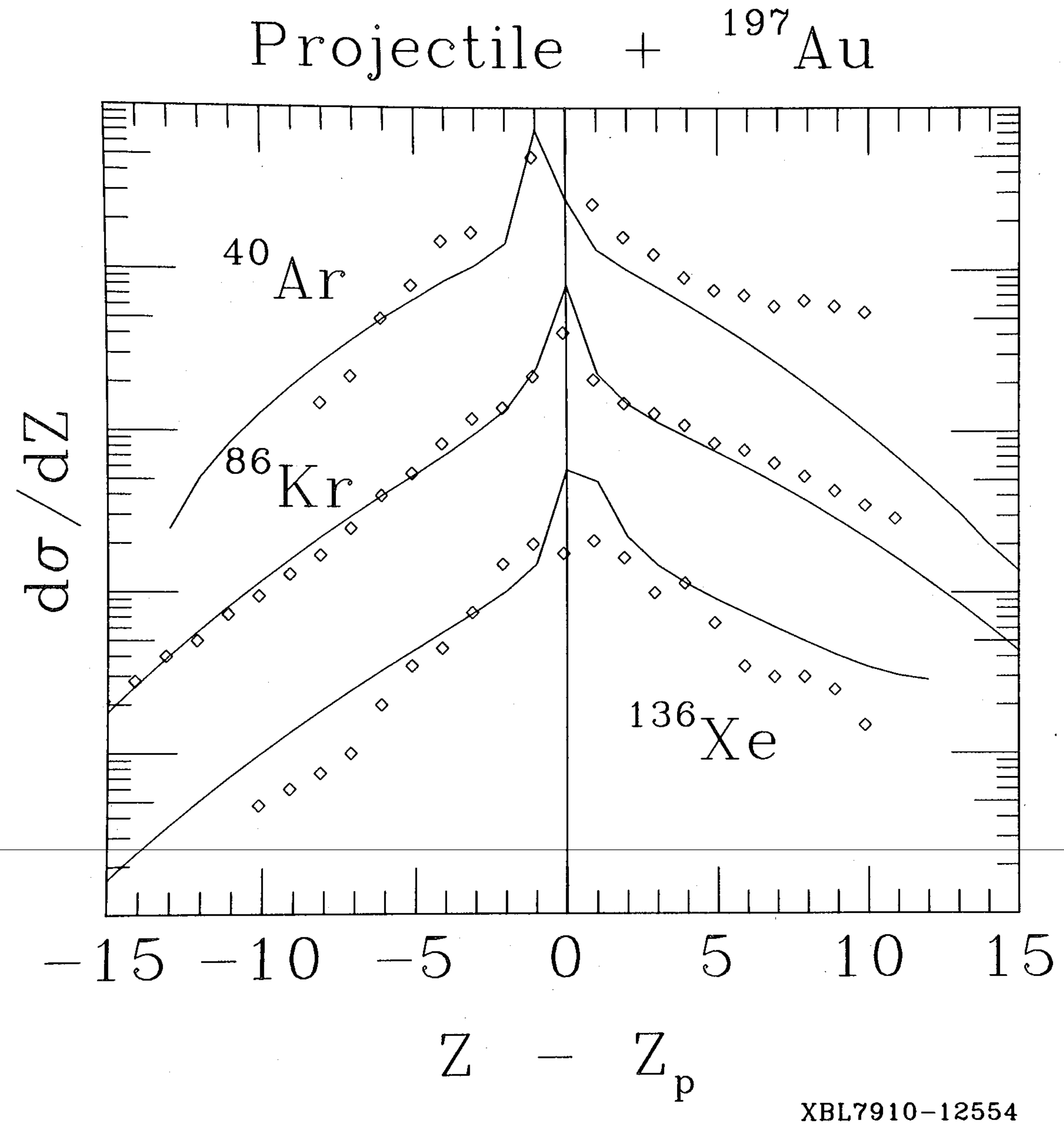
Projectile + ^{197}Au
^{40}Ar
^{86}Kr
^{136}Xe
dσ/dZ
−15
−10
−5
0
5
10
15
Z − Z_p
XBL7910-12554

Fig. 46

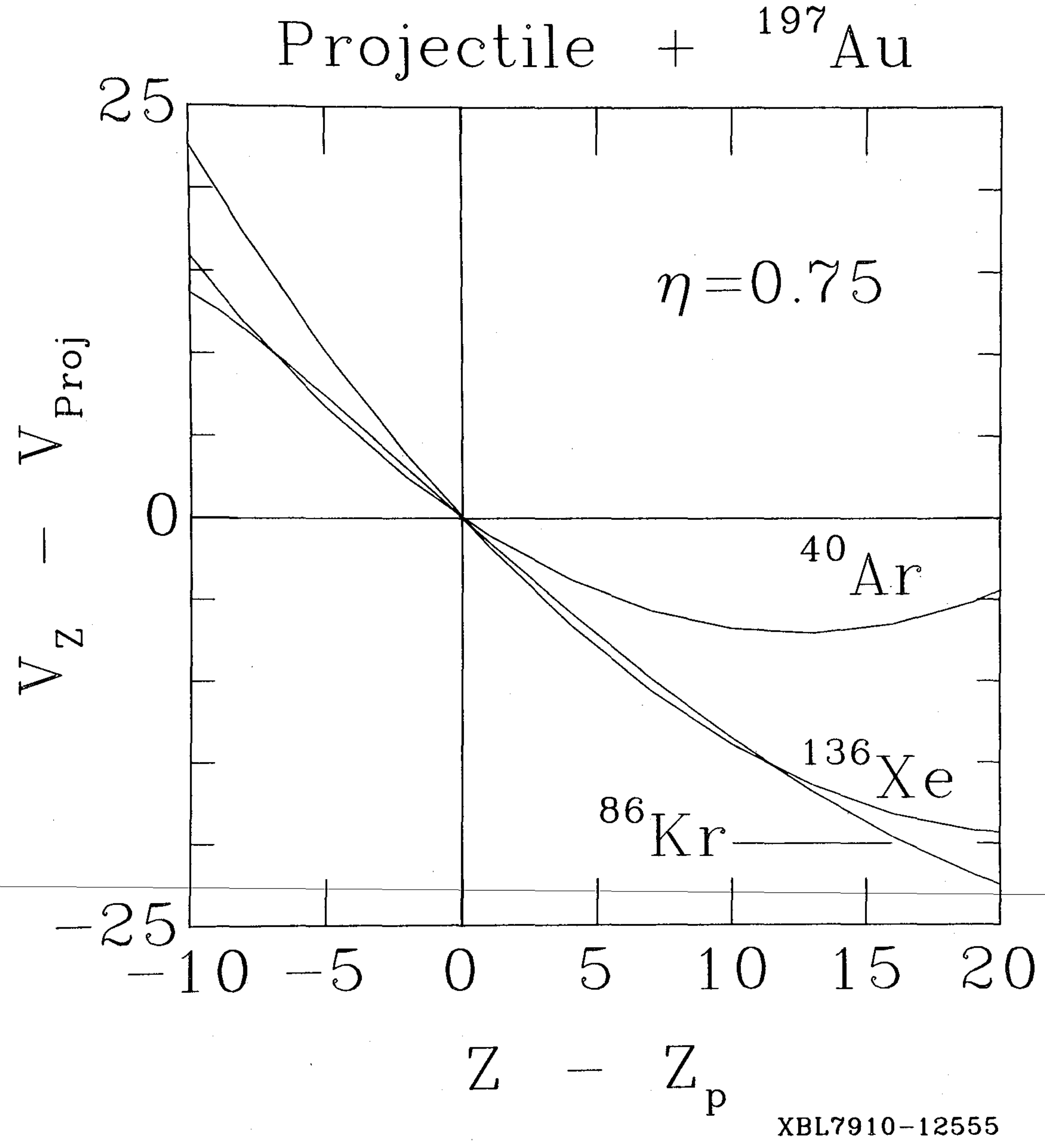

Projectile + ^{197}Au
25
0
−25
η=0.75
^{40}Ar
^{136}Xe
^{86}Kr
−10
−5
0
5
10
15
20
$V_Z - V_{Proj}$
$Z - Z_p$
XBL7910-12555

Fig. 47

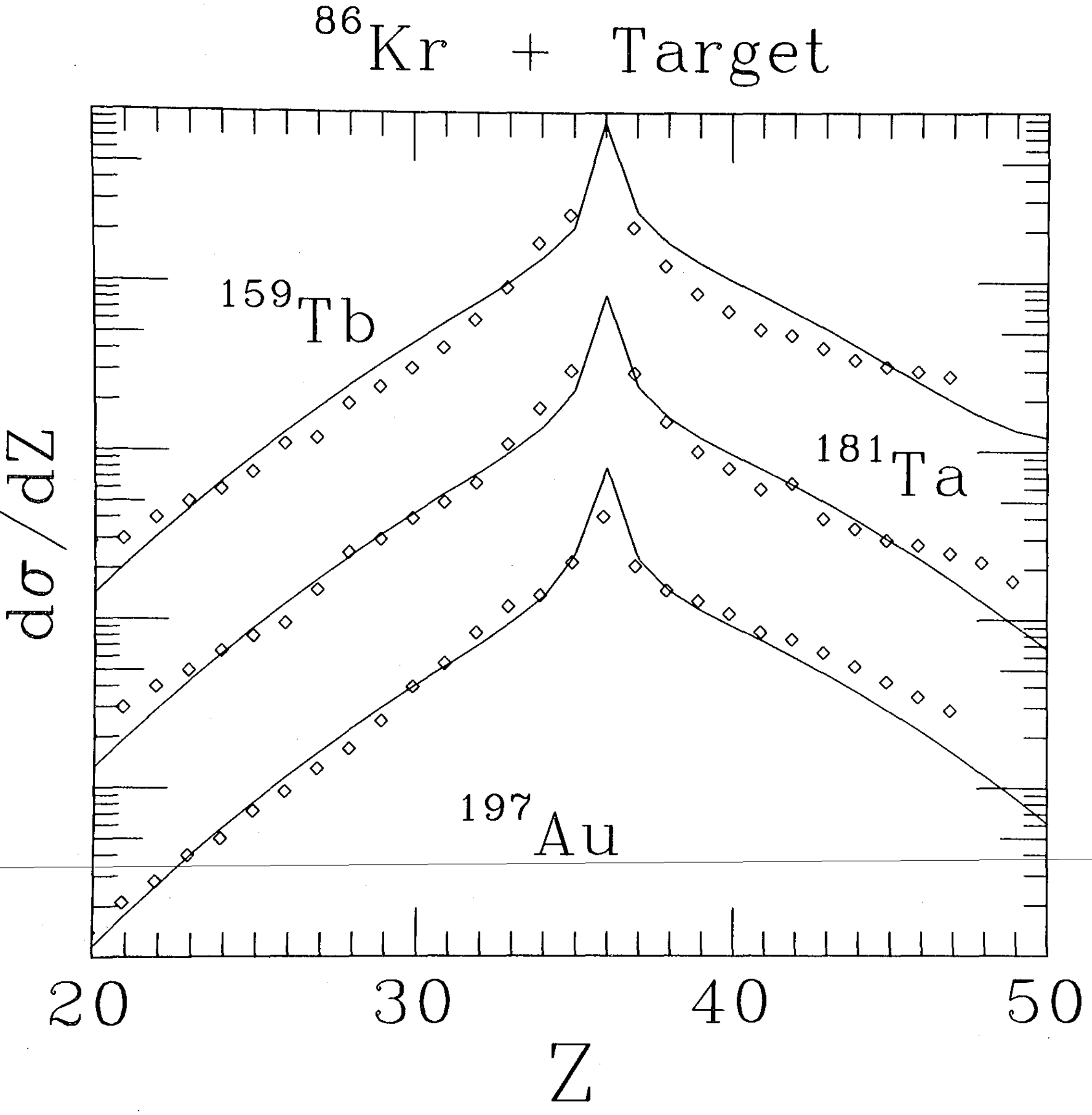

XBL7910-12556

Fig. 48

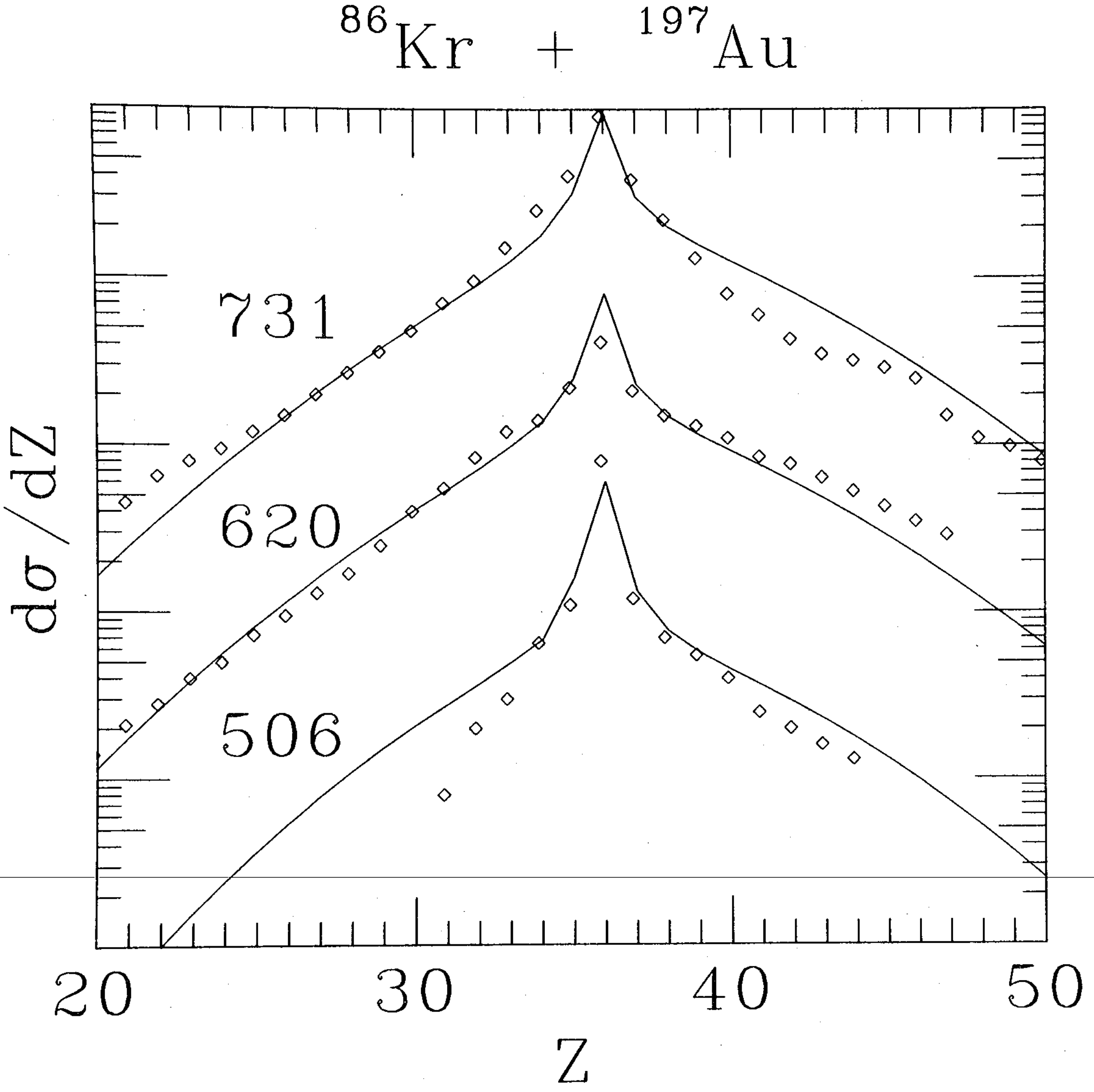

XBL7910-12557

Fig. 49

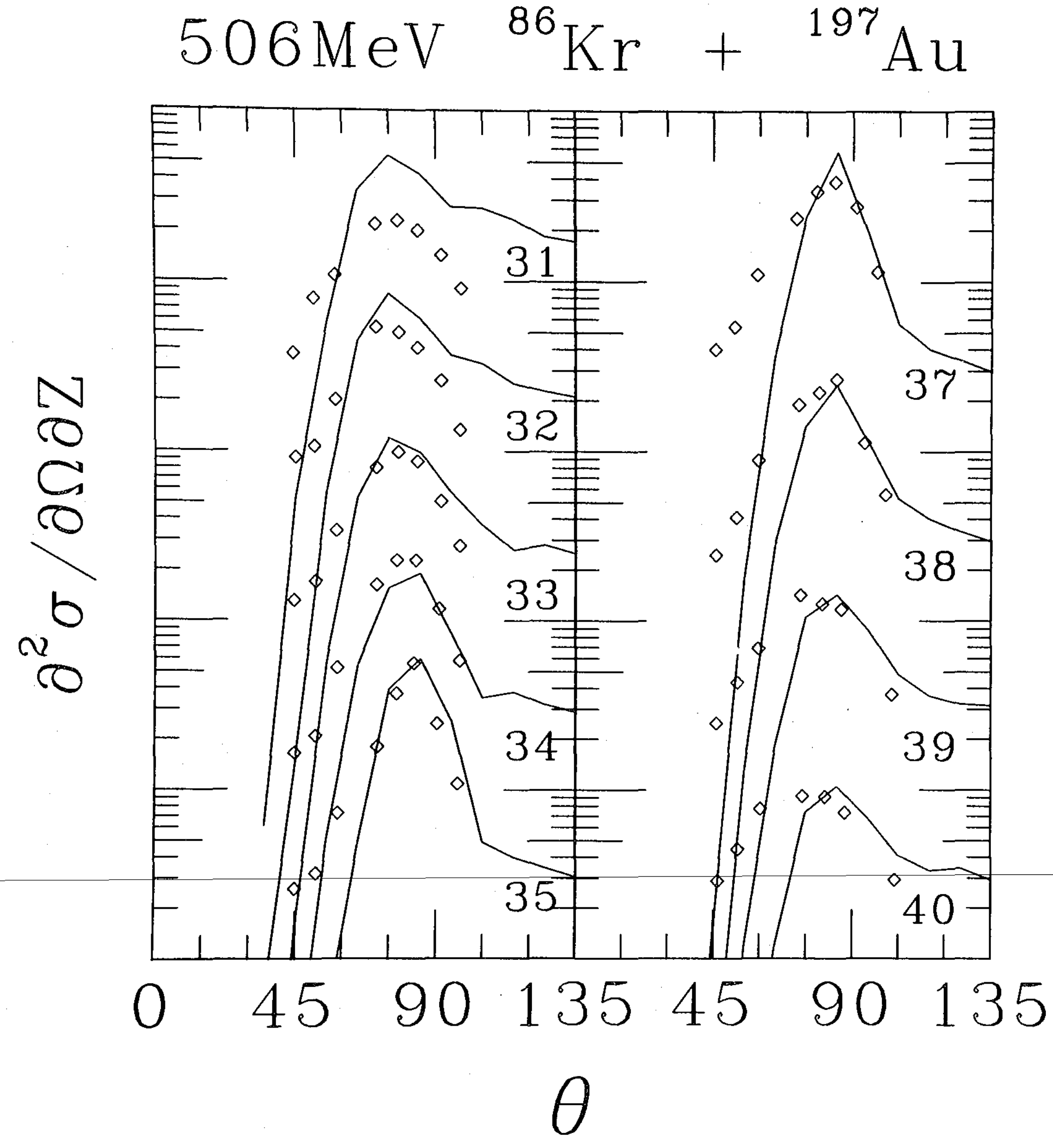

XBL7910-12558

Fig. 50

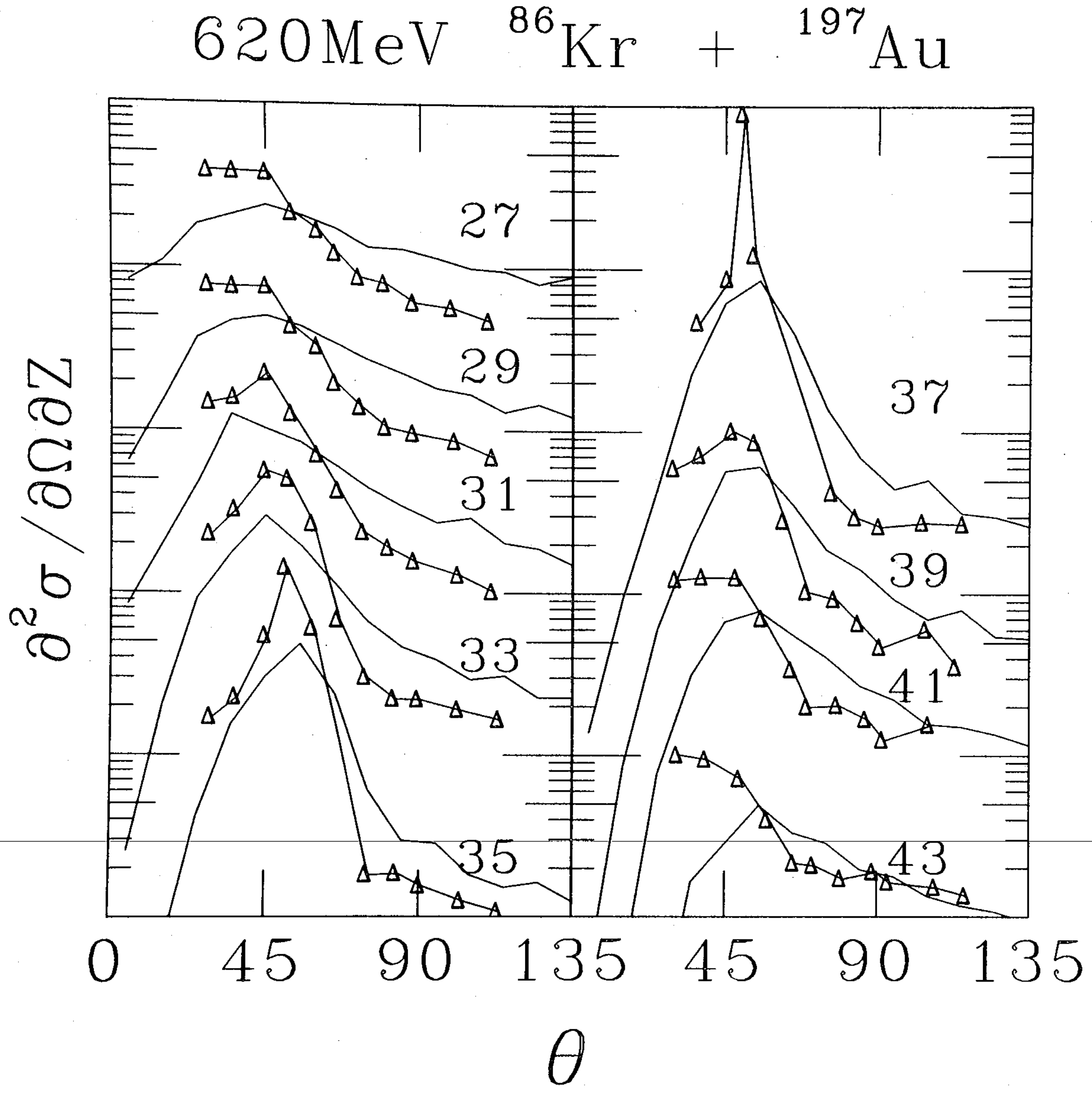

XBL7910-12559

Fig. 51

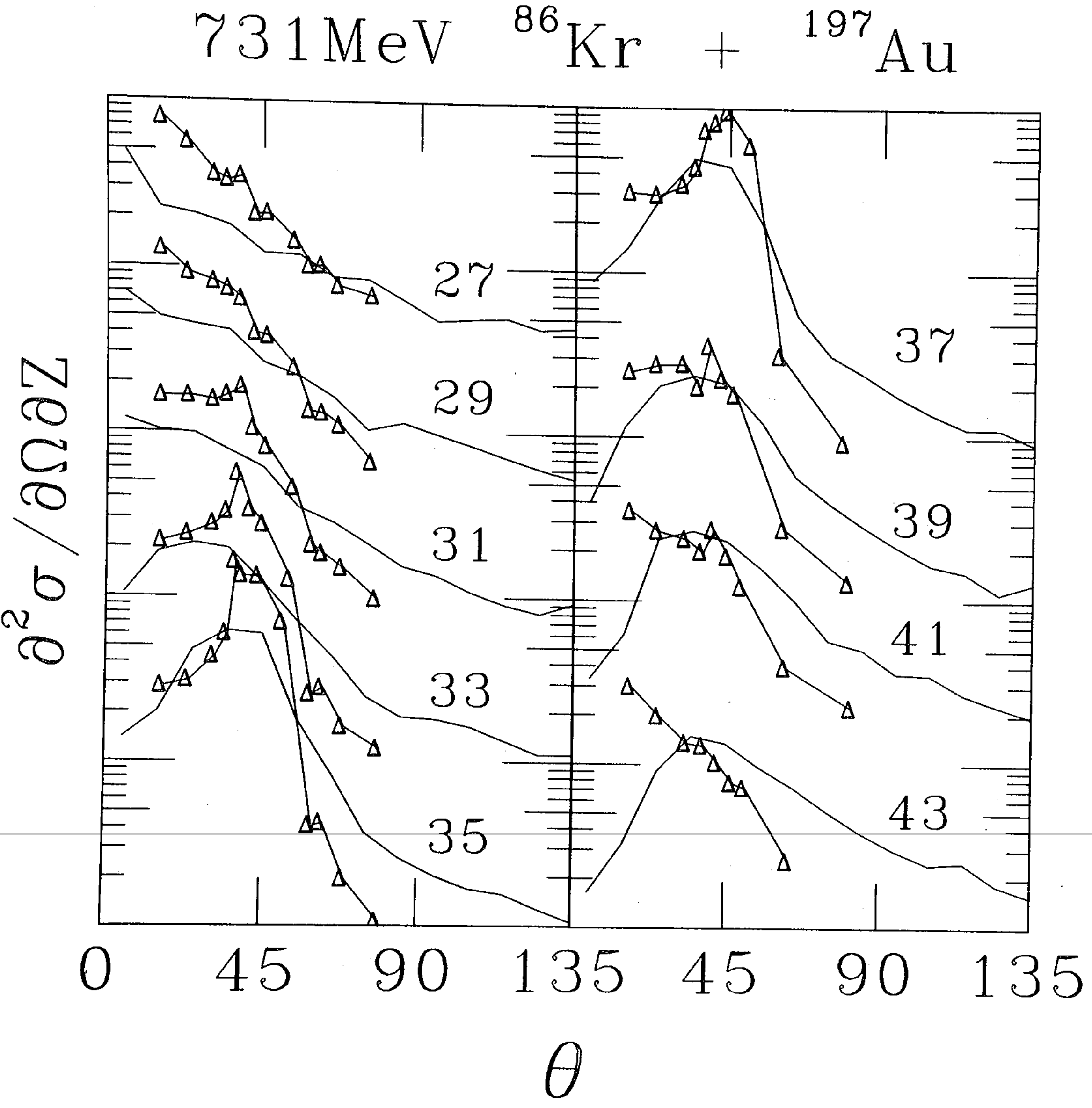

XBL7910-12560

Fig. 52

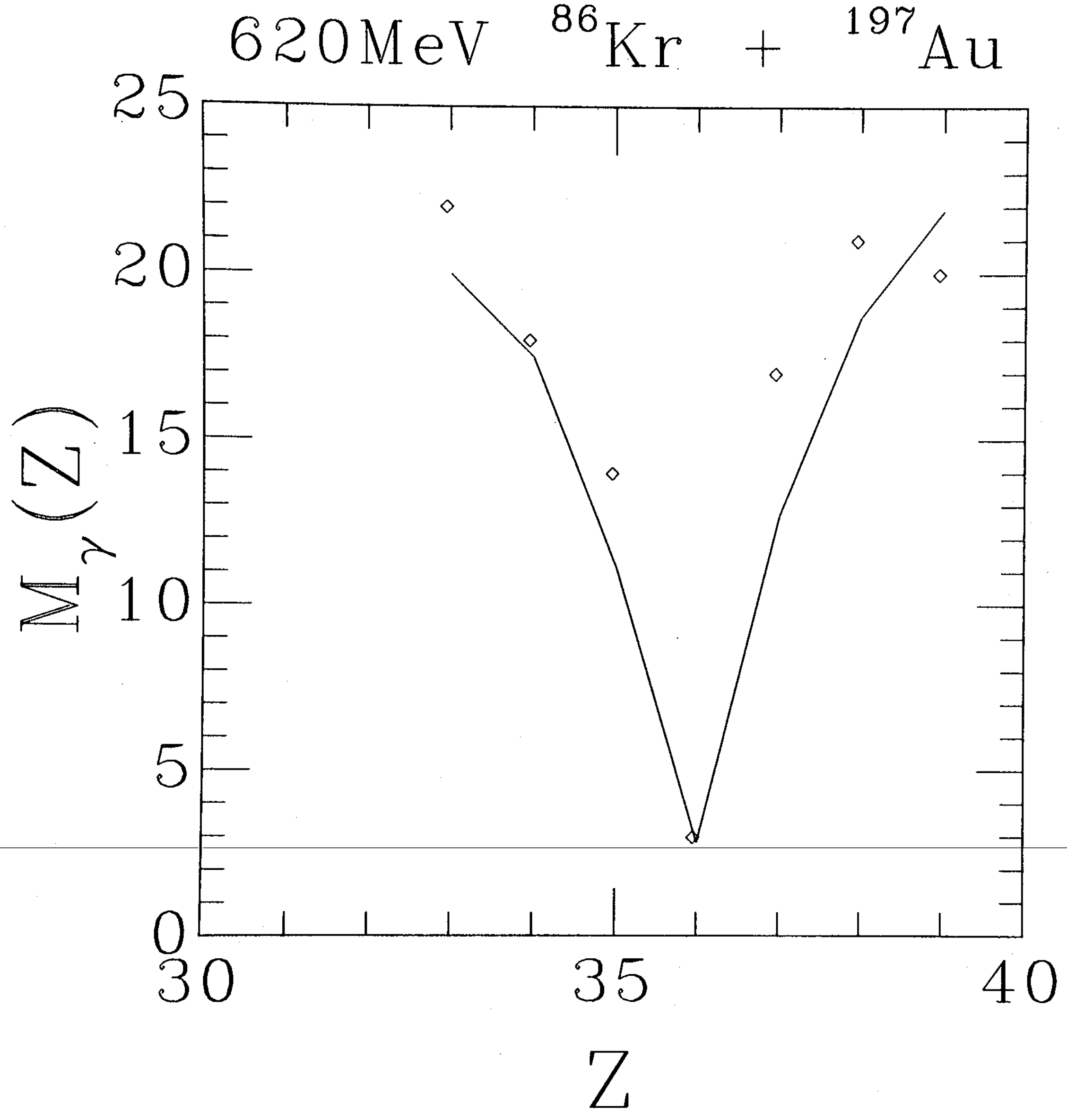

XBL7910-12561

Fig. 53

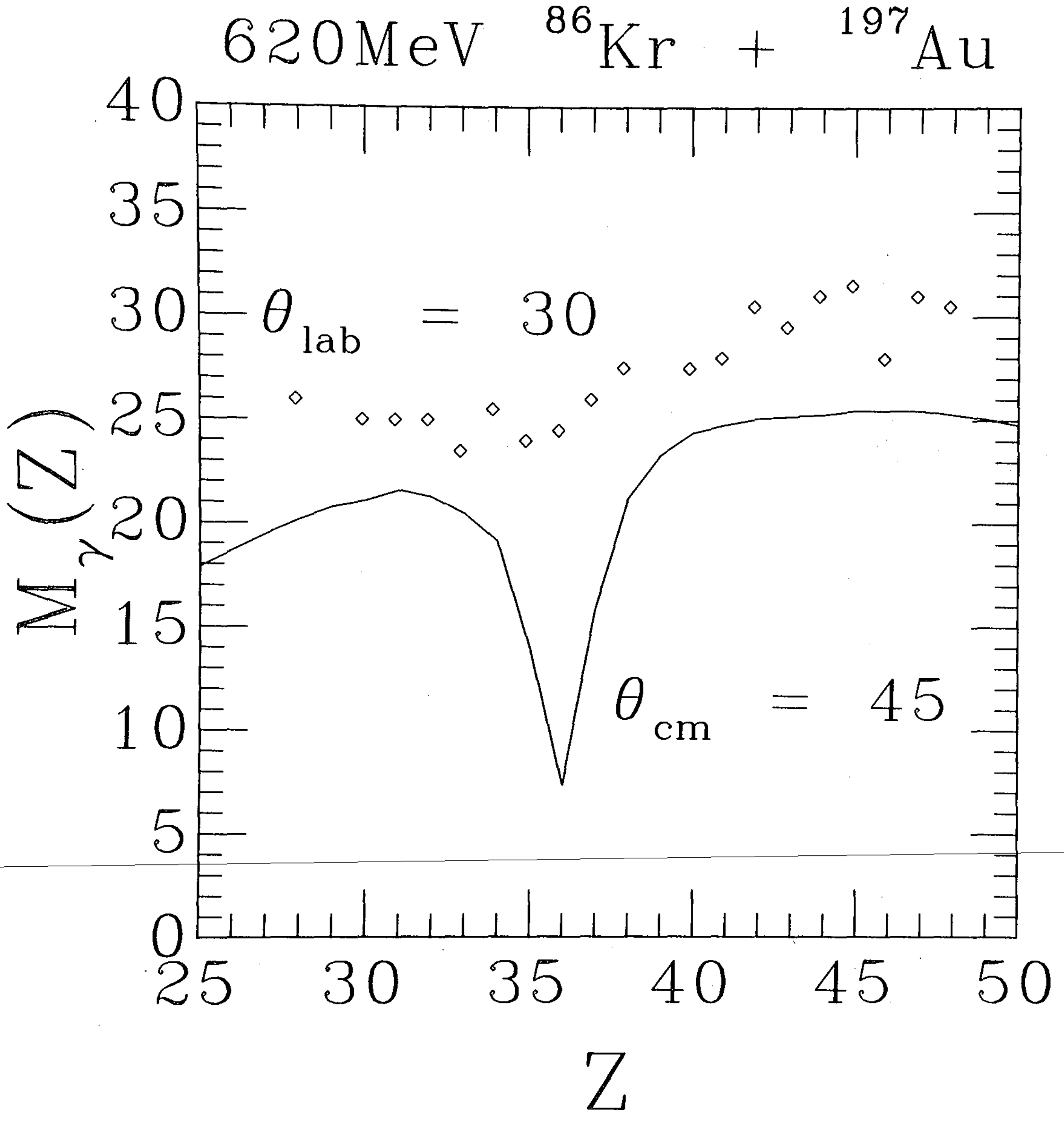

XBL7910-12562

Fig. 54

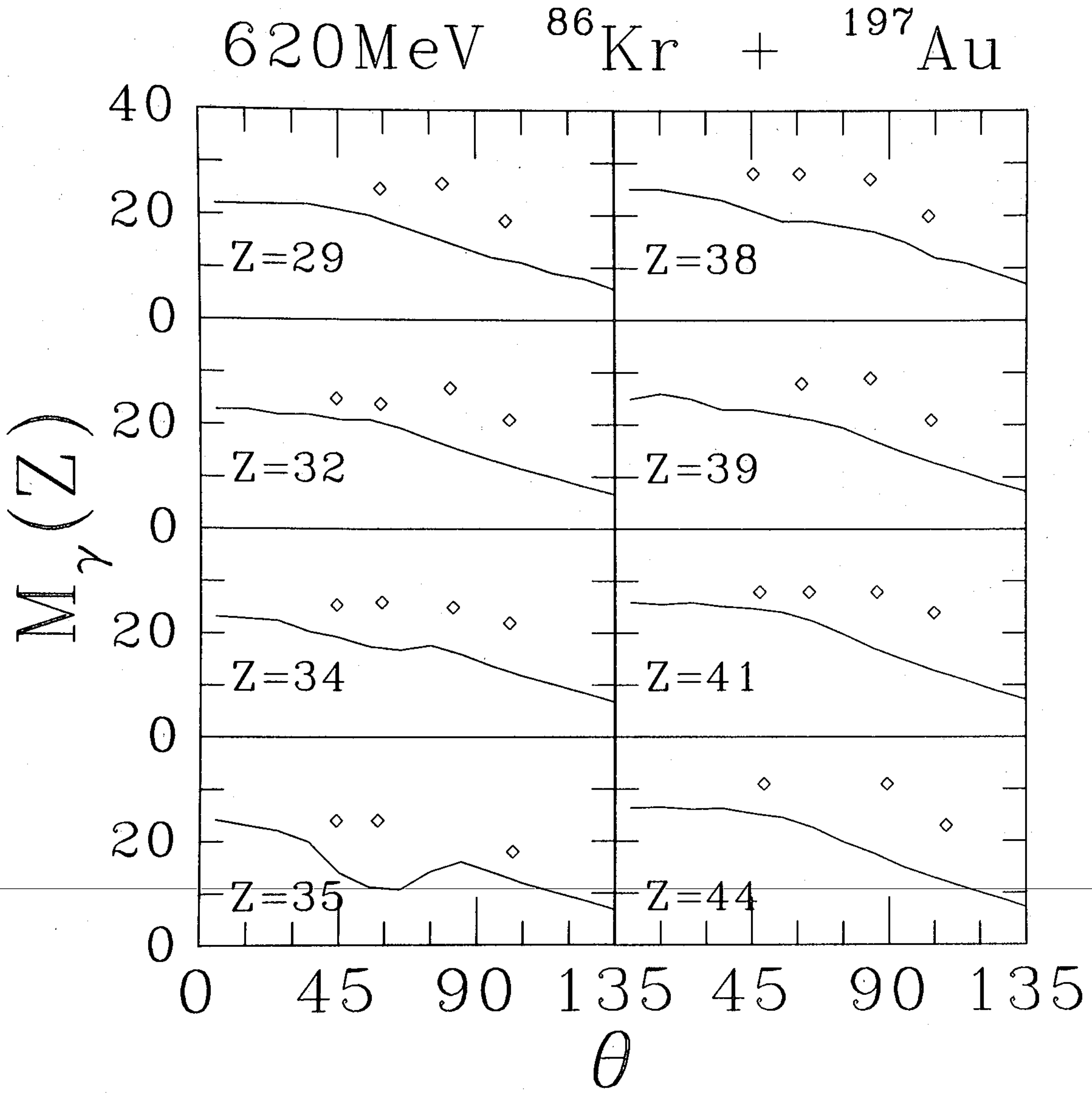

XBL7910-12563

Fig. 55

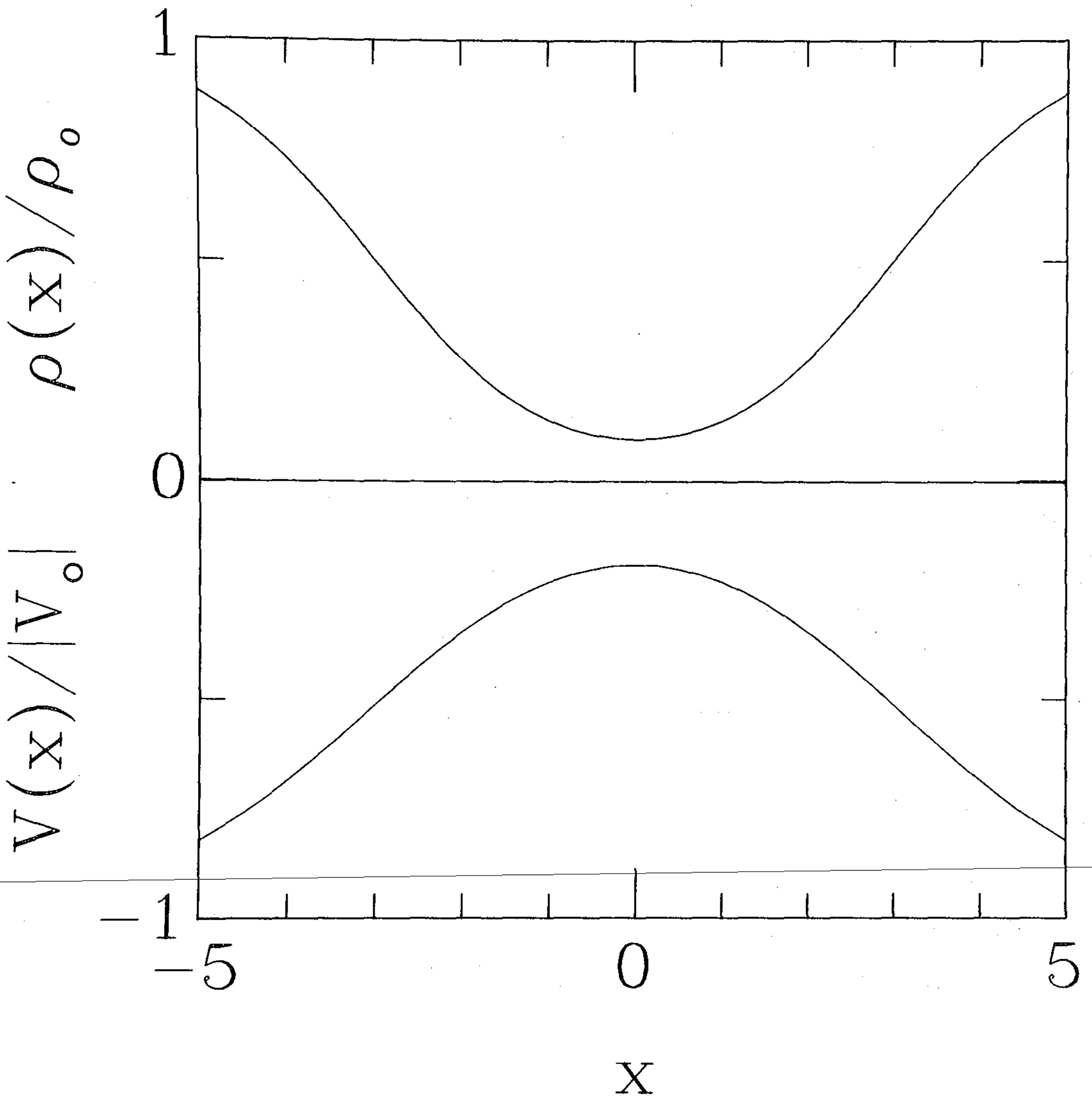

XBL7910-12564

Fig. 56

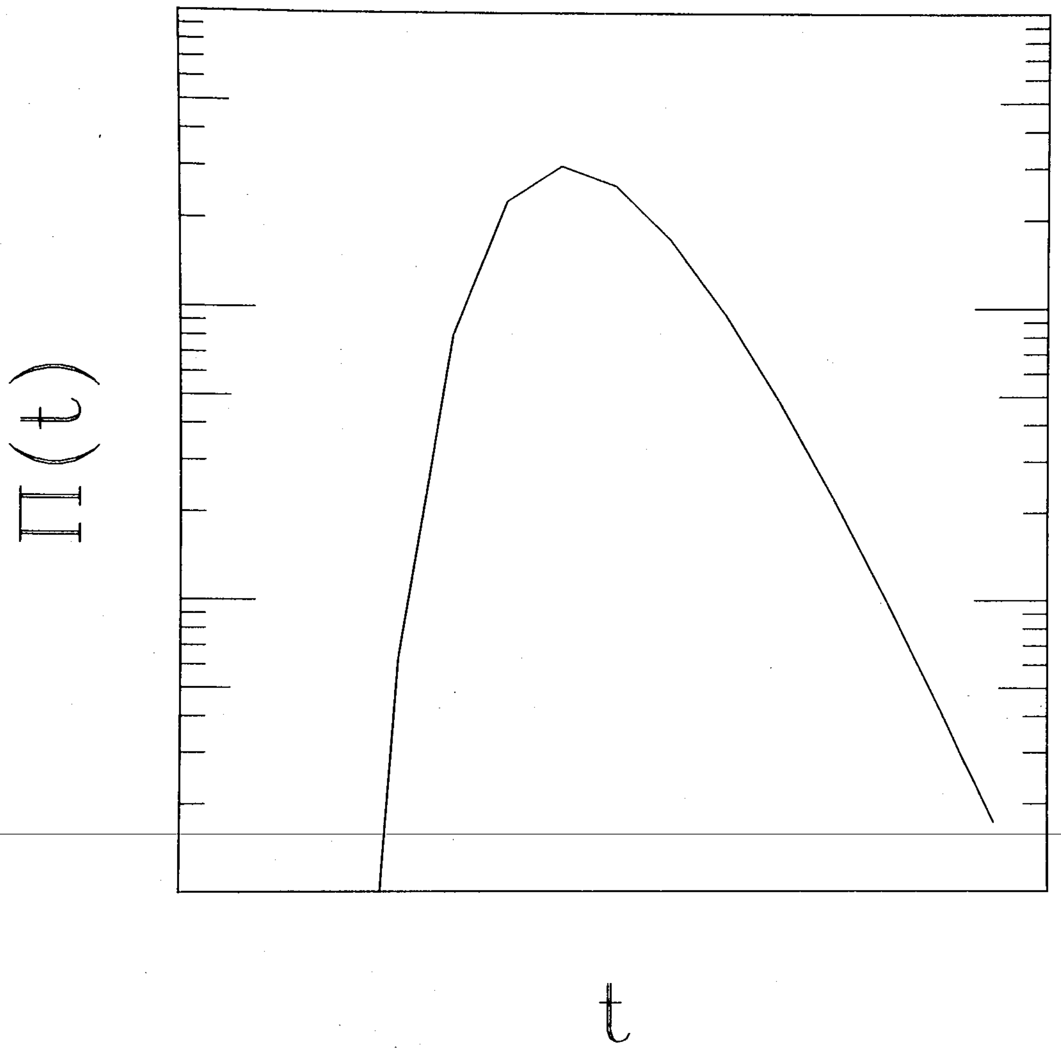

XBL7910-12565

Fig. 57

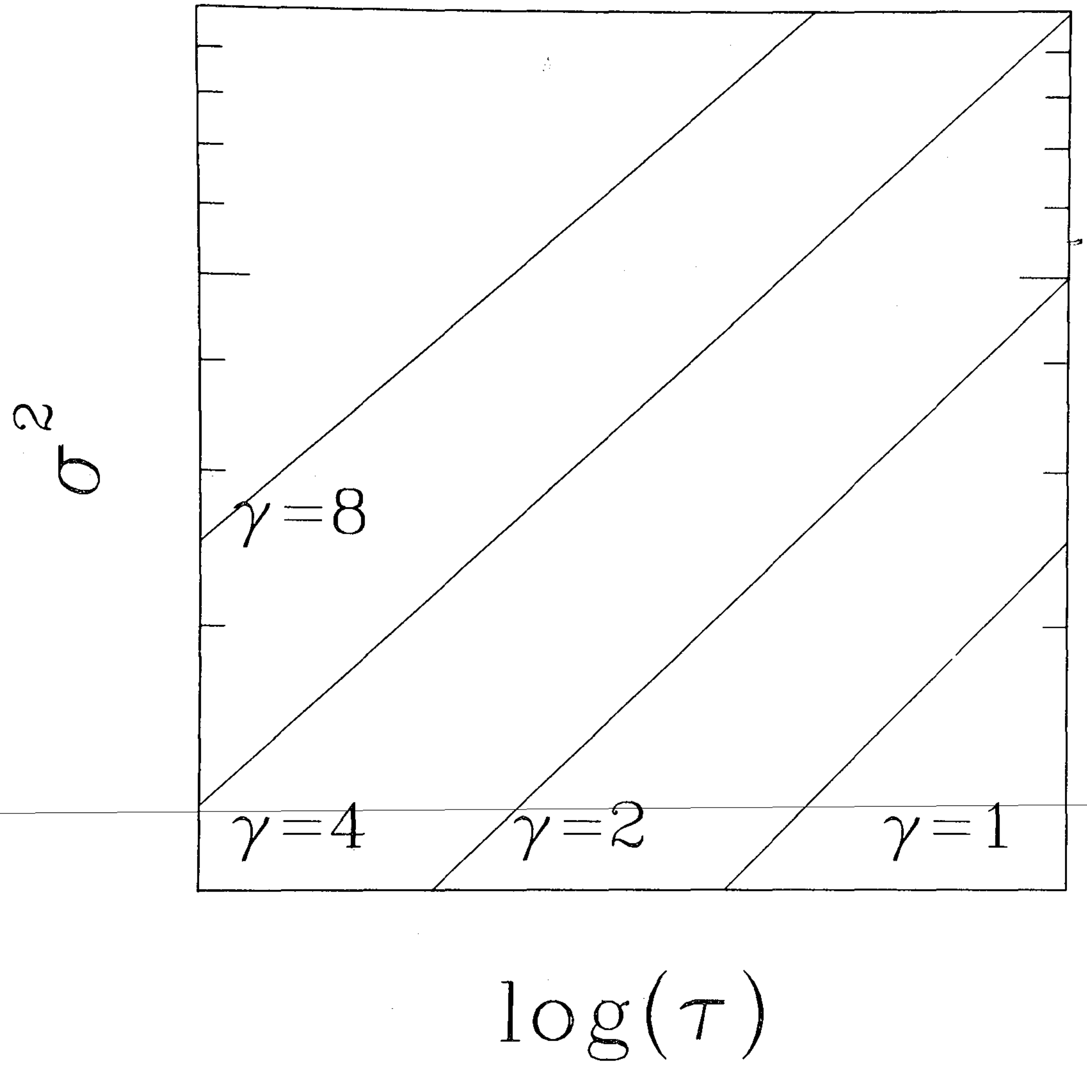

XBL 7910-12566

Fig. 58

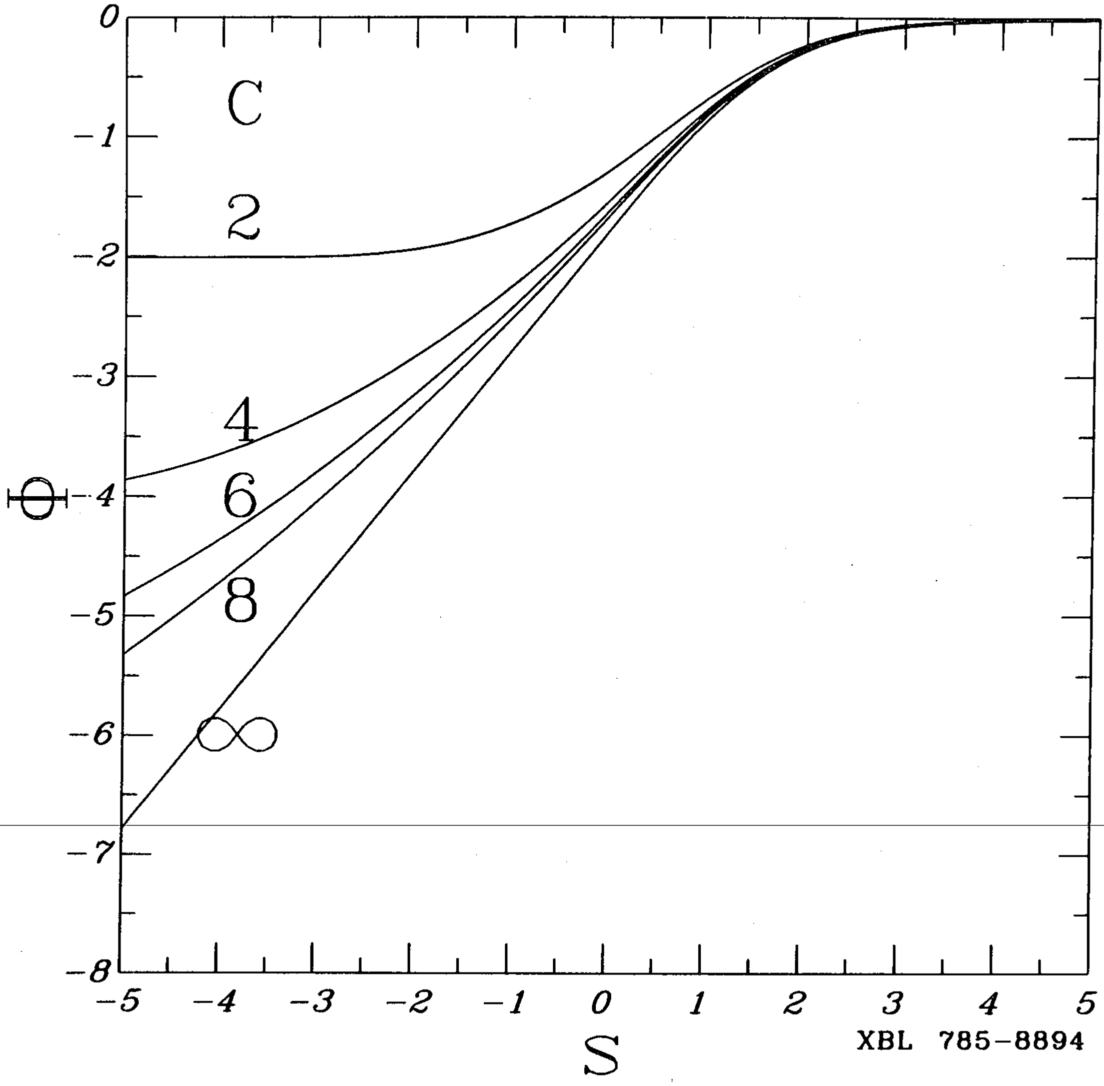

Fig. 59

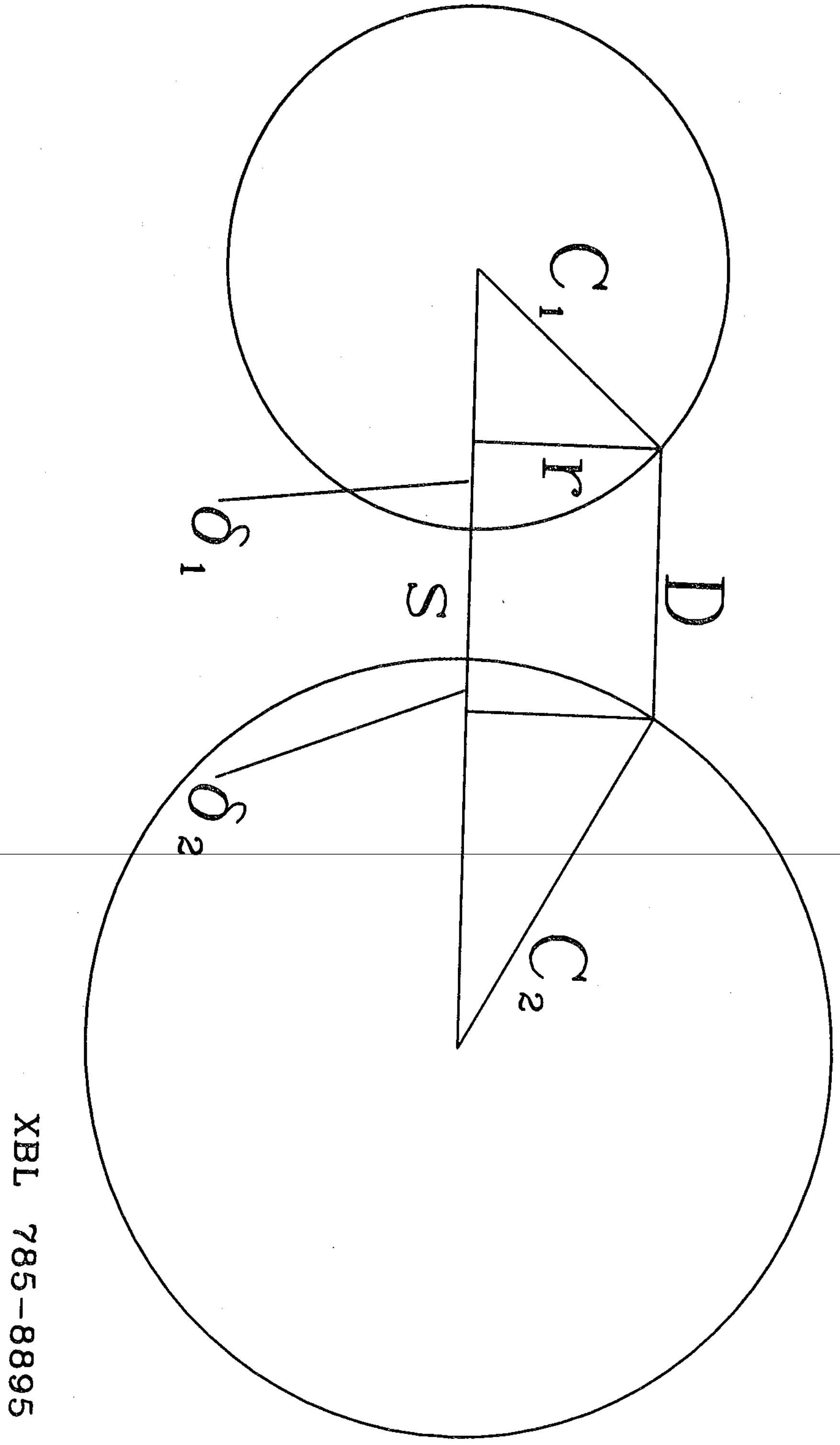

Fig. 60

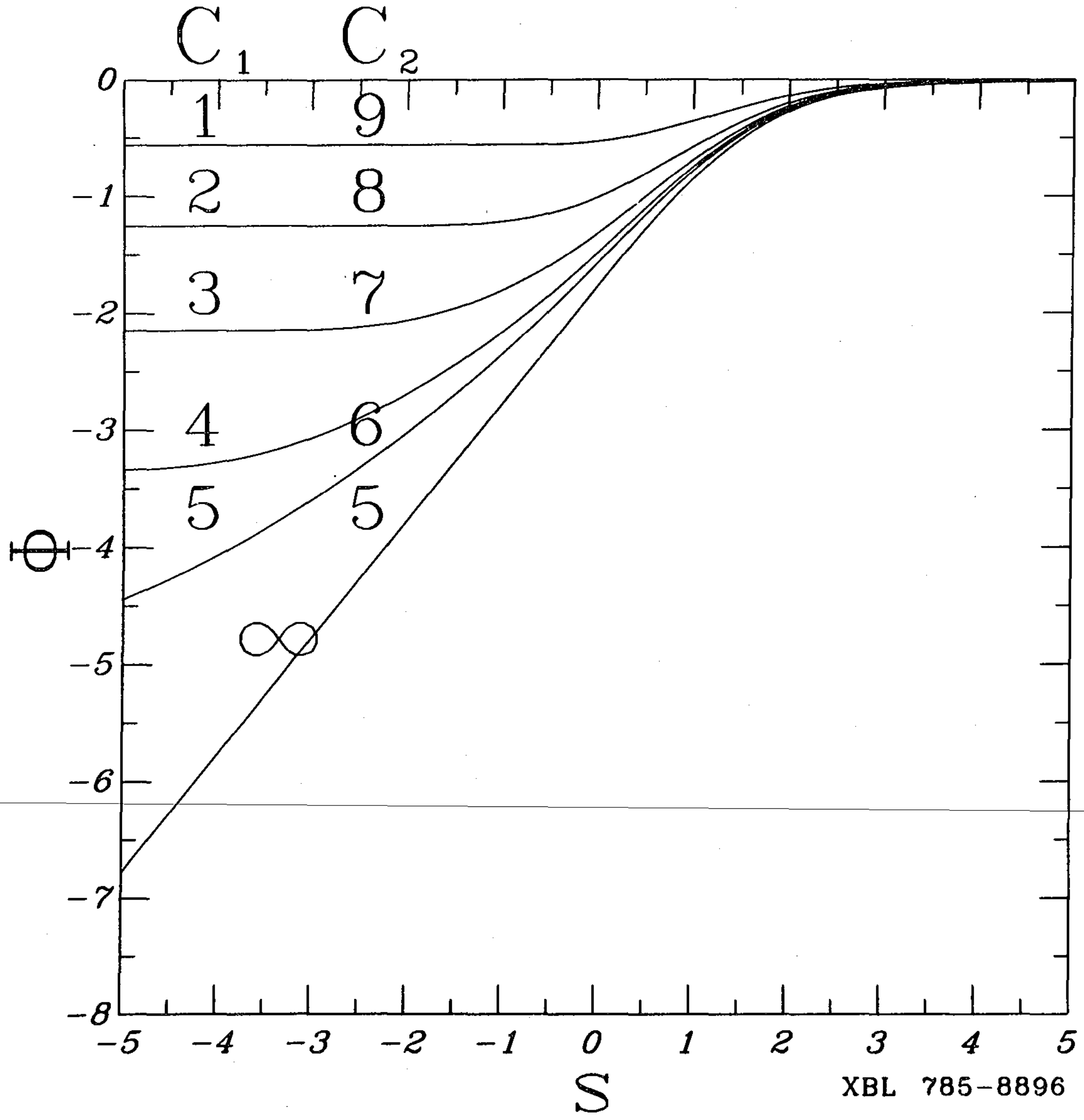

Fig. 61

TECHNICAL INFORMATION DEPARTMENT
LAWRENCE BERKELEY LABORATORY
UNIVERSITY OF CALIFORNIA
BERKELEY, CALIFORNIA 94720